Synthesis and Applications of One-dimensional Semiconductors

Sven Barth*[1,2], Francisco Hernandez-Ramirez[3], Justin D. Holmes[1,2] and Albert Romano-Rodriguez[4]

[1]*Materials and Supercritical Fluids Group, Department of Chemistry and the Tyndall National Institute, University College Cork, Cork, Ireland.*
[2]*Centre for Research on Adaptive Nanostructures and Nanodevices (CRANN), Trinity College Dublin, Dublin 2, Ireland.*
[3]*M-2E / XaRMAE, Catalonia Institute for Energy Research (IREC), Barcelona, Spain.*
[4]*MIND-IN2UB, Department of Electronics, University of Barcelona, Barcelona, Spain.*

*Corresponding author: Dr. Sven Barth, Department of Chemistry, University College Cork, Cork, Ireland

E-mail: sbarth76@gmail.com; s.barth@ucc.ie
Department of Chemistry
Kane Building, College Road
University College Cork
Cork, Ireland

Tel.: +353 214 903301
Fax: +353 214 274097

Keywords: *Nanowire, Semiconductors, Nanosensors, Microcircuits, Photovoltaics, Nanogenerators, Lithium Ion Batteries, Photonics, Synthetic Techniques, Silicon, Germanium, Gallium Nitride, Gallium Arsenide, Cadmium Sulfide, Zinc Oxide, Tin Oxide*

Abstract

Nanoscale inorganic materials such as quantum dots (0-dimensional) and one-dimensional (1D) structures, such as nanowires, nanobelts and nanotubes, have gained tremendous attention within the last decade. Among the huge variety of 1D nanostructures, semiconducting nanowires have gained particular interest due to their potential applications in optoelectronic and electronic devices. Despite the huge efforts to control and understand the growth mechanisms underlying the formation of these highly anisotropic structures, some fundamental phenomena are still not well understood. For example, high aspect ratio semiconductors exhibit unexpected growth phenomena, e.g. diameter-dependent and temperature-dependent growth directions, and unusual high doping levels or compositions, which are not known for their macroscopic crystals or thin film counterparts.

This article reviews viable synthetic approaches for growing high aspect ratio semiconductors from bottom-up techniques, such as crystal structure governed nucleation, metal-promoted vapor phase and solution growth, formation in non-metal seeded gas phase processes, structure directing templates and electrospinning. In particular new experimental findings and theoretical models relating to the frequently applied vapor-liquid-solid (VLS) growth are highlighted. In addition, the top-down application of controlled chemical etching, using novel masking techniques, is described as a viable approach for generating certain 1D structures. The review highlights the controlled synthesis of semiconducting nanostructures and heterostructures of silicon, germanium, gallium nitride, gallium arsenide, cadmium sulfide, zinc oxide and tin oxide. The alignment of 1D nanostructures will be reviewed briefly. Whilst specific and reliable contact procedures are still a major challenge for the

integration of 1D nanostructures as active building blocks, this issue will not be the focus of this paper. However, the promising applications of 1D semiconductors will be highlighted, particularly with reference to surface dependent electronic transduction (gas and biological sensors), energy generation (nanomechanical and photovoltaic) devices, energy storage (lithium storage in battery anodes) as well as nanowire photonics.

1. Introduction

Semiconductors are widely used in electronic, catalytic, photonic and energy related applications. In recent years, ongoing miniaturisation of electronic circuits led to an emerging interest in nanoscaled materials. In addition, inorganic structures confined in several dimensions within the nanometre range, exhibit peculiar and unique properties superior to their bulk counterparts. These unique properties can be attributed to the limited motion of electrons in the confined dimensions of the nanomaterial (quantum effects) [1].

The interest in utilising the unique properties of nanostructures for practical applications increases with the deeper understanding and tailoring of these materials. To date, a huge variety of materials have been synthesised and incorporated in devices demonstrating their potential to overtop the performance of currently used technology. The material classes of inorganic 1D structures include metallic elements [2,3], metal nitrides [4,5], oxides [6,7], carbides [8,9], and sulfides [10,11]. However the transition from fundamental science to industrial application requires an even deeper understanding and control of morphology and composition at the nanoscale. Size reduction of well known materials into the nanometre regime or the realisation of novel nanostructures can improve device performance and lead to novel discoveries. For instance, in microelectronics the increased number of transistors per area of a silicon chip, has led to faster operation and lower power consumption [12]. Size-dependent physical properties observed in 1D nanomaterials have included photon absorption and emission, such as nanoscale avalanche photodiodes [13], metal-to-insulator transition in a material [14] and quantised or ballistic transport characteristics [15]. However literature reports describe divergent behaviour of some intrinsic material properties,

such as the elastical modulus [16-18], for nanosised materials ranging from diminishing to increased values with shrinking radial dimensions, which implies that reliable instrumentation has to be established to gain precise insight in the effects present in the nanometre regime. Besides the opportunity to investigate and evaluate novel physical properties of 1D materials, the controlled fabrication of high quality nanowires and their growth mechanisms has attracted tremendous attention. Though the number of reports describing the growth of novel 1D structures has increased rapidly over the last ten years, the fundamental understanding of their formation is still limited. In addition, the integration of high aspect-ratio nanostructures into devices requires ongoing efforts in both engineering and materials science to control the processes on the atomic scale [19].

In this article, state-of-the-art strategies for engineering one-dimensional functional semiconductors, which can be used for photonic, sensor and energy applications, are reviewed. Viable growth strategies and mechanisms are outlined in this review and the synthesis of Si, Ge, GaN, GaAs, CdS, ZnO, and SnO_2 is outlined. For controlled use of individual or bundles of defined numbers of nanostructures alignment techniques are a mandatory requirement. A description of the most effective in situ and post alignment methods is therefore included in this review. In addition, we emphasise the applicability of nanowire-based devices for gas and biochemical detection, nanophotonics, energy harvesting, such as nanogenerators and solar cells, as well as components in Li ion batteries.

2. Synthetic approaches to 1D nanostructures

During the last decade several approaches for synthesising 1D nanostructures have been described in detail, however generic methodologies are limited. Herein we delineate rational strategies used to facilitate the formation of inorganic high aspect-ratio nanostructures. Figure 1 illustrates different types of 1D nanostructures and the terms/abbreviations used to describe them.

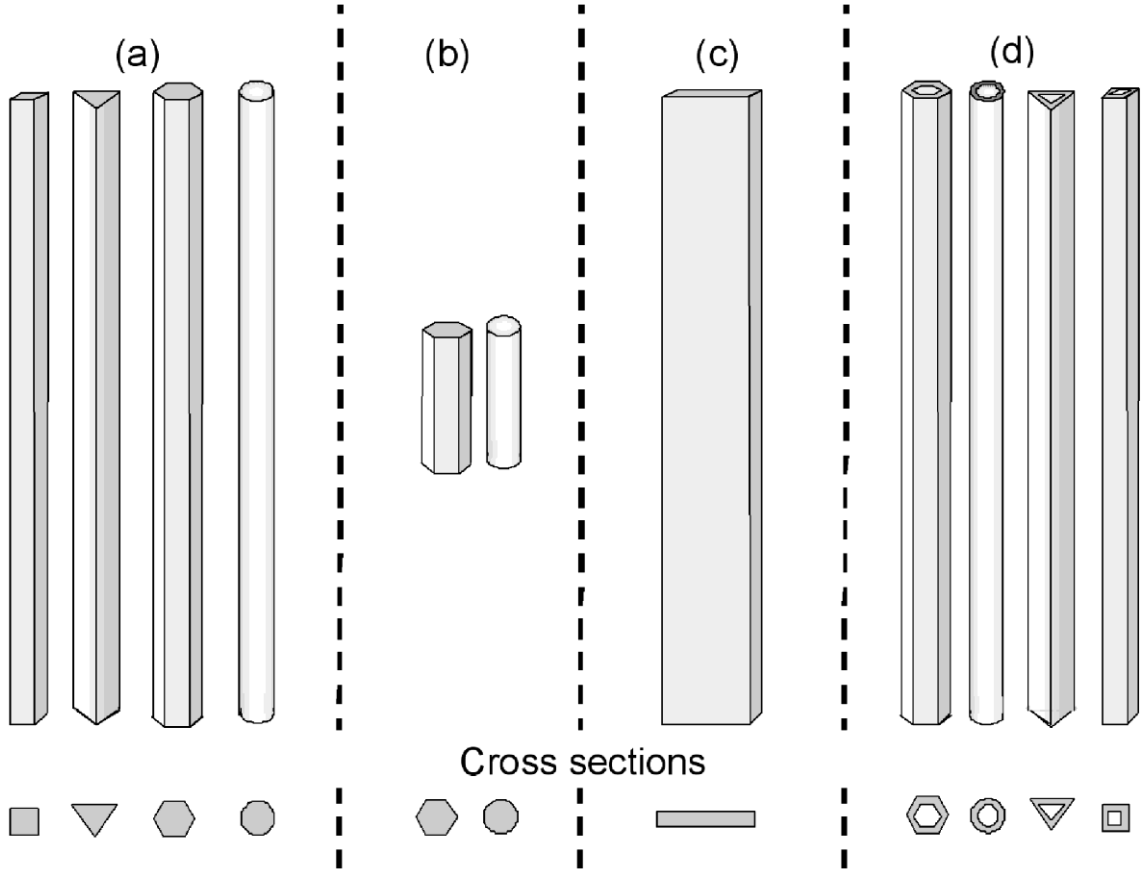

Figure 1. Schematic illustration different shapes of 1D nanostructures and the terms typically used to describe them: (a) nanowires (NWs), nanofibers or whiskers; (b) nanorods (NRs); (c) nanobelts (NBs) or nanoribbons and (d) nanotubes (NTs). Among these structures, the only ones restricted to a certain cross section are NBs, which typically have one dimension of a few nanometres and a second dimension up to the range of hundreds of nm.

2.1 Crystal structure governed nucleation in solution

Anisotropic growth of crystals is induced by the sum of surface energies of the terminating facets, which causes the formation of most elongated nanocrystals. In solution, several materials show preferential growth facets under appropriate experimental conditions such as nucleus formation, concentration, pH and ionic strength [20]. The crystal structure governed formation of 1D nanostructures is not universal, due to the intrinsic requirements on the crystal structure itself. The formation of high aspect ratio (> 200) nanostructures is limited to a few systems such as Se and Te, which actually produce nanowires instead of rod-like structures [21-23]. For the formation of most materials, the contribution of surface energies of different crystal facets to the total system energy is not enough to promote the formation of 1D nanostructures. This problem can occasionally be overcome by adding surfactants to the growth solution to modulate the effective surface energy of the growing crystals to engineer 1D nanostructures due to site-specific adsorption and residence times of surface modifiers [24].

In addition, for polytype materials the crystallographic phase and the balance of kinetic and thermodynamic growth regime are responsible for the shape of the synthesised nanoscaled crystals. For instance, low temperature and short reaction times allow the formation of zinc blende or wurtzite phase MnS nuclei which act as seeds for nanowire or multipod growth as shown in figure 2 [25]. Higher temperatures lead to rock salt MnS nuclei and the growth of cubes. In the kinetic regime, fast growth promotes 1D formation whereas prolonged heating at identical low temperatures leads to more thermodynamically stable particles. Another example is the hydrothermal growth of inorganic materials in combination with the addition of structural directors,

such as amines [26] or acetates [27] to grow ZnO nanowires. Different stages of ZnO crystals development from nanoparticles to nanorods and even into single crystalline nanowires after prolonged reaction times.

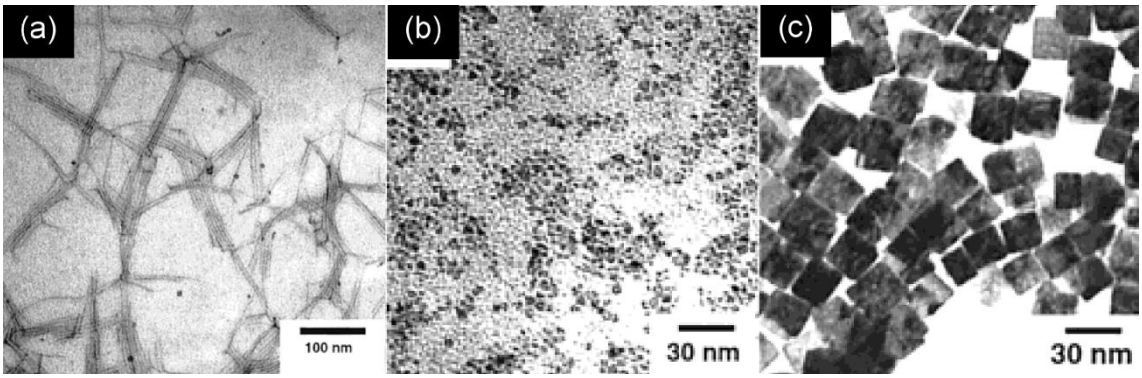

Figure 2. Shape evolution of MnS nanocrystals by the variation of growth temperatures: wires at 120 °C (A), spheres at 180 °C (B), and cubes at 250 °C (C). Reprinted from Ref. [25] with permission of ACS Publishers.

2.2 Non-metal seeded gas phase growth

In the absence of metal catalysts, the vapor–solid (VS) or self-catalytic growth mechanism has been mainly used to synthesise metal oxide and some semiconductor nanomaterials. The anisotropic growth of nanowires can be promoted by manipulating the differences in crystal surface energies, defects such as screw dislocations, and self-catalytic formation of a metal wetting layer. In all of the cases the growth front plays a crucial role in the adsorption of atoms or phase forming species. The front can be very rough (poorly arranged atomic positions and the presence of defects) which promotes the sticking of diffusing species and nucleation. An ideal crystal facet contains only a few nucleation centres and potential desorption events of diffusing species are likely due to the low binding energy. In this respect, the presence of defects, such as screw-dislocations, is mandatory to provide continuously atomic steps, where the diffusing species can bond. In addition, twin structures exhibit at the twinning plane, potential

nucleation centres for a layer by layer growth of the respective grain. The effect of dislocations on crystal growth was reported by Burton *et al.* sixty years ago, who described the importance of defects for crystal growth at low supersaturation due to the low stability of 2D nuclei at reduced pressures [28]. In a perfect crystal the growth can only proceed if new surface steps are formed and layer by layer growth occurs, however the growth rate of real crystals is much higher due to the presence of defects (kinks, twins, dislocations). The first report dealing with a screw dislocation mediated whisker growth was reported by Sears in 1955 for mercury [29].

Pure vapour transport synthesis is a resublimation process and the material morphology is governed by process parameters, such as substrate temperature, gas phase composition and overall pressure. This synthetic strategy allows the synthesis of belt-like structures, which show defined side-facets with low surface energies. The nucleation step could be induced by defects on the growth front which exhibit a rounded shape or by sequential incorporation of charged species on nuclei combined with the formation of low energy facets or catalytic growth (self-catalytic or metal induced), followed by VS growth to attain the most favoured nanostructure under given experimental conditions [30]. The presence of reduced metallic species cannot be excluded and is described by the same group [31], which indicates that both, self-catalysis and defect induced growth, can promote nanowire growth either by carbothermal transport or resublimation. The morphology is dependent on several factors, such as substrate temperature as well as carrier gas flow and composition. Complex 1D ZnO structures based on nanobelt-based structures, such as helices and rings that are formed due to reeling up of nanobelts owning polar facets, can be formed by accurate control of growth kinetics (figure 8) [32, 33].

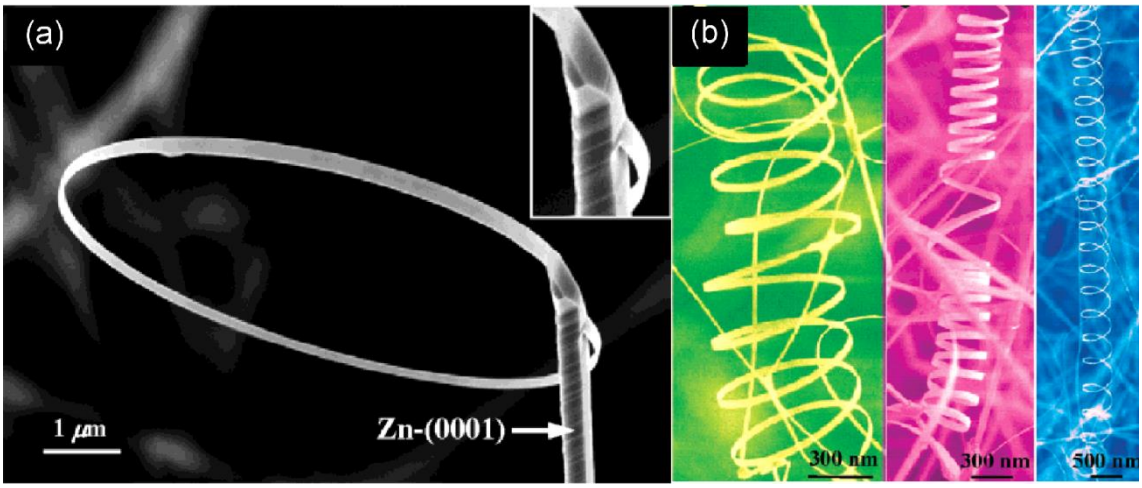

Figure 8. (a) SEM image of a ZnO nanoring formed at the end of a ZnO wire and (b) SEM of ZnO nanobelts with helical structure formed by a resublimation process. Reprinted from Ref. (a) [32] and (b) [33] with permission of ACS Publishers

Another formation mechanism of 1D nanostructures is the oxide assisted growth (OAG) of nanowires in which a thin oxide shell is formed around the semiconductor core (figure 9) [34].The growth of semiconductor nanowires via an OAG mechanism has been reported for two different synthetic routes, pulsed laser ablation of semiconductor/oxide mixtures and simple evaporation techniques, enabling the growth of semiconductors such as Si [35], Ge [36] and GaAs [37], with thin oxide shells surrounding the semiconductor core. For instance, silicon forms suboxides in the gas phase which can disproportionate to pure Si and SiO_2 and which can form a composite material at a substrate surface [38]. Continuous delivery of gaseous silicon suboxide at the appropriated reaction conditions leads to the formation of Si NWs covered with an oxide shell, while the growth front is expected to be a semi-liquid suboxide [35]. In addition, a two stage process allows the self-seeded growth of Si nanowires when a reactive SiO_x sub-layer is used as the growth surface. This sub-layer results in the formation of Si seeds, by disproportionation, which subsequently promote the growth of

nanowires under similar conditions used in VLS growth (thermal decomposition of silane or germane) [39].

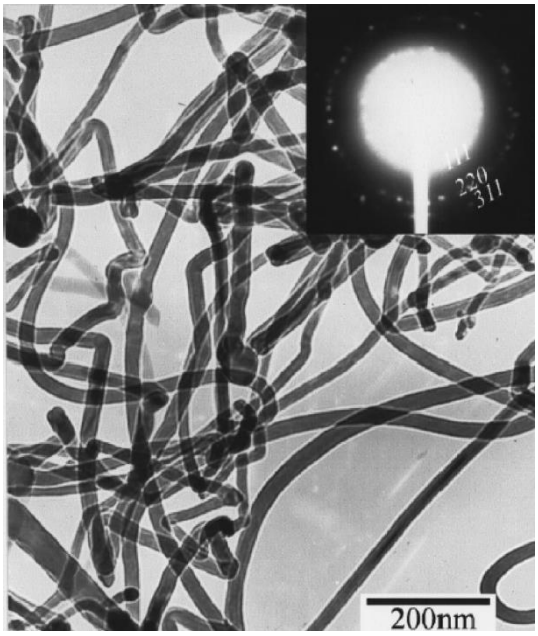

Figure 9. TEM image of Ge NWs formed by oxide assisted growth techniques. Reprinted with permission from [34]. Copyright (2000) by the American Physical Society.

2.3 Metal-promoted vapor growth

Several vapour sources are viable for the synthesis of 1D nanostructures, including thermal and pulsed laser induced evaporation, chemical vapour deposition (CVD) and molecular beam epitaxy (MBE). Thermal evaporation is typically a high temperature vapour process used for depositing high melting point materials, where a significant amount of energy is required to break strong chemical bonds. Pulsed laser deposition is a variable technique in which a solid phase material is evaporated through high energy laser pulses. Even though the local temperature during a pulse is very high, the overall temperature of the source material is fairly low, when compared to the thermal evaporation process. MBE is based on the thermal evaporation of the phase forming elements under high vacuum conditions, which react on a substrate surface to form the

desired crystal lattice. CVD techniques probably allow for the highest variability of deposition parameters. The chemical reactions involved in the precursor-to-material conversion can include thermolysis, hydrolysis, oxidation, reduction, disproportionation, nitration and carboration, depending on the precursor species used. Once the gaseous species are in proximity to the substrate or the surface itself, they can either adsorb directly on the catalyst particle or on the surface. Diffusion processes as well as the concentration of the adsorbates (supersaturation) are responsible for the growth of a solid phase at the catalyst-surface interface. In the early 1960's Wagner and Ellis described the growth of micrometer-sized Si whiskers/wires with hemisphered or truncated tips of similar radial dimension, the so called vapor-liquid-solid (VLS) mechanism [40]. Given the fact that gold and Si can form an alloy, it was concluded that the intermixing occurs at higher temperatures and acts as a nucleation side for Si crystals. Wagner and Ellis proposed that the precursor preferentially decomposes on the liquefied alloy droplet and the resulting Si could either desorb or be incorporated in the droplet (figure 3(a)). Due to a continuous supply of precursor the liquid alloy eventually becomes supersaturated and the Si precipitates at the solid-liquid interface. Apart from the potential catalytic activity, the function of the metal particles is twofold: (i) absorption of structure forming species from vapour phase or substrate surfaces, driven by lowering the chemical potentials of the sources and (ii) precipitation or crystallisation of the source materials at the particle-substrate interface. A deeper insight into the potential VLS mechanism was provided by Givargizov who described the dissociation of a precursor at the particle surface, incorporation of Si in the catalyst material, the diffusion of decomposed wire-forming species through the particle and nucleation of a nanowire at an interface [41]. Despite the fact that in the literature the

metal particle is often described as a catalyst, in most cases it does not necessarily lower the activation energy for the decomposition of the precursor species, which was already but not explicitly described by Wagner *et al.* for Si [42]. Several groups have reported different activation energies for bulk and metal-promoted nanowire growth, suggesting catalysis may play a role in some cases [43, 44].

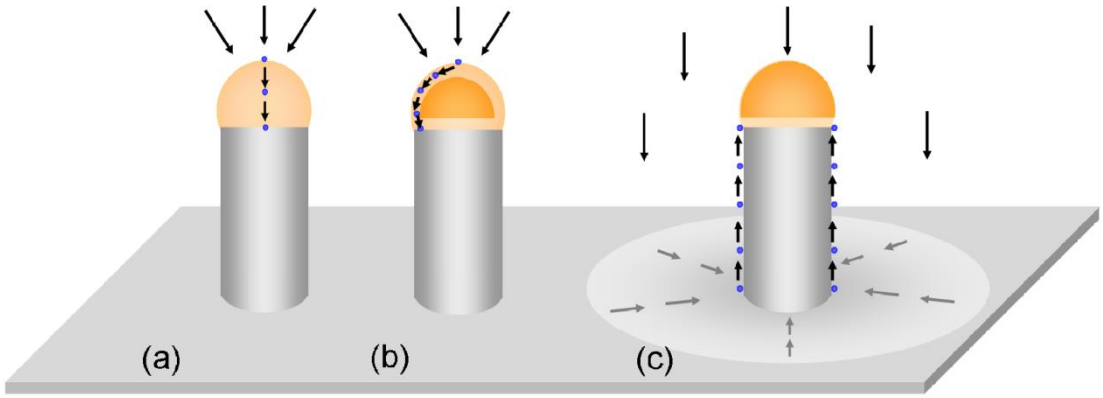

Figure 3. Diffusion models for the source atoms to the growth front of the nanowires: (a) classical VLS with diffusion through a liquid seed, (b) a partially molten particle with liquid surface and interface and solid core and (c) a solid growth seed with a liquid particle wire interface and additional surface diffusion area.

Despite these results of enhanced growth due to the catalytic activity of the metal particle, this fact cannot be attributed to MBE-grown materials, which also show the metal seed promoted nanowire formation [45-47]. Therefore the catalytic effect of the metal seed could play a role in the growth of nanowires under specific conditions, but it does not necessarily mean that this is the underlying reason for 1D crystal growth. In addition, the effect the substrate has on the decomposition of a precursor, such as influencing the growth rate, has to be taken into account [48]. In this respect, substrate material and growth parameters, such as precursor choice, side-wall reactions, temperature, pressure, and carrier gas, have to be taken into account if film and wire

growth are compared because these factors can alter the value of the calculated activation energy by changes in the rate-limiting steps.

Given the enhanced growth rate of nanowires when compared to the competing 2D film growth, the local concentration of adsorbed phase-forming species has to be different on the substrate surface compared to the metal/alloy particles, which Wagner postulated to be an enhanced sticking coefficient/accommodation probability of the liquid. This effect does not consider the surface diffusion of species to the growth seed, which can be an important factor for the growth rate. For instance, the collection area of surface adsorbed species, which contribute to the wire growth, was determined using metal seeds with specific pre-defined spacing [49]. Using the dependence of the interwire distance on growth rate, it was concluded that 80 % of the contribution to nanowire growth InAs on InAs (111)B stems from diffusion of metal species on the substrate and side facets of the nanowires in the vapour growth process, as schematically shown in figure 3(c). Bergstrom *et al.* reported a synergistic effect during GaP wire growth, due to a specific collection area on the surface, the gas phase diffusion of pre-decomposed monomethylgallium (secondary collection volume) and the catalytic activity of gold in decomposition of trimethylgallium. The larger surface area of big gold particles leads to a higher concentration of catalytically decomposed species in their vicinity that is responsible for a higher growth rate of wires (figure 4) [50].

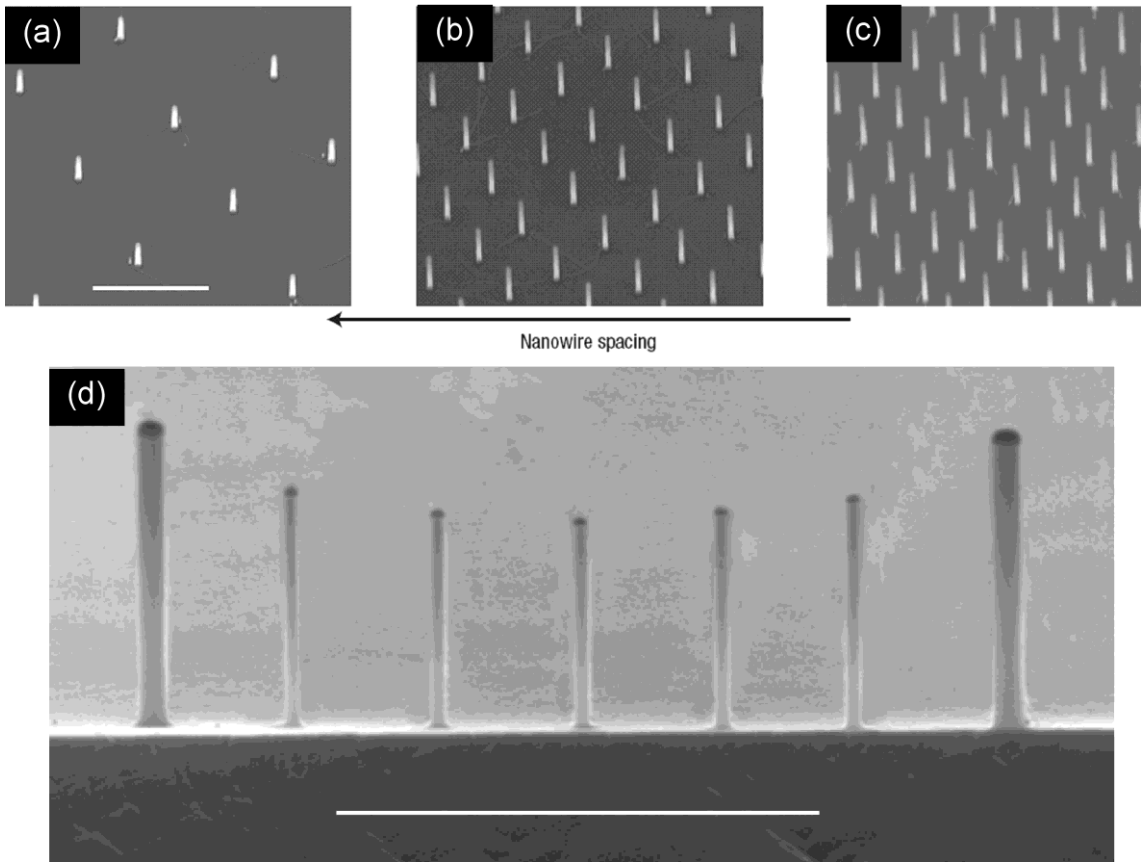

Figure 4. SEM images of GaP nanowire patterns. (a)–(c), An increase in the nanowire growth rate is observed by decreasing wire spacing L from (a), 1,000 nm to (b) 500 nm and (c) to 400 nm, for a constant nanowire diameter d of 25 nm. (d) Cross-sectional SEM image of nanowires grown from a pattern of gold catalysts with different sizes. Nanowires were grown from 25- and 100-nm catalysts with 300 nm spacing. Wires next to a thick wire are taller than the second-nearest wires, which are taller than those in the middle of the field (furthest from the thick wire), showing that the growth rate of one wire is enhanced by the presence of another one, and dependent on the amount of catalytic alloy. Nominal diameter values are used. Scale bar is 1 mm. Wires in the background have been removed graphically to clarify the effect. Reprinted by permission from Macmillan Publishers Ltd: Nature Nanotechnology [50], copyright (2007).

From figure 4, it can be concluded that physical surface processes must be considered in order to understand the growth of 1D nanowires. Axial and lateral growth may be treated as competing processes in metal-promoted vapour growth, if the substrate temperature is high enough to promote 2D film formation. The seed particle captures migrating species which cannot diffuse away and all growth material reaching

the particle will contribute to axial growth. Any material which cannot diffuse far enough to reach the metal particle will contribute to lateral growth. The important influence of growth parameters, such as substrate temperature as well as precursor composition and pressure, can be attributed to variations in the size of the collection area, which is defined by the migration length of the adsorbed species on a surface in vapour growth processes [51]. For instance, the diffusion length dependent variation of the nanowire composition is shown for the InGaAs system, which exhibits different group III ratios along the nanowire axis [52]. The indium species possess higher mobility on the GaAs surface, such that the wire is richer in In towards the seed particle. In addition, MBE growth of GaAs nanowires reveals the importance of growth conditions where the adatom diffusion on a GaAs surface from the substrate to the top of the NWs , considerably increases the length of NWs [53]. The growth of thin NWs (< 100 nm) is mainly controlled by the adatom diffusion and not so strongly by the adsorption on the drop surface in these studies. Similarly, MBE-grown Si NWs show a diameter dependent growth rate which correlates inversely with the wire diameter showing the important impact of diffusion processes during the growth of nanowires [45]. However, the growth method is an important factor for determining the actual diameter dependent growth rate, which is typically higher for thicker wires in CVD-based techniques [54].

Further remarkable findings were recently reported by Algra *et al.*, who described the reduction of twin defects and stacking faults in the controlled growth of InP nanowires [55]. For the InP wires, doping with zinc was found to promote the growth of zincblende nanowires with periodically twinned segments. Without the dopant pure wurtzite NWs with a high fraction of stacking faults were observed, which can be

attributed to a modification of the nucleation energy. The growth of these controlled twin-superstructures is dependent on the size of the growth seed and a reduction of the liquid–solid step energy by dopant-crystal-growth seed interactions. A simple VLS mechanism can be applied to the growth of Si nanowires by CVD, where the nucleation of a nanowire is initiated when the Si concentration exceeds the solubility limit in the liquid Au/Si alloy. However for compound materials the underlying mechanism is much more difficult to understand, because many of these do not form ternary (multinary) alloys with the metallic seeds (commonly transition metals and low melting group III and IV metals). In addition, the supply of the material coming from different sources, such as with precursors often used for the growth of III/V semiconductors, implies that all constituent materials do not have to be incorporated in the alloy particle to promote compound nanowire growth. For instance, several alloys of group III metals and Au are known, but no stable Au-As or Au-P is described. However the Au-promoted III/V nanowire formation is well known. The interpretation of the growth is quite complicated, due to the potential interaction of a Au-III compound with group V species, either by their incorporation into the particle at higher temperatures or by surface diffusion to the semi-liquid metal-semiconductor interface (figure 3(b)). Despite the fact that a termination of a nanowire with a globular particle is typically attributed to VLS growth, also a vapour-solid-solid (VSS) growth could be present, which is described for the formation of GaAs wires [56]. The metallic particle forms a solid alloy with the gallium component and the arsenic is probably transported through the interface between the seed particle and the nanowire. The small shape variations in the catalyst material at different temperatures used in MOCVD could be realised by surface diffusion of seed material to minimise the surface energy of the particle. Predictions of

potential 1D growth of binary or even more complex materials via an alloying between the metallic seed and the constituents is almost impossible due to the lack of information in terms of phase diagrams. This data is limited due to the fact that for each system a detailed study over a four-dimensional parameter space (pressure, temperature, and two relative material compositions) is required, which implies difficulties in prediction and interpretation of the nanowire growth based on this information.

Theoretical approaches are trying to justify and explain nanowire growth from alloys or non-alloying particles, although there is no universal explanation accepted yet. What these approaches have in common is that they treat the particle/crystal interface as a preferential nucleation site, with kinetically hindered growth on the substrate and side facets of the wire material. From an energetic point of view, the surface Gibbs energy increases during the displacement of the liquid droplet by the nucleating nanowire material [57]. However, wires grow merely if the surface energy of the solid is low, when compared to the liquid. Similarly Glas *et al.* calculated a gain in free energy by nucleation at the triple phase line (particle-substrate-gas) by a virtual shift of the nucleation event from the middle of the seed-substrate interface to the triple phase region [58]. The specific surface energies for different substrate materials must be considered when crystal nucleation events are investigated. For instance, nucleation could take place either by wetting the particle-substrate interface or by nucleation on the corner of the particle-substrate-gas triple phase region, which has been experimentally described for Si-III/V heterostructures (figure 5) [59]. The presented model relates the wire morphology to the nature of the nucleus, either island or layer-type, which is dependent on the relationship of the interface energies between two materials and the

catalyst particle. Dick *et al.* came to this conclusion assuming that the type of nucleus formed is analogous to planar 2D film growth.

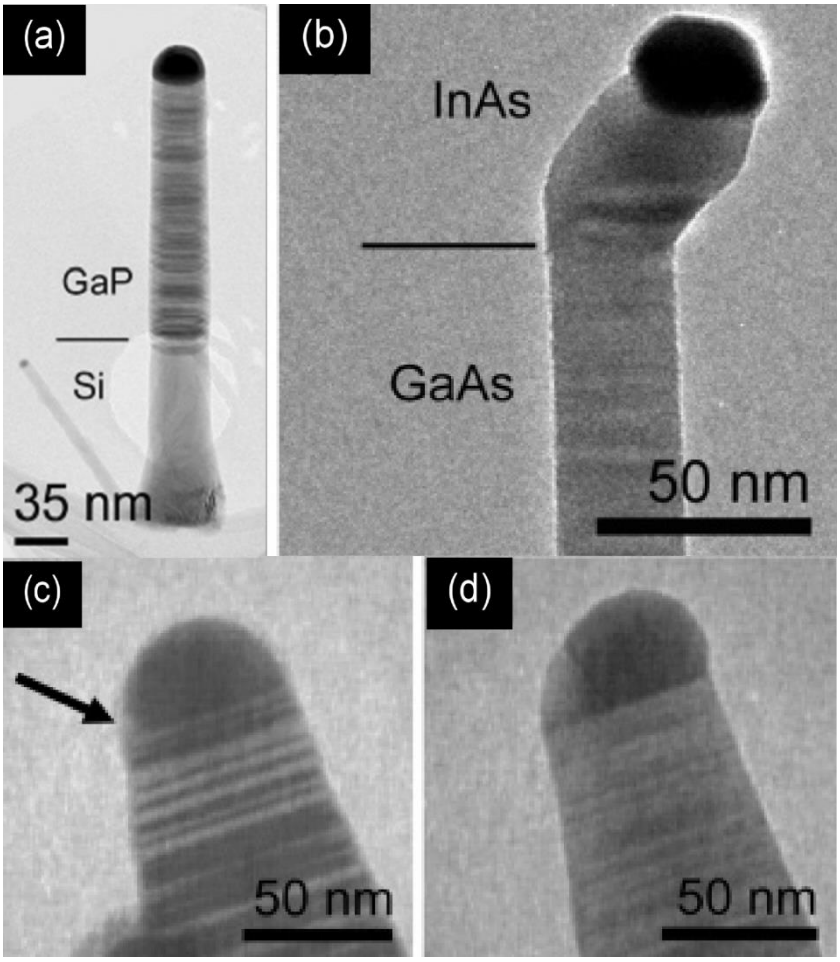

Figure 5. Examples of heterostructures formed by (a) wetting of the initial segment and (b) island formation of the second material at the seed nanomaterial interface leading to kinking of the wires. (c)-(d) shows an initial Ge island formation at the Au-GaP interface leading to kinked growth similar to the growth in (b). Reprinted from Ref. [59] with permission of ACS Publishers.

Another theoretical approach highlights that in the growth of nanowires the interface acts as the minimum point of curvature of the liquid droplet, with the lowest local mobility, and therefore promotes preferred nucleation [60]. The theoretical data obtained from this study does not restrict the particle to be in a specified state (liquid or solid), due to the assumption that the surface mobility is the highest on curved surfaces,

resulting in material transport to the interface induced by a material gradient. Another model by Dubrovskii *et al.* proposes that the Gibbs–Thomson effect plays a strong role in the energetics of nanowire growth, which can result in wurtzite being stable for small nanowire diameters in polytype materials, such as III/V semiconductors instead of the favourable zincblende crystal structure of bulk materials [61]. Small droplets with a high surface curvature exhibit a higher effective vapour pressure, which has to be overcome by gas phase supersaturation. Surface energy contributions are inversely proportional to seed radius and accounts for the Gibbs-Thomson effect of elevation of chemical potential in a NW of small radius, first modelled by Givargizov and Chernov [62].

In addition to the previously described examples several groups have reported the nucleation of semiconductor nanowires from solid metal particles. For instance, silicon nanowires have been grown from PtSi [63] and Cu [64] nanoparticles. Similar findings have been reported for Ge [65,66], GaN [67], ZnO [68], and GaAs [69] nanowires. The difficulties in attributing the growth of wires according to either the VLS mechanism or a solid particle (VSS growth mode) are shown by Kodambaka *et al.* [70]. In-situ TEM studies on the growth of Ge nanowires from Au growth seeds under UHV conditions, showed no size dependent melting effects, but strong hysteresis in melting-freezing cycles. In this respect, nanowire growth occurred even at 80 K below the expected eutectic temperature from an undercooled liquid. In addition, the phase diagram strongly depends on the pressure, which is generally not considered, but is of great significance, for materials synthesised under high or low pressure conditions. These investigations also showed the co-existence of VLS and VSS growth in neighbouring

wires. Advanced theories should be able to describe the observed phenomenon of nanowire growth in solid and liquid state of the seed particles with a single model.

Furthermore one should not neglect the potential surface diffusion processes of catalytic material leading to the tapering of wires due to catalyst shrinkage or growth, especially at high temperatures (figure 6) [71]. However, the diffusion can be affected by the growth conditions, such as the change of precursor supply [72]. The diffusion tendency of catalyst material is high for low precursor concentration and low for higher silane concentration. The higher silane adsorption onto the sidewalls of the nanowires in the latter case results in a suppression of the gold migration on the nanowire sidewalls. The addition of small oxygen concentrations during the growth of Si nanowires has a similar effect on the growth of Si nanowires by reducing the surface mobility of the diffusing catalyst on the side facets [73]. The formation of a surface oxide, which prevents migration tendencies, is also described for NWs that are exposed to oxygen containing atmospheres prior to annealing at higher temperatures [74]. In addition, the presence of surface diffusing gold species on Si is observed when there is a low supply of precursor species, leading to instability of the Au-Si alloy, which is accompanied by surface diffusion. Taking advantage of the metal seed migration allows the one-step growth of branched Si NW structures, by changing the experimental conditions during the process. Sawtooth faceting is also attributed to the presence of Au on UHV-grown Si NW surfaces, which is illustrated for (112) Si surfaces forming stepped and faceted surfaces depending on the coverage [75]. Comparing the results to the structure seen on the sidewalls of Si NWs, an overall Au coverage between 0.40-0.46 monolayers Au can be assumed to be a relevant concentration for sawtooth faceting and the driving force for the faceting events is the formation of energetically favourable Au rich (113) facets

and Au depleted (111) facets. Surface diffusion of Au seed material is also reported for other systems apart from Si [76] and additionally the incorporation of catalyst material in the growing wire should be taken into account, as this could alter their physical properties [77].

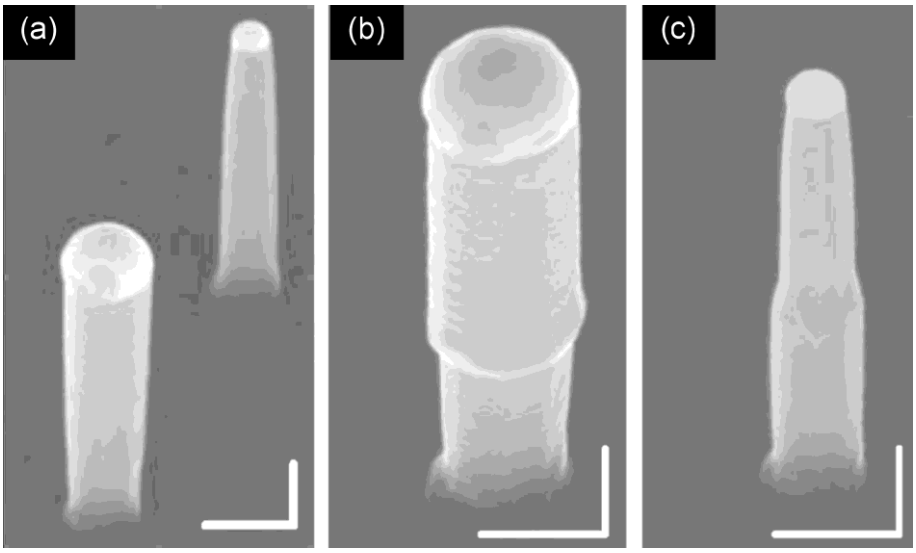

Figure 6. SEM images of (a) Si nanowires grown on Si(111) substrates, recorded with a 42˚ angle of incidence, coarsening of the catalyst particles leads to wires with diameters that either grow or shrink during nanowire growth. (b) and (c) Nanowires imaged after 30 mins of growth at 600 °C, followed by annealing at 650 °C for 20 min, and a final growth period of 25 min at 600 °C. Scale bars: 200 nm. Reprinted with permission from Macmillan Publishers Ltd: Nature [71], copyright (2006).

Despite the large body of data, the metal particle promoted growth of nanowires is not completely understood. Recently, carbon nanotube growth from silica [78] and diamond [79] nanoparticles has been described. This result is totally unexpected, as the formation of carbon nanotubes has traditionally been attributed to the carbon sticking coefficient and the catalytic behaviour of metal particles, which both can be altered by doping with small levels of impurities [80]. Similar to theoretical works described above, the authors attribute the activity of the 0D nanostructures to a high degree of curvature which can lead to partially melted particles or semi-liquid surfaces/interfaces

as shown in figure 3b. The non-metal nanoparticle-promoted carbon nanotube is a revolutionary discovery, which will lead to a broader knowledge and insight in the growth mechanism of 1D structures.

2.4 Metal-assisted growth in liquids

Metallic seed particles can support nanowire growth in a liquid environment, similar to the growth of nanowires on surfaces from a vapour phase. Depending on the synthetic conditions either a solution-liquid-solid (SLS), in the case of standard pressure [81], or a supercritical–fluid-liquid-solid (SFLS) mechanism under high pressures [82] can be predicted. In the SLS process the solvent requirements generally include a high boiling point liquid, which is stable up to 400 °C, and a low melting point metal growth seed (Bi, Sn, In, Bi/Au, etc). The pre-formed metal colloids act as nucleation seeds for decomposing metalorganic species and induce the nucleation of single crystalline wires, such as PbS as shown in figure 7 [83]. The metal-deposit interaction is similar to the VLS mechanism, which was already described in detail above. However the particle-solid interface has to be created as a first step, which is already present in conventional VLS processes.

Similar catalyst reactions are expected in a SFLS growth process, whilst the main differences are a higher temperature (< 550 °C), high pressures in the range of 200-300 bar and simple solvents, such as hydrocarbons (hexane and toluene) and CO_2. The main benefits of both synthetic procedures are the potential generation of small diameter 1D nanowires (4-10 nm) with narrow size-distributions in high yields. Catalytic particles may be chosen to broaden the range of viable precursors and to expand the parameter space, but not all appropriate particle materials are catalytic [84]. Similar to the solid

metal-promoted NW growth from gas phase, the nucleation of semiconductors by solid Ni is described by Tuan *et al.* [85,86].

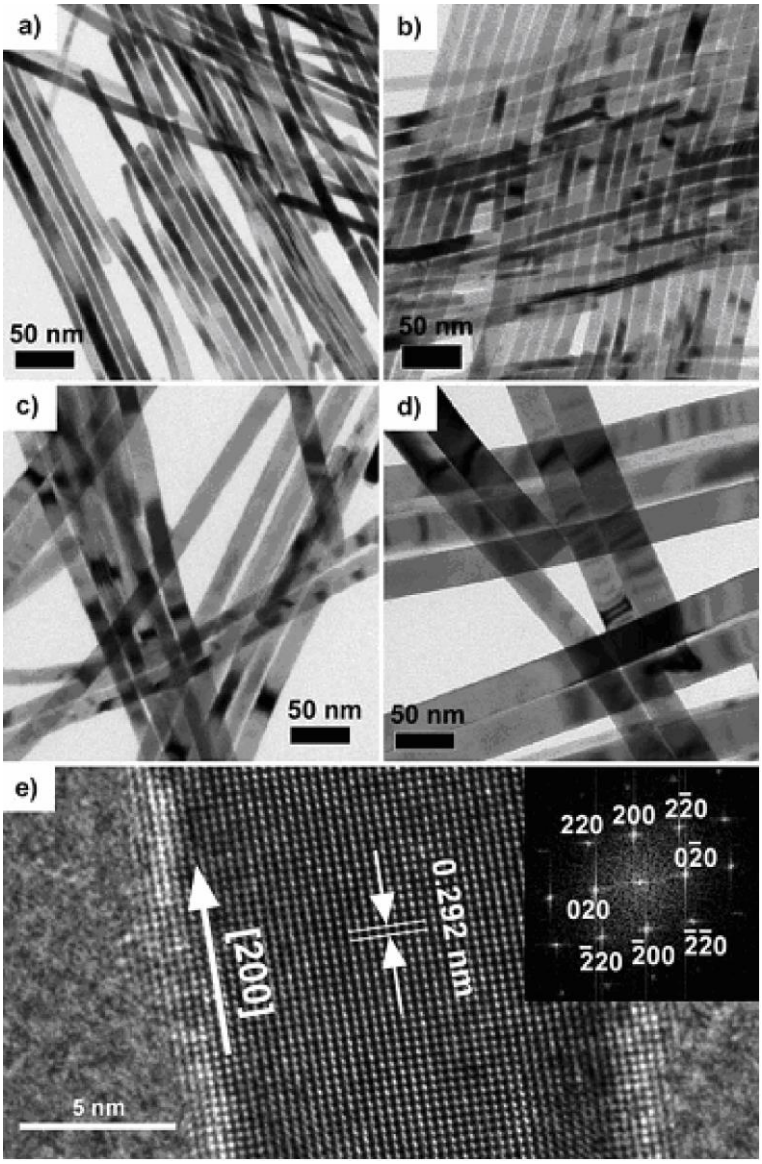

Figure 7. Representative TEM images of PbS nanowires of various diameters (d): (a) d = 8.7 ± 2.4 nm (± 28 %), (b) d = 11.2 ± 2.3 nm (± 21 %), (c) d = 16.1 ± 2.9 nm (± 18 %), and (d) d = 31.2 ± 3.9 nm (± 13 %). (e) A lattice-resolved HRTEM image of a 15 nm diameter PbS nanowire. The inset shows the indexed fast-Fourier-transform (FFT) pattern of the image, indicating that the nanowire grows along the [200] direction. Reprinted from Ref. [83]. Copyright Wiley-VCH Verlag GmbH & Co. KGaA. Reproduced with permission.

2.5 Template synthesis of nanowires/nanotubes

1D nanostructures can be generated by either filling or covering a host (template) structure, using a variety of techniques, resulting in hollow and solid nanostructures as schematically displayed in figure 10.

The most popular representatives of *hard templates* with pre-defined pores are AAO (anodic alumina oxide) and polycarbonate membranes, which can be filled or covered with a thin layer of the desired material from metalorganic precursor solutions and subsequent thermolysis [87], by electrolysis [88-91] or by ALD (atomic layer deposition) techniques [92]. In addition, high pressure injection [93] and supercritical fluid inclusion methods [94] or capillary force [95] are appropriate techniques to fill the pores with inorganic materials. Combined methods of metal particle promoted growth of wires within structure directing membranes are viable approaches to form aligned nanowire arrays by CVD [96,97] or supercritical fluid synthesis [98].

Advantages of the membrane based approach are the ability to guide the 1D growth of several material classes, either through chemical conversion of electrodeposited metallic wires or direct growth, and the solubility of the alumina/polycarbonate backbone in appropriate solvents, which enables the release of the as grown nanostructure. However, one drawback of this method is obviously the predominantly polycrystalline nature of the material. Positive replication, which means coating the outermost surface of 1D materials, such as carbon nanotubes or oxides, is also a prosperous technique [99]. In this approach the templating material can act as a removable skeleton, hybrid structure or second reagent for solid phase reactions [100].

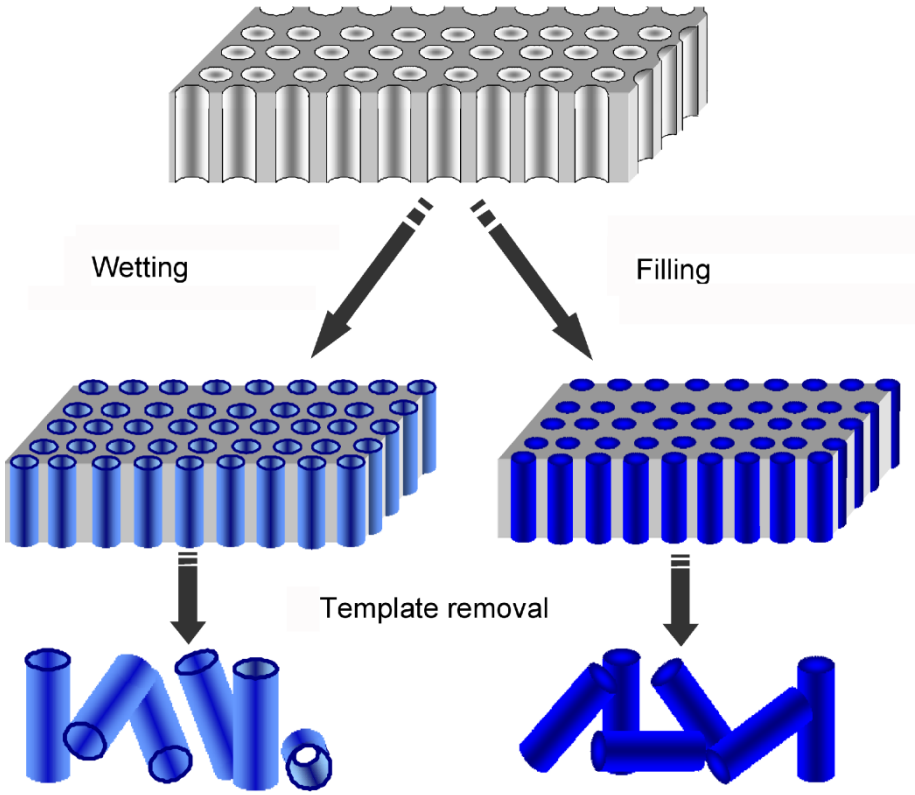

Figure 10. Schematic illustration of the membrane-based synthesis of nanotubes and nanowires. Removal of the hard template releases the nanostructures.

Soft templates are related to the use of surfactants to build mesophasic structures, which are formed by self assembly at critical micelle concentrations. Chemical reactions within this water-oil-surfactant system allow, similar to vesicular micelles, the synthesis of materials with diverse morphologies and aspect ratios [101]. For instance, $BaSO_4$ NWs were obtained in sodium bis(2-ethylhexyl)sulphosuccinate (Na-AOT) containing microemulsions by controlling the synthetic conditions, whilst the 1D shape of the nanostructures obtained was observed to be dependent on the irreversible fusion, unidirectional exchange and the coalescence of microemulsion droplets, followed by the crystallisation of an amorphous filamentous $BaSO_4$/surfactant phase [102]. In this respect, the composition of the two-phase/surfactant system plays an important role in the shape evolution of nanomatter by this approach [103]. In addition, the presence of

specific anions in the water-oil-surfactant system can trigger the evolution of different shapes and aspect ratios, which indicates that the micelle forming surfactant is not the only driving force for the 1D growth [104]. Therefore, selective ion adsorption on facets is an important factor for the crystal growth in potential soft templates such as inverse micelles and the presence of surfactants are mandatory [105,106].

2.6 Electrospinning

Traditionally *electrospinning* has been used as a method to produce polymer fibers, where the basic phenomena described by Bose [107] (aerosol generation by electric charges) and Rayleigh [108] (required charge density to overcome surface tension of a liquid) are applied to achieve charge carrier transport via a liquid jet. A high voltage is applied to a capillary through which a polymer/solvent mixture is guided and a metallic plate acts as counter-electrode and collector. Above a critical field force charge carrier transport emerges due to a fluid string between the electrodes, which forms the fibres on the metallic counter-electrode via evaporation of the solvent during the tavelling of the jet between the electrodes. For the synthesis of inorganic nanowires a triphasic solute (solvent, polymer and precursor) is used, which either includes metalorganic monomers or pre-formed particles [109]. However the spun fibres are generally organic-inorganic hybrids, which are either used as obtained [110] or transferred in a purely inorganic material by calcination. The approach can be used for various particle-polymer combinations, however the pure inorganic materials are generally polycrystalline oxides due to the requirement of the oxidative removal of the organic structural backbone. An alignment of electrospun fibres was demonstrated for tailored collector/substrate electrode configurations, which also showed the formation of different mesh geometries

[111,112]. Core-shell and hollow nanostructures can be obtained by an advanced assembly using two combined injection capillaries and liquids. The interdiffusion of both liquids in the area of the capillary and during the electrospinning should be prevented to form co-axial polymer fibers or inorganic tubes. Tubular 1D nanostructures can be spun by use of mineral oil as one of the sources to form the hollow core and the other shell forming polymer, which prevents the collapse of the jet during the electrospinning process [113-115].

2.7 Top down approach / chemical etching

The most important top-down process for controlled 1D nanostructure formation is the chemical etching technique, which is eligible for use with many materials and especially suitable for elemental semiconductors. Top-down techniques have improved within the last 5-10 years and are nowadays able to obtain structures at the nanoscale (< 20 nm) [116], however several growth steps are required and involve photoresist deposition/removal and the chemical or ion beam etching [117]. Due to facet dependent etching rates, predefined shapes can be produced from preliminary masked areas, which has been demonstrated for compound semiconductors such as InP and GaAs (figure 11) [118].

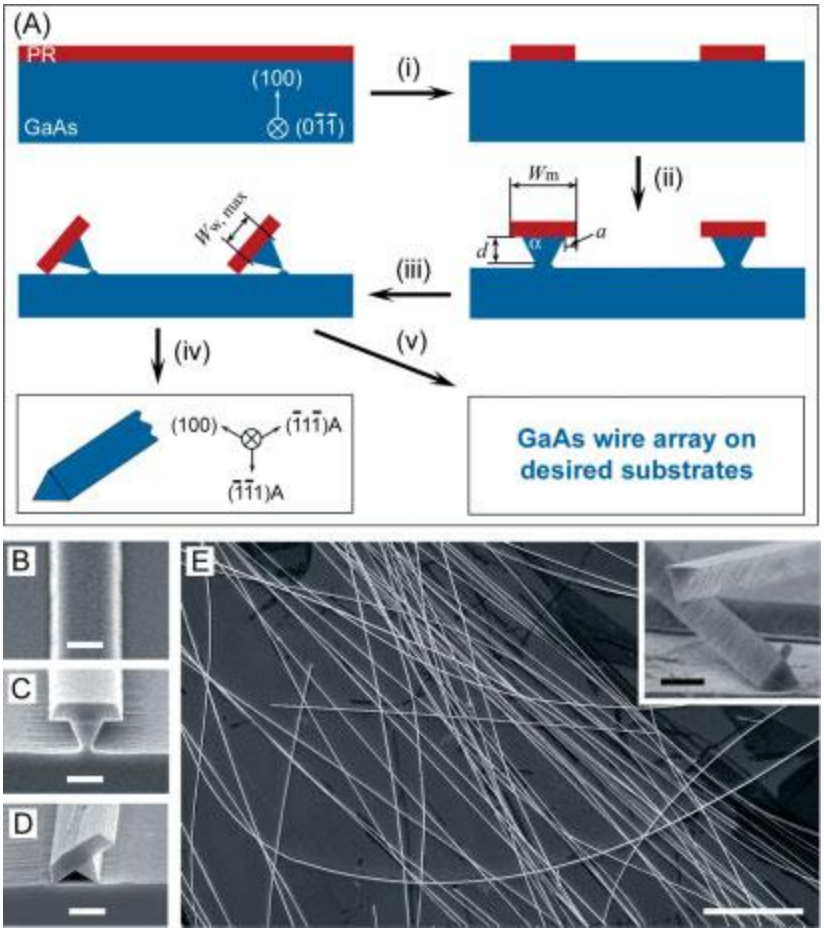

Figure 11. (A) Schematic illustration of the process for generating nanowires from a high quality bulk single crystal GaAs wafer. The major steps include: (i) defining the patterned photoresist (PR) stripes on the GaAs wafer; (ii) anisotropic chemical etching of the GaAs wafer using the PR stripes as a etch mask; (iii) continuous etching of the GaAs wafer, with the formation of released GaAs wires; (iv) removing the PR using acetone and/or O_2 plasma and (v) transferring the GaAs wire arrays from the mother substrate to another desired surface. (B)-(E) SEM images of nanowires at different stages of the fabrication process: (B) PR stripes on a GaAs wafer before etching, (C) cross section of a reverse-mesa capped with a PR stripe, (D) cross section of a released GaAs wire resting on the mother substrate against the bottom edge of the GaAs wire and one edge of the PR stripe and (E) a random assembly of GaAs nanowires after removal of the PR stripes (scale bar 50 μm). The inset in (E) shows the triangular cross section of the GaAs nanowires. Scale bars in (B)-(D) and inset in (E) are 1 μm. Reprinted from Ref. [118]. Copyright Wiley-VCH Verlag GmbH & Co. KGaA. Reproduced with permission.

Lift-off of the wires and their transfer to virtually any surface is also demonstrated [119]. The pre-orientation achieved by this technique is superior to the methods described above, because post-alignment by Langmuir-Blodgett or similar approaches

as described in section 4 is not necessary. The etching solution removes material at the exposed area, which is not covered by a mask. Another site-selective chemical etching can be induced by metals such as silver and gold, which promote/catalyze the removal of material at the Si-metal interface [120]. Moreover an excellent control of the doping level is ensured due to established techniques for thin film and bulk single crystal technology, such as wafer bonding, which allows to create high density of diodes by using sandwich structures [121]. A critical step for the etching of nanostructures is the accurate transfer of mask features to the surfaces, which becomes complicated for high density arrays and very small feature sizes and will limit the progress in this area using conventional approaches.

3. Synthesis of Si, Ge, GaN, GaAs, CdS, ZnO and SnO_2 1D nanostructures

Inorganic semiconductors spanning a large variety of material classes are known to act as active components in functional devices. We have summarised in this section reliable strategies (table 1) for the synthesis of the most popular semiconductors for nanowire-based sensors, energy related applications and nanophotonics.

Table 1: Synthetic strategies for the synthesis of high aspect ratio 1D semiconductors.

Semiconductor	Bandgap bulk	Synthetic strategy	1D morphology	Reference
Si	1.12 eV	CVD	NWs	[40, 41, 64, 71, 97 122-143]
			NBs	[144]
		Laser ablation	NWs	[34, 38, 145, 146]
		MBE	NWs	[45, 147, 148]

		Physical transport	NWs	[149-155]
			NBs	[156]
		Template synthesis	NWs	[157-161]
			NTs	[162]
		Solvent / SCF	NWs	[82, 84, 163-165]
		Etching	NWs	[116, 166-171]
			NBs	[172-173]
Ge	0.97 eV	CVD	NWs	[65, 66, 70, 122, 174-184]
		Laser ablation	NWs	[34, 36, 145]
		Physical transport	NWs	[185-189]
		Template synthesis	NWs	[94, 98, 158, 159, 190]
		Solvent / SCF	NWS	[85, 191-196]
		Etching	NWs	[197]
GaN	3.36 eV	CVD	NWs	[67, 198-212]
			NBs	[213]
		Laser ablation	NWs	[214-217]
		Template synthesis	NWs	[218, 219]
			NTs	[220, 221]
		Etching	NWs	[222]
			NBs	[223]
GaAs	1.43 eV	CVD	NWs	[56, 69, 224-229]
		Laser ablation	NWs	[230]
		MBE	NWs	[41, 231-233
		Solvent / SCF	NWs	[81, 234, 235]
		Etching	NWs	[118, 119, 236-238]
CdS	2.42 eV	CVD	NWs	[239-242]
		Laser ablation	NWs	[230]
		Physical transport	NWs	[243-249]
			NBs	[247-255]
		Template synthesis	NWs	[256-260]
			NTs	[261, 262
		Solvent / SCF	NWs	[83, 263-268]
ZnO	3.37 eV	CVD	NWs	[269-273]
		Laser ablation	NWs	[230, 274, 275]
		MBE	NWs	[276]
		Physical transport	NWs	[30, 31, 277-278]
			NBs	[279, 280]
			Helices/Rings	[32, 33, 281-283]
		Carbothermal	NWs	[284-292]
			NBs	[[293-295]
		Template synthesis	NWs	[88, 296]
		Solvent	NWs	[297-301]
		Electrospinning	NWs	[302-305]
SnO_2	3.6 eV	CVD	NWs	[306-314]
			NBs	[309, 312, 315, 316]
		Laser ablation	NWs	[317]
			NBs	[318]
		Physical transport	NBs	[319, 320]
		Carbothermal	NWs	[321-324]
			NBs	[325]
		Template synthesis	NWs	[326. 327]
		Electrospinning	NWs	[328-330]

3.1 Silicon

Various synthetic methods have been established for growing Si nanowires, after the initial discovery of high aspect ratio silicon micro- and nanostructures in the 1960's by Wagner's group [40]. Silicon nanowires are typically synthesised nowadays using metal-assisted growth techniques, with a combination of different metal growth seeds and silicon sources. The most popular method for growing Si NWs is by CVD of gaseous sources, such as silane SH_4 [122,123], disilane [71], and silicon tetrachlodide $SiCl_4$ [40, 124, 125]. An improved decomposition of the silicon source can be achieved by plasma enhanced CVD techniques, which permits a pre-cracking and weakening of the chemical bonds in the gaseous molecules before material deposition on a substrate [126]. The growth rate of Si NWs also increases in changing from SiH_4 to Si_2H_6, which enables the growth of millimetre-long Si NWs with uniform electronic properties along their wire axis [127]. In addition, physical evaporation techniques of pure silicon sources by pulsed laser deposition (PLD) [145, 146], by MBE [147, 148] and by thermal [149] as well as electron beam evaporation [150, 151] have been demonstrated as suitable processes for VLS-based nanowire growth. Thermal evaporation of SiO powder followed by its disproportionation to form Si/SiO_2 core-shell nanowires is reported in the presence [152] and absence [153] of gold seed particles. The metals which have been reported to promote the VLS growth of Si nanowires include Ni, Cu, Pd, Ag, Pt, Ga, In, Al, Zn, Fe and Sn [40, 124, 136, 138, 139, 145]. A solid metal seed particle induced vapour-solid-solid growth is reported for Ti and Dy [137]. The general growth direction for VLS-grown Si nanowires with diameters > 50 nm is <111>, however a change of the preferential growth direction with diminishing radial

dimensions is described, which results in <112> and a majority of <110> oriented wires for diameters below 20 nm as shown in figure 12 [140].

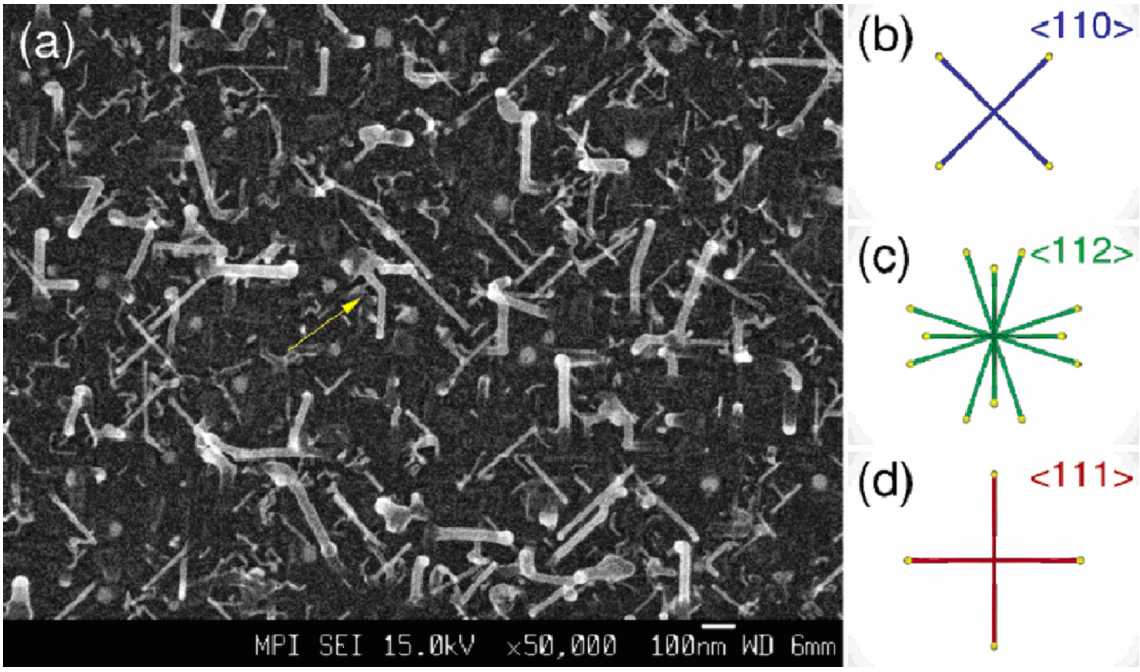

Figure 12. (a) SEM of thickness dependent growth direction of Si NWs on Si(100) with schematic illustration of crystallographic orientations of wires (b-d). Reprinted from Ref. [140] with permission of ACS Publishers.

Similar findings are described for Si nanowires grown from Pt (< 10nm) seed particles which promote predominatly <110> wire growth [141]. This result is also supported by theoretical investigations based on the nucleation thermodynamic model which considers the orientation-dependent surface and interface energies of Si NWs. For Si NWs there is a threshold diameter of ~25 nm for a switch between the preferred <110> growth direction to the <111>-oriented wires for larger radial dimensions [331]. Interestingly, the fast growth rate using disilane, in a Au-promoted CVD process, results in predominately <110> oriented nanowires in the diameter range between 20-80 nm, which is attributed to potential kinetic effects on the growth direction [127].

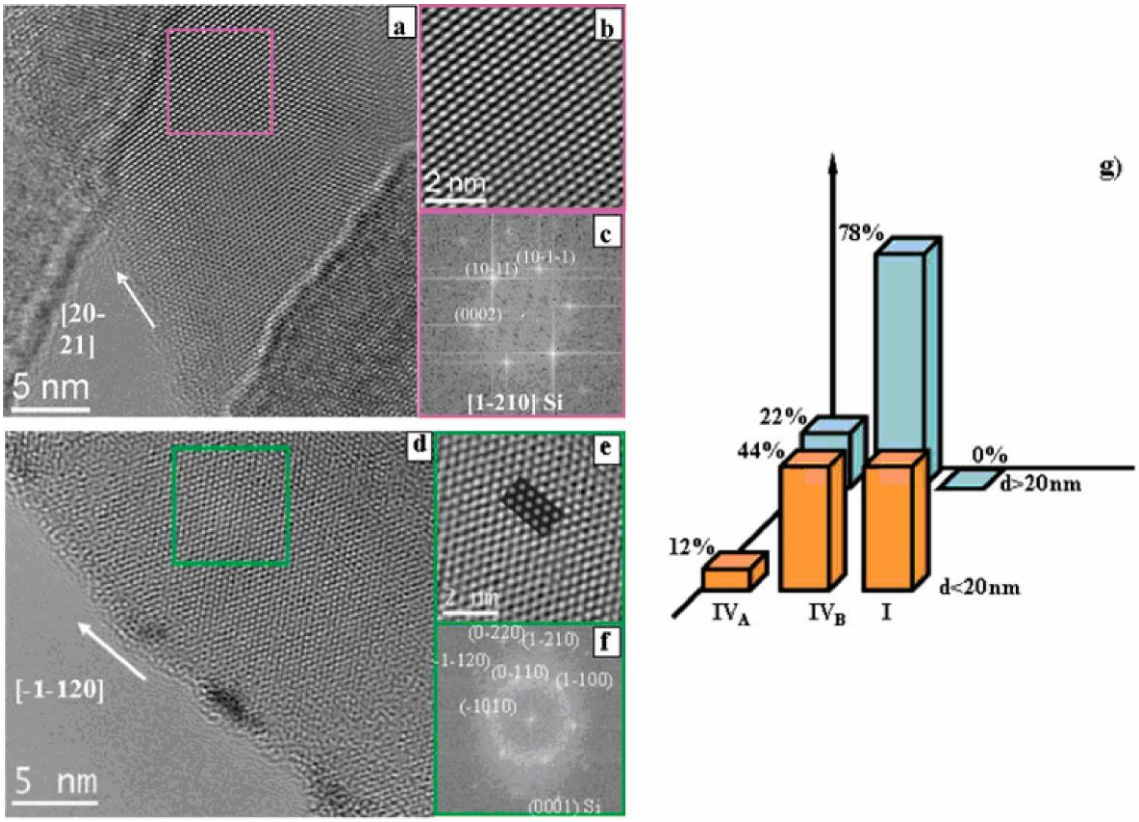

Figure 13. Detailed structural analysis of Si NWs. (a) HRTEM image of a wurtzite-type Si NW, (b) magnified detail of the squared region in (a). The inset shown in (b) corresponds to a HRTEM computer simulation of the hexagonal Si crystal structure obtained from a 3D atomic supercell model reproducing the thickness and focus conditions observed experimentally. (c) Power spectrum (FFT, Fast Fourrier Transformation) of the crystalline structure. From the FFT, the distances and angles between the planes are calculated to determine the crystalline structure of the nanowire and its growth direction. (d) HRTEM of a Si NW. (e) Magnified detail of the squared region in (d). (f) Power spectrum of the crystalline structure. (g) Statistics of the crystalline structure for NWs with diameters smaller than 20 nm and between 20 and 100 nm. (I represents the percentage of nanowires with cubic crystal structure and IV indicates the percentage of Si nanowires crystallized in a hexagonal lattice. Above 100 nm it is difficult to obtain good-quality HRTEM measurements). Reprinted from Ref. [143]. Copyright Wiley-VCH Verlag GmbH & Co. KGaA. Reproduced with permission.

Si NWs with a <100> growth direction, which are typically difficult to synthesise, have been produced using a guided homoepitaxial growth process on a Si (100) wafer. A thin AAO membrane on the Si substrate was used as a template in a CVD process to generate the nanowires [142]. Tendencies of cubic bulk materials to form hexagonal lattices are well described in theory and recently Morral *et al.* have demonstrated that

silicon NWs in wurtzite phase could be grown using silane based CVD on gold coated silica surfaces (figure 13) [143]. The authors describe two different wurtzite modifications which differ slightly in their unit cell parameters and their total percentage is dependent on the wire diameter, with a total absence of diamond Si NWs in the diameter range between 20-100 nm (figure 14). However, these data require careful interpretation as outlined by Cayron *et al.*, who question the existence of a hexagonal silicon crystal lattice [332]. They related the odd electron diffraction pattern to microtwins which induce extra spots by double diffraction, and nanotwins which induce extra spots as a result of streaking effects. In addition, this investigation includes simulated diffraction pattern which match well in position and intensity to the spots from the observed experimental data for Si NWs and thin films.

Suitable precursors for solvent based electroless synthesis are generally trisilane and heteroleptic aryl-substituted silane precursors. Filling of mesoporous membranes was achieved by supercritical fluid inclusion techniques, which allows an effective filling of the pores by decomposition of monophenylsilane in supercritical CO_2 [157]. Electrolytic deposition of amorphous Si nanowires in polycarbonate membranes, with diameters between 400 to 15 nm, was achieved using a solution of $SiCl_4$ in ionic liquids under mild conditions [158, 159]. The polycarbonate template could be easily removed by dissolution in organic solvents, releasing the pure Si wires without any surface modification. Solution-based techniques have also successful in growing Si nanowires via SFLS and SLS mechanisms. Au growth seeds in supercritical organic solvents are able to induce the formation of single crystalline Si nanowires, with diameters between 5-10 nm [82]. Moreover solid phase seeding of Si wires is also described for several compounds including Co, Ni, Mn, CuS and MnPt in supercritical toluene [84].

Recently, Si nanowires were seeded by Au and Bi nanoparticles in high boiling solvents, octacosane ($C_{28}H_{58}$) or squalane ($C_{30}H_{62}$) via decomposition of trisilane, which can be attributed to a SLS type growth [163].

The most popular top-down approach for the synthesis of high aspect Si nanostructures is wet chemical etching, which can be used to fabricate aligned arrays in plane to a substrate surface, as well as in different angles out of plane. The site selective etching is in most cases induced by metal promoted (Ag, Au etc) oxidation and dissolution of the SiO_2 by hydrofluoric acid [120,166]. This wet etching technique allows nanowire formation either without or within a template, with the latter allowing the formation of nanowires with narrow size distribution [167]. Metal-assisted wet-chemical etching of silicon substrates in combination with nanosphere lithography is considered to be a viable low cost approach for positioning aligned Si NWs, with controllable diameters, lengths, spacing, and density [168, 169]. The hexagonal array of nanospheres acts as a patterning mask for a thin metallic film, which allows the etching of vertically and tilted aligned (100)- or (111)-oriented Si NWs with predefined diameters through the size of the holes in the metal film (figure 14).

The selective size reduction of lithographically created Si NWs can be achieved by etching the nanowires with a mixture of aqueous hydrofluoric acid and ethanol (50 %) and careful optimisation of the etching process by additional photogeneration of charge carriers which help to tune the etching reaction into an appropriate regime [170]. It should be noted that electrical connections to each end of a nanowire are vital to properly set the etching conditions with this method and that the electrical characterisation of these devices can be performed during the ongoing etching process. Highly aligned arrays of Si NWs, with radial dimensions as low as 18 nm and pitches of

30 nm, have been obtained by the superlattice nanowire pattern transfer (SNAP) process, followed by etching through SOI layers [116]. This unique method uses a metallic line pattern deposited on the initial mask, which is obtained by selective etching of segments in a GaAs/AlGaAs superlattice. The tilted geometry during metal deposition also reduces the line spacing between segments. In the next step the pattern is transferred to the silicon which is covered with an adhesive layer and reactive ion etching allows removal of the material between the metal lines. This methodology allows the fabrication of nanowires with lengths exceeding the 100 μm range and conductivity values comparable to bulk Si [171].

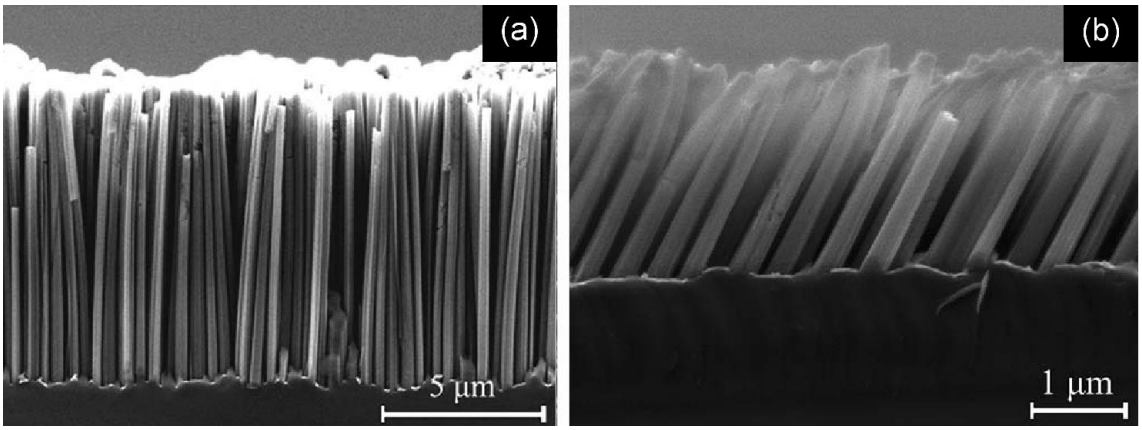

Figure 14. Cross-sectional SEM images of (a) vertically aligned ordered Si NWs produced on a p-type (111) substrates and (b) tilted aligned SiNWs produced on an n-type Si (113) substrate by wet etching techniques. Reprinted from Ref. [169] with permission of American Institute of Physics.

3.2 Germanium

The techniques to synthesise high aspect ratio Ge nanostructures are similar to those described for Si. The most common technique is the catalyst-assisted chemical vapour deposition using Au nucleation centres and traditional sources such as germane GeH_4 [122, 174]. Homoepitaxial NW growth only occurs at temperatures close to the eutectic temperature of the bulk Ge-Au alloy, whereas non-epitaxial growth can be observed at

temperatures as low as 280 °C [65]. In addition, chemical transport via iodide [175] as well as physical transport of metallic Ge via PLD [145], thermal evaporation with [185] and without a carbon additive to increase the surface area [186] are reported to permit the formation of 1D Ge nanostructures. The Au seed particle can be easily removed after NW growth by non-destructive etching using triiodide containing hydrochloric acid (figure 15) [176]. Remarkably, indium catalysed Ge nanowires exhibit a preferential <110> growth direction on insulators, while generally <111> oriented nanowires are reported for Au promoted growth, which are also reported for In-seeded Ge NWs on silicon [177]. In contrast to silicon precursors, germanium aryls can also serve as sources for the formation of nanowires. CVD using diphenyl germanium forms wires via a base growth model on steel [178] or via VLS based Ni catalysed growth [179]. Solution-based techniques include supercritical inclusion techniques to fill AAO membranes or channels in mesoporous thin films with [98] and without [94, 190] gold seed particles by the decomposition of diphenyl-germane. The electrolysis of $GeCl_4$ in ionic liquids, such as 1-butyl-1-methylpyrrolidinium bis(trifluoromethylsulfonyl)amide, permits the electrodeposition of amorphous Ge wires in polycarbonate membranes [158, 159]

The reduction of germanium chloride by sodium at elevated temperatures and pressure forms 1D Ge structures, where the intermediate growth could be initiated by a liquid sodium droplet via VLS-type growth [191]. SFLS techniques using gold [192], and Ni [85] seeds in supercritical hydrocarbons are described by Korgel's group. Besides the typically used germanium alkyl hydrides, germanium aryloxides [193] also proved useful for growing 1D Ge nanostructures via a similar approach in supercritical solvents. Decomposition of diphenyl-germane and germanium diiodide in high boiling

point solvents in the presence of Au [194] and Bi [195] seeds have been proven to be an alternative synthetic procedure to grow Ge nanowires via the SLS mechanism.

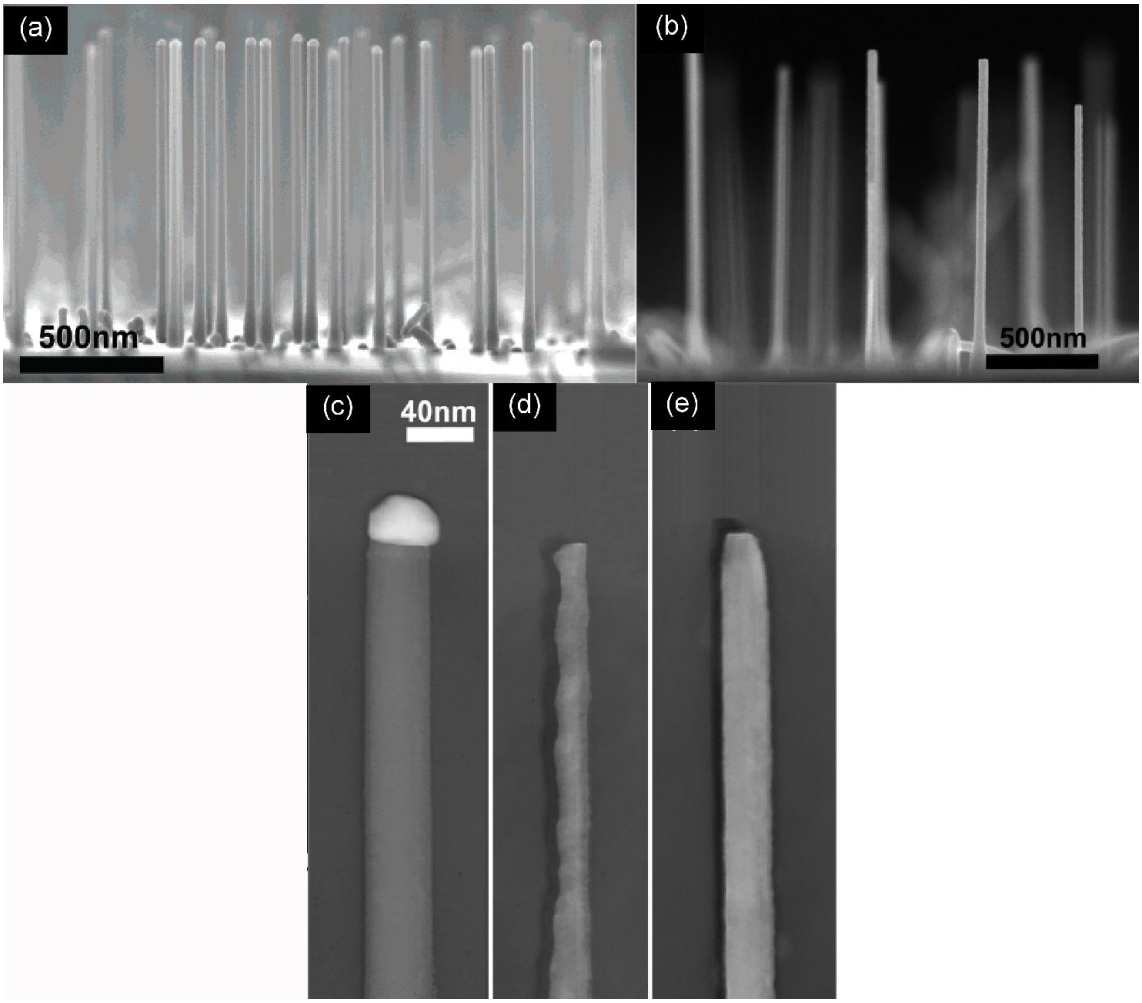

Figure 15. Cross sectional SEM images showing (a) Ge NWs grown from 40 nm gold colloids showing the growth seeds at the end of the wire and (b) an array of Ge NWs after removal of the gold particle without damaging the wires. Bright-field TEM image of (c) a nanowire prior to etching showing the gold catalyst at the tip, (d) a damaged Ge NW after treatment with an aqueous triiodide solution, and (e) removal of Au with minimal etching of the nanowire using an aqueous triiodide solution containing HCl. Reprinted from Ref. [176] with permission of ACS Publishers.

Electrochemical etching techniques take advantage of controlled pore formation on single crystal Ge in aqueous HCl electrolyte solutions [197]. Operating in the dark and at low temperatures is mandatory to ensure a high leakage current through pore walls,

which leads to their constant dissolution and the formation of individual wires by the merging of pores. Due to the random pore formation the cross section of different wires is rather irregular and controlled by the location of the initial pores formed.

3.3 Gallium Nitride

GaN is an important wide bandgap semiconductor in industrial applications such as amplifiers, light emitting diodes and transistors. The formation of 1D GaN nanowires, via the CVD of gallium and ammonia as source materials, has been demonstrated at temperatures between 800-1050 °C using several metal growth seeds, such as In, Co, Ni, Fe, Ni/Co, and Fe/Co [198, 199]. Moreover, metallic gallium / gallium oxide mixtures [200] and gallium acetylacetonate [201] have been used as metal sources in CVD processes with the same nitration agent (ammonia). The combined evaporation of gallium and a dopant source of solid Mg_3N_2 in flowing ammonia allows the growth of p-doped GaN nanowires via nickel seeded CVD techniques [202]. However, the use of a solid Ga source can yield non-continuous vapour pressures, whereas the metalorganic CVD approach, using trimethylgallium with ammonia at elevated temperatures, is a viable strategy to achieve controlled growth of gallium nitride nanowires [203]. The shape of the wires can be changed between triangular and hexagonal cross-section by selecting the appropriate substrate materials such as γ-$LiAlO_2$ and (111) MgO, respectively, which also allows the formation of highly aligned arrays of nanowires (figure 16) [204]. Nanobelts of GaN have also been grown using similar synthetic strategies, such as nickel seeded CVD of gallium and NH_3 [213].

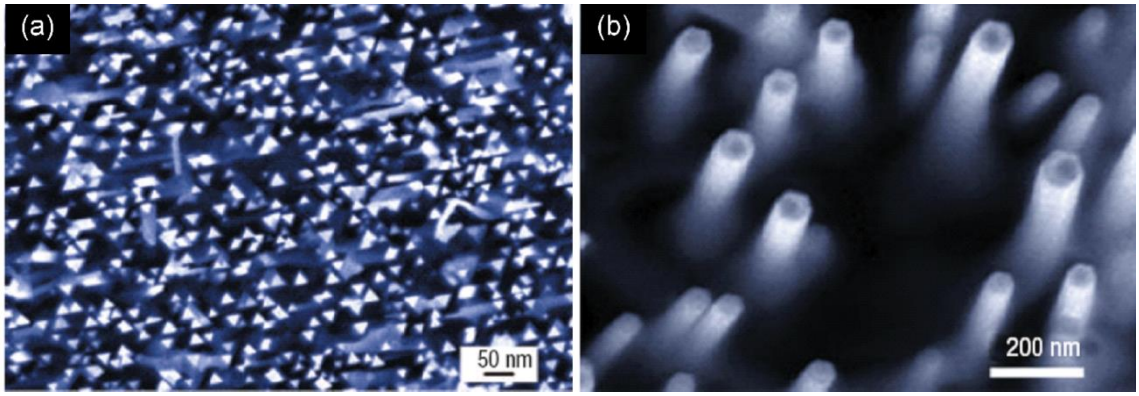

Figure 16. Aligned GaN NWs showing triangular cross sections on γ-$LiAlO_2$ substrates and hexagonal cross sections on on (111) MgO substrates. Reprinted by permission from Macmillan Publishers Ltd: Nature Materials [204], copyright (2004).

Laser ablation of GaN/Fe targets [214] or GaN/Ga_2O_3 [215, 216] sources are suitable for the growth of GaN NWs, via a metal-supported or oxide-assisted formation process, respectively. The iron seeded GaN nanowires were n-type semiconductors and showed gate-dependent conductance variations exceeding 3 orders of magnitude when used in FET device configuration [217]. Filling structure directing templates containing indium growth seeds by gas phase synthesis using gallium/gallium oxide mixtures in NH_3 also permits access to single crystalline nanowires of specific radial dimensions [218]. Nanotubes have been formed in AAO membranes by the CVD of trimethylgallium and ammonia as a polycrystalline replicate of the oxide template [220]. Single crystalline gallium nitride nanotubes have been grown via the CVD approach using aligned ZnO nanowire assembly as a mask [221]. The epitaxial relationship between the oxide and the growing GaN allows the formation of hollow structures by subsequent removal of the ZnO nanowire templates by thermal reduction and evaporation.

Early etching techniques use photo-electrochemical processes to selectively remove material between dislocations, which are present in n-type GaN films [222]. Recently, inductively coupled plasma etching using a polymer mask is described to permit the

formation of GaN belt-like structures from thin films, which can be released from the underlying Si substrate by wet etching techniques and printed to other surfaces [223].

3.4 Gallium Arsenide

Gallium Arsenide, GaAs, is one of the most promising III/V semiconductors for devices such as LEDs, lasers, field emission transistors, and monolithic microwave integrated circuits. However, gallium arsenide is polytype like all the III/V semiconductors, which implies it can either crystallise in a zincblende (cubic) or a wurtzite (hexagonal) structure. Thus, a common problem is the formation of stacking faults in the growth of these nanostructures, which cause effects like strong non-radiative recombination and decrease the luminescence efficiency in optical devices based on nanostructured GaAs.

The most popular technique for growing GaAs nanowires is by metal organic vapour phase epitaxy (MOVPE), using trialkyl gallium and arsine or alkyl arsines as precursors via a catalyst supported growth [224, 225]. However this process seems to be a vapour-solid-solid (VSS) growth and not a traditional VLS growth mode, where the arsenic compound does not mix with the metallic seed particle and diffuses at the interface between the seed particle and the nanowire to form GaAs [56]. Surprisingly, an enhanced growth rate reduces the twinning in the wires in a Au seeded growth mode, which is exactly the opposite to conventional planar epitaxy of bulk materials [226]. The catalyst-free formation of GaAs nanowires under similar conditions was achieved by site-selective patterning of a GaAs substrate with a SiO_2 film, which enabled the epitaxial growth of nanowires on the uncovered areas with higher growth rates [227].

Physical vapour growth of GaAs nanowires using gold metal seeds is described by laser ablation from GaAs substrates [230] and MBE techniques using metal sources [41]. Additionally, MBE allows the self-seeded growth of nanowires on silicon oxide coated GaAs substrates due to nanowire self-nucleation from Ga droplets as described for microwires by Morkoc *et al.* [231]. Oriented growth of NWs can be achieved by using very thin silicon oxide coatings (< 30 nm) due to a prior reaction of Ga metal with SiO_2 pinholes leading to microcraters and therefore contact to the III/V substrate as shown in figure 17 [232].

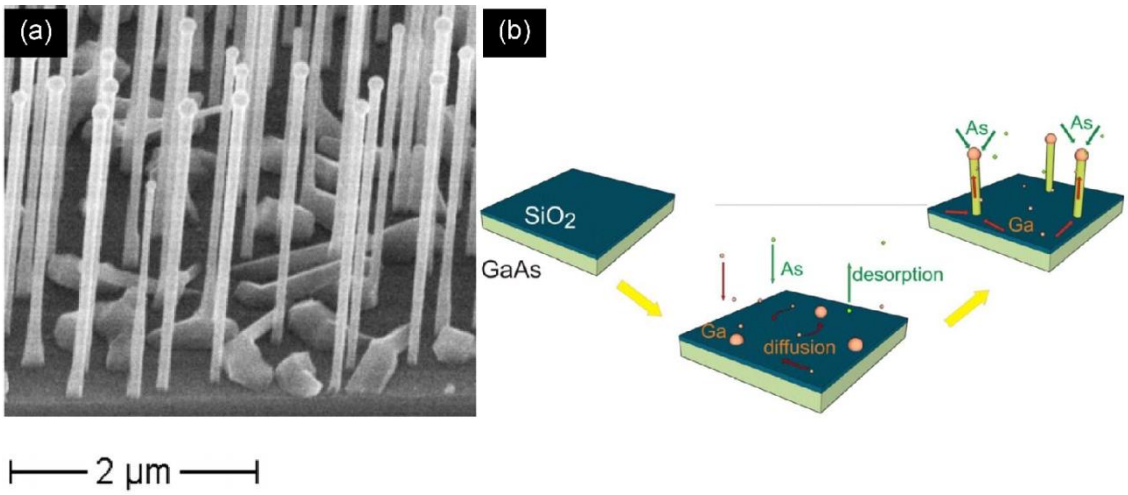

Figure 17. (a) Scanning electron micrograph of MBE grown GaAs nanowires on a (111)B GaAs substrate sputtered with a 10 nm SiO_2 layer and (b) schematic of the proposed growth model. On the SiO_2 surface, the seeds of the GaAs nanowires nucleate at pinholes of the SiO_2 and grow, being continuously fed by the Ga adatoms that diffuse from the neighbouring SiO_2 surface owning a low sticking coefficient for Ga at elevated temperatures, and form a droplet on top of the nanowires. The As_4 molecules impinging on the Ga top droplet contribute to the axial growth of the nanowires. Reprinted with permission from [232]. Copyright (2008) by the American Physical Society.

GaAs nanowire formation by SFLS synthesis requires two separate sources such as $As(SiMe_3)_3$ and $Ga(tBu)_3$ and a colloidal gold catalysts to initiate and promote 1D formation [234], whereas the SLS method uses identical precursors with In catalyst particles, due to the lower melting temperatures of the growth seeds [81, 235].

Chemical, anisotropic etching of wafer-sized GaAs substrates with H_3PO_4, H_2O_2 and H_2O in combination with lithography allows pre-definition of horizontal arrays of nanowires, which can be transferred onto plastic substrates and used in nano-macroelectronics [119].

3.5 Cadmium sulfide

Among II/VI semiconductors, cadmium sulphide is one of the most studied compounds due to applications in photoresistors, solar cells, lasers, infrared wave guides and splitters. The thermal decomposition of $Cd(S_2CNEt_2)_2$ [239] and $Cd(S_2CNProp_2)_2$ [240] in a low pressure CVD process on gold seeded substrates results in the formation of single crystalline CdS nanowires. Atmospheric pressure CVD, using $CdCl_2$ and elemental sulphur as precursors, produces CdS nanowires on gold coated substrates [241]. The resublimation of CdS powders at elevated temperatures and Ar atmosphere with [243,244] and without gold seeds [245, 246] forms CdS NWs. Similar synthetic conditions are described for CdS nanobelt synthesis, which indicates a narrow synthetic window allowing the selective formation of nanowire and nanobelts by this process [247]. Differences in temperature and vapour pressure lead to the formation of CdS nanobelts at higher and nanowires at lower temperatures in Au catalysed growth in the physical vapour deposition chamber as shown in figure 18 [248, 249].

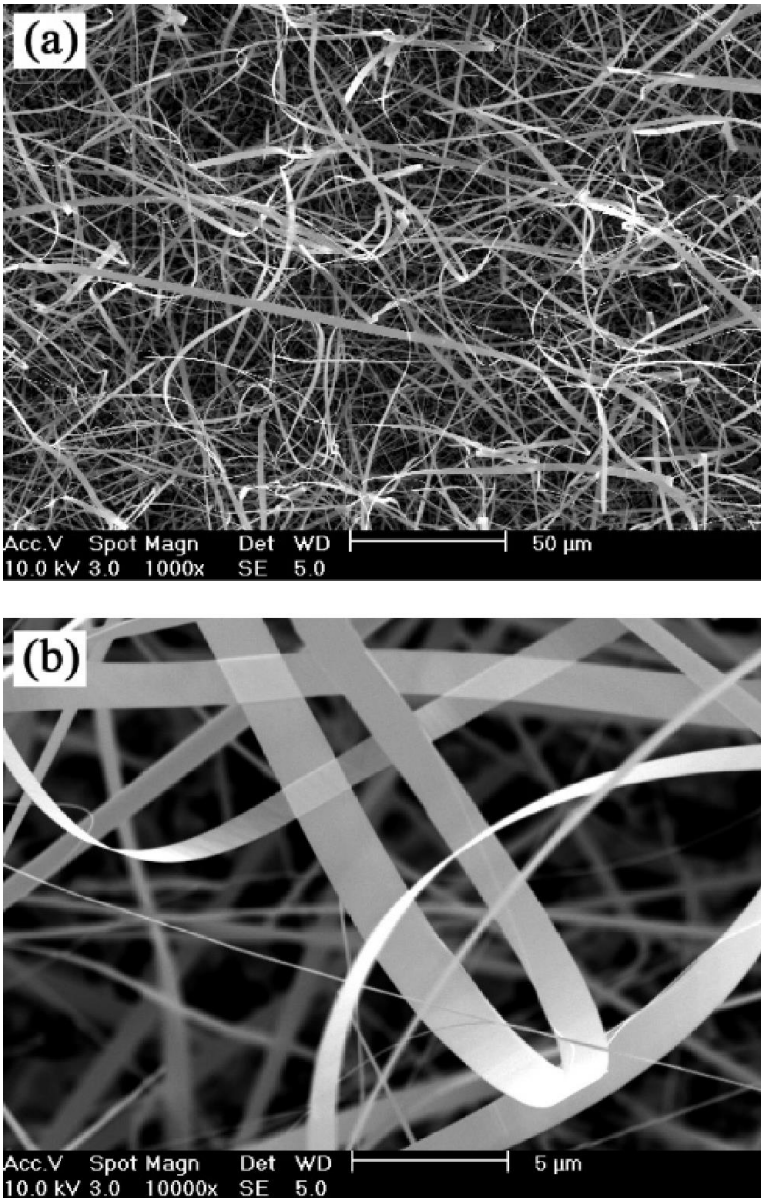

Figure 18. FE-SEM images showing the typical morphologies of the as-synthesised CdS nanostructures grown at different temperatures: (a) CdS nanowires and (b) CdS nanobelts. Reprinted from Ref. [248] with permission of ACS Publishers.

Electrochemical filling of pores using a solution of $CdCl_2$ and elemental sulphur in dimethyl sulphoxide [256] or thioacetamide in acidic aqueous solutions [257] at slightly elevated temperatures can lead to the formation of CdS nanowires. The products are single crystalline and their radial dimensions resemble the pore diameters of the template. Wetting the walls of AAO membranes via CVD of cadmium

bis(diethyldithiocarbamate) [261] and sol-gel methods using $CdCl_2$ and Na_2S in aqueous solution containing mecaptoethanol [262] allows the synthesis of polycrystalline CdS tubes as replica of the templates. Filling of the pores with similar wet techniques in several infiltration cycles is achieved using cadmium acetate and thioacetamide, which allows the slow release of H_2S and therefore better control over the reaction kinetics, preventing instant particle formation in the solution [259].

A reaction of thiosemicarbazide and Cd foil under solvothermal conditions in ethylenediamine [263] and the decomposition of $Cd(S_2CNEt_2)_2$ in refluxing ethylenediamine produces CdS nanowires at low temperatures [264]. SLS synthesis using cadmium bis(diethyldithiocarbamate) allows the formation of single crystalline CdS nanowires similar to the CVD experiments with the identical precursor as described above [83]. The growth seeds for the solution based synthesis are bismuth nanoparticles instead of gold in the vapour phase growth, due to the lower melting point of Bi.

3.6 Zinc oxide

Zinc oxide is the most studied material among metal oxides due to its broad application portfolio related to its semiconducting and piezoelectric properties. For instance, ZnO-based devices can be used in optoelectronics, sensors, transducers, actuators and lasers. In contrary to group IV and III/V semiconductors CVD techniques using metal alkyls or hydrides are not the most popular techniques to grow 1D ZnO, however the synthesis of zinc oxide nanowires is described by the reaction of oxygen with dimethyl-zinc in presence of gold to promote VLS-type growth [269, 270]. The thermal evaporation of metallic zinc and subsequent oxidation to form zinc oxide

nanowires on various rough surfaces has allowed the aligned growth of wires without the need for catalysts or ZnO seed layers [271]. Zinc acetylacetonate hydrate is another precursor used in the catalyst-free CVD of ZnO nanowires in an oxygen containing atmosphere, which can lead to dendritic structures if the same substrate is used in two similar growth cycles [272]. Moreover, the pulsed laser ablation of ZnO targets and growth on Au containing surfaces [274] and on bare substrates [275] (figure 19) permits the formation of nanowire assemblies. Silver seeded zinc oxide NWs are described by Heo *et al.* via MBE, where the formation of wires merely occurs on the Ag containing areas [276]. Z. L. Wang's group discovered that thermal evaporation in the absence of a metal growth seed allowed the formation of very interesting 1D structures such as nanobelts [277], rings [281] and nanosprings as shown in figure 8 [282, 283]. The origin of the nanorings was attributed to the polar site-facets of the forming nanobelts, whereas the nanosprings showed a switch from belt-structure to a superlattices resulting in the curling of the nanostructure. Carbothermal reactions, by mixing the ZnO source with carbon, are also suitable for growing nanowires on gold [285, 286] or nickel [287] coated substrates, whereas the condensation on porous aluminium oxide can result in the formation of metallic zinc under appropriate conditions, which acts as a seed for ZnO nanowire nucleation [288].

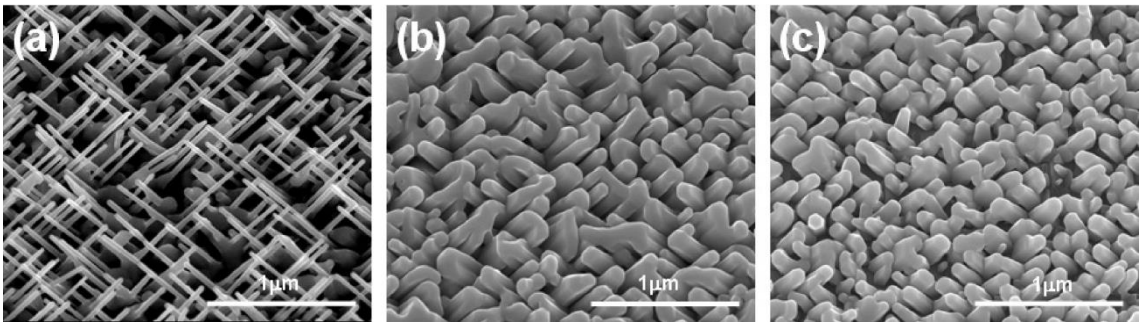

Figure 19. Tilted view (30°) SEM images of ZnO nanowire samples grown with an oxygen flow of (a) 0 sccm, (b) 20 sccm and (c) 35 sccm on m-plane sapphire via PLD of ZnO targets. Reprinted from Ref. [275] with permission of IOP.

Electrochemical deposition from an aqueous zinc nitrate solution into an AAO membrane has been reported to produce single crystalline zinc oxide nanorods [88], whereas deposition from zinc sulfate and boron acid produced metallic zinc wires. The metallic nanostructures could be oxidised in a second step to obtain ZnO nanowires [296]. Thermal decomposition of zinc acetate at elevated temperatures in trioctylamine [297] leads to ZnO nanowire formation. Large areas of small, oriented 1D ZnO nanostructures on various substrates are produced by the thermal decomposition of metheneamine in the presence of low concentrations of zinc nitrate in H_2O [298, 299]. Poly (vinyl alcohol) and zinc acetate solutions are appropriate precursors for the formation of polycrystalline ZnO fibres by electrospinning and subsequent calcination and pyrolysis of the organic polymer [302-305].

3.7 Tin Oxide

Tin (IV) oxide is an intrinsic n-type wide-bandgap semiconductor due to intrinsic oxygen vacancies. Its applications include gas sensing, heating elements and solar cells. Alkoxide-based gold-catalyzed CVD growth is a viable strategy to obtain well controlled SnO_2 NW formation [306, 307]. Diameter and orientation control of the

grown wires are achieved by appropriate growth parameter and substrate variation (figure 20). The formation of 1D SnO_2 nanowires via oxidation of tin vapours in oxygen containing atmospheres has been demonstrated on bare [308] and gold coated [309] substrates at temperatures between 900-950 °C. In addition, the VS synthesis of kinked tin oxide wires by SnO evaporation under pulsed flow conditions has been demonstrated [310]. The individual segments are formed due to unstable gas-phase supersaturation conditions in proximity to the substrate during growth. At low oxygen partial pressures the orthorhombic form instead of the common rutile crystal structure SnO_2 could be observed in nanowires [311] and nanobelts [312].

1D SnO_2 nanostructure synthesis includes the carrier gas flow supported thermal evaporation of SnO or SnO_2 powders, which leads to nanobelts in high quantity [313]. The laser ablation of pure tin in an oxidising Ar/O_2 atmosphere allows the formation of tin oxide nanowires [317], whereas the PLD process with a SnO_2 target at low pressures leads to single crystalline nanobelts [318]. Moreover, single crystalline SnO_2 nanowires can be obtained by a self-catalysed growth mechanism via carbothermal synthesis [321]. Screening several metal sources revealed the tin oxide nanowire formation via carbothermal synthesis using Pd, Ag, Al, Cr, Fe, Co, Ni, Cu and Au seeds [322]. However the autocatalytic growth of SnO_2 in gas phase processes should always be considered due to the thermodynamic stability of SnO at higher temperatures, and its tendency to disproportionate into Sn and SnO_2 on the substrates. Electrodeposition of tin wires within structure directing AAO membranes and post-oxidation is another approach to synthesise tin oxide nanowires [326, 327]. Polycrystalline SnO_2 nanowires can be prepared by electrospinning of mixtures of polymer solutions (poly(ethylene oxide) or poly(vinyl alcohol)) and tin sources, such as tin oxide sol [328],

dimethyldineodecanoate tin [329] or stannic chloride pentahydrate [330]. Pure, polycrystalline tin oxide fibres can be liberated from the carbon backbone and converted to crystalline SnO_2 by calcination in oxygen containing environments.

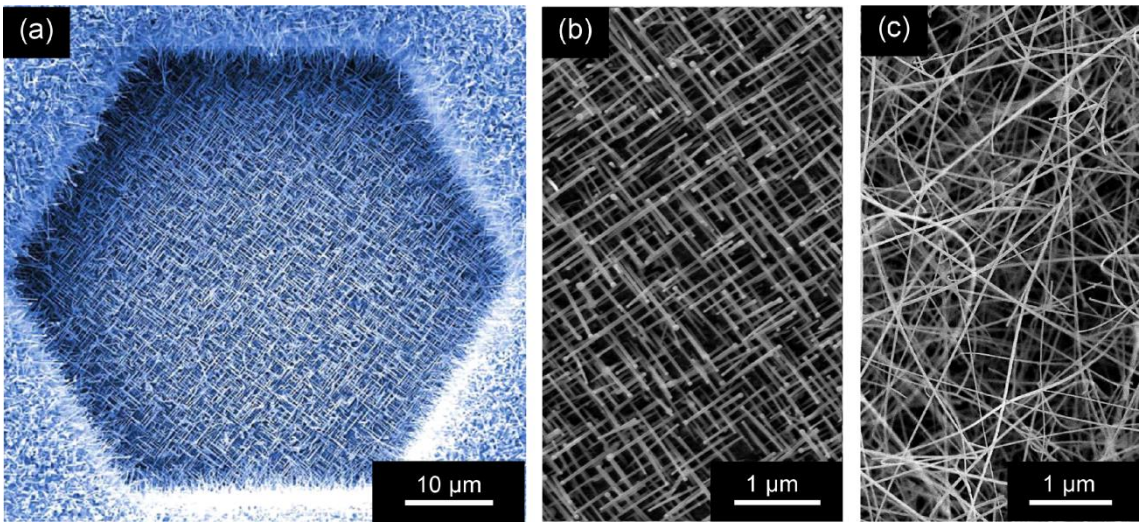

Figure 20. (a) SEM image of a combined view of oriented and random SnO_2 nanowire growth with enlarged images of Au promoted alkoxide-based SnO_2 nanowire growth, (b) aligned SnO_2 nanowires grown on TiO_2 (001) and (c) random wires on copper surfaces.

3.8 Semiconductor Heterostructures

The growth of complex nanostructures is the next step in the development of smart functional materials with well controlled interfaces. Heterostructures of material classes such as metals, semiconductors and polymers have led to unique properties and functionalities that are not realised in single-component materials. In this subsection we will focus on strategies to grow and control complex materials with nanoscaled heterostructures (figure 21). The synthesis is similar to single component materials but typically includes multiple steps to build the desired structure and tailor their properties. A recent review by Mieszawska *et al.* is devoted to these heterostructures and highlights a broad range of different material combinations [333].

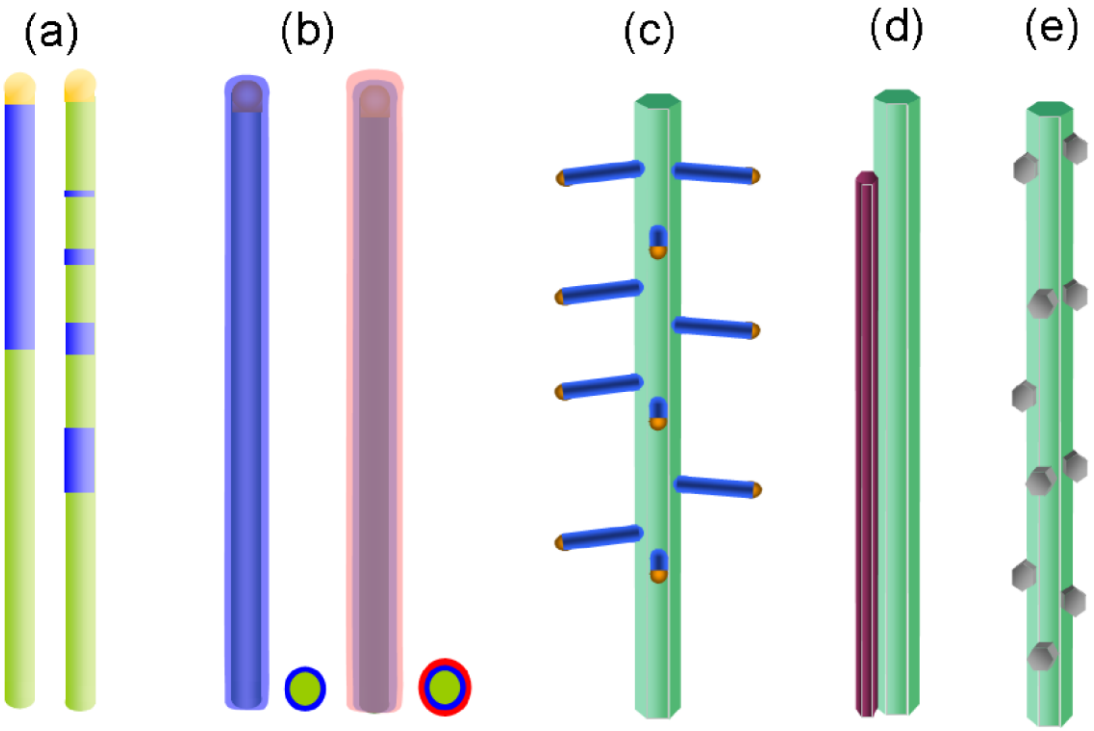

Figure 21. 1D heterostructures can be divided in following categories: (a) axial or segmented, (b) radial or coaxial, (c) hierarchical/branched (d) aligned and (e) 1D-0D heterostructures.

3.8.1 Axial Heterostructures

The synthesis of multi-segmented elemental semiconductor heterostructures have been described by several groups using metal seed promoted vapour phase growth techniques. For instance, MBE techniques allow the synthesis of Si/Ge segmented nanowires, by alternating the Si and Ge source evaporation cycles during deposition [334]. An approach to obtain Si/SiGe superlattices has been based on the continuous deposition of Si via silicon chloride decomposition and sequential laser ablation of a Ge target [335]. The physical evaporation by the laser results in the silicon-germanium intermixing within the catalyst particle and the formation of superlattice-like nanowires with an alternating Ge concentration. Similarly, the Au promoted growth of Si/$Si_{1-x}Ge_x$ heterostructures by CVD using silane and germane sources is demonstrated and shows

leading and trailing edges of the $Si_{1-x}Ge_x$ segments being parabolic, which is a probably a strain induced effect [54]. Sharper interfaces between Si and Ge segments can be achieved by AAO templated RIE etching doming pits on a MBE grown Si/Ge superlattice film [336]. Silver deposition and subsequent wet etching in HF/H_2O_2 results in highly crystalline Si/Ge NWs with diameters lower than 20 nm.

CVD techniques generally offer the best control over formation of III/V semiconductor nanowires, which also enables the growth of segmented wires by switching the gas phase supply of either the group III or group V source. An abrupt change in the segment composition of an InAs/InP wire is obtained via a procedure where growth is interrupted by stopping the group III source, such as trimethylindium, gas flow and changing the group V source [337]. Since crystallographic growth of the nanowires follows the arrangement of the substrate atoms as described in section 4, the nanowires were predicted to grow either in the <111> or <001> direction, with hexagonal or square cross sections depending on the substrate material. However the abruptness of the segment composition is dependent on synthesis and material combination and can also be in the range of 15-20 nm as described for GaP/GaAs superlattices [338].

Solution based synthesis of axial CdSe-CdS heterostructures can be realised by a sequential injection procedure of S/trioctylphosphine or Se/tributylphosphine in a Cd n-tetradecylphosphonic acid complex containing a tri-*n*-octylphosphine oxide solution with immobilised Bi seeds and removal of the residual reactants between two cycles [339]. Moreover, solid state reactions (temperature driven diffusion) can be used for the formation of NiSi/Si axial heterostructures via site selective physical vapour deposition of Ni onto Si nanowires through masking techniques and subsequent annealing (figure

22) [340]. The interface between the segments is atomically sharp and the technique opens up the possibility of integrating both active devices and high-performance interconnects from a single nanoscale building block. Nanometre scale chemical manipulation underneath an AFM tip is shown by electrochemical dip-pen nanolithography via site selective conversion of GaN nanowires into Ga_2O_3, resulting in alternating nitride-oxide segments [341].

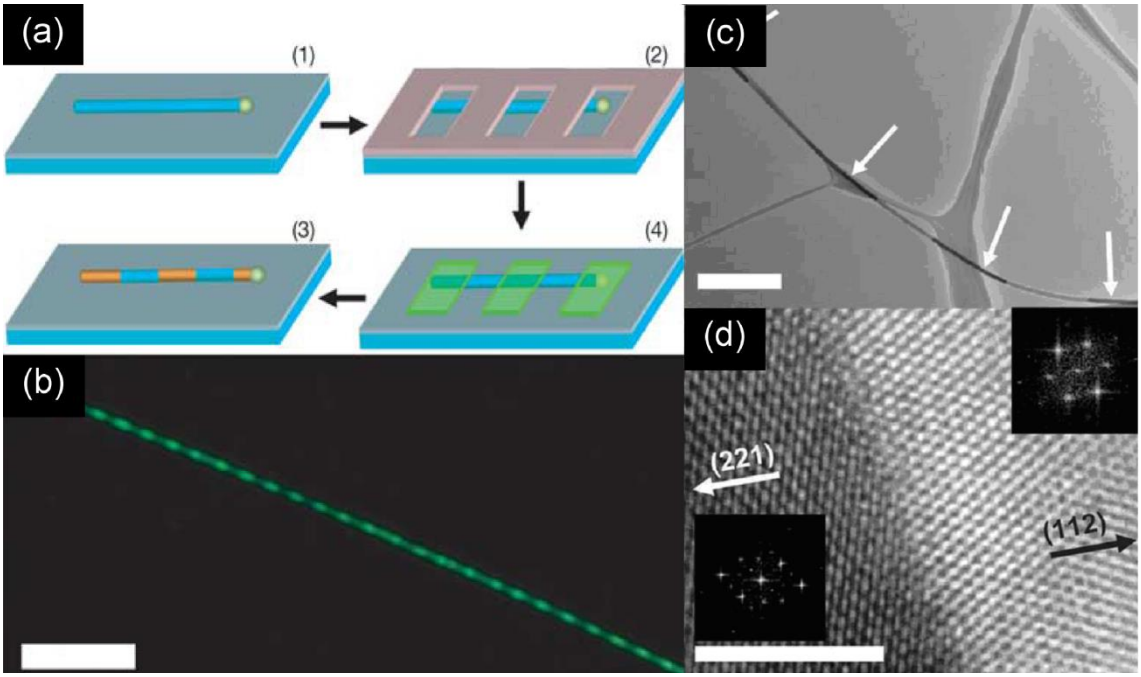

Figure 22. Fabrication and structural characterisation of NiSi/Si nanowire heterostructures and superlattices. (a) Fabrication of NiSi/Si nanowire heterostructures and superlattices: (1) Si nanowires (blue) dispersed on a substrate are (2) coated with photoresist (grey) and lithographically patterned, (3) selectively coated with Ni metal (green) to a total thickness comparable to the Si nanowire diameter and (4) reacted at 550 °C to form NiSi nanowires. (b), Dark-field optical image of a single NiSi/Si nanowire heterostructure. The bright green segments correspond to silicon and the dark segments to NiSi. Scale bar is 10 μm. (c) TEM image of a NiSi/Si heterostructured nanowire. The bright segments of the nanowire correspond to silicon and the dark segments, which are highlighted with arrows, correspond to NiSi. Scale bar is 1 μm. (d) High-resolution TEM image of the junction between NiSi and Si showing an atomically abrupt interface. Insets, two-dimensional Fourier transforms of the image depicting the [110] and [111] zone axes of NiSi and Si, respectively, where the arrows highlight the growth fronts of the NiSi (221) and Si (112). Scale bar is 5 nm. Reprinted by permission from Macmillan Publishers Ltd: Nature [340], copyright (2004).

3.8.2 Radial Heterostructures

Coaxial or core-shell heterostructures (nanocables) are typically formed in two step or multistep procedures where either the growth parameters or the synthetic method are changed. Due to layer growth onto a surface without the impact of a growth seed, the interfaces can be grown with high purity and control over thickness of individual layers. Intrinsic silicon (i-Si) core and p-type Si shell (p-Si) have been fabricated by altering the axial and radial growth modes during CVD [342]. After VLS-like growth of the intrinsic Si core, a shell is formed with diborane added as a p-type dopant by lowering the synthesis temperature. The same procedure is used to fabricate Ge/Si core/shell nanowires using germane and silane sources [343]. The amorphous shell could be crystallised by thermal annealing in both cases, which resulted in epitaxial coaxial structures. Several III/V combinations are shown to be viable components for functional devices and one of the most advanced examples of a core-multishell GaN/InGaN/GaN/AlGaN structure is described by Quian *et al.* [344]. The growth rate of the shell material was dependent on the surface facets and lead to non-uniform shell thicknesses around a trigonal GaN core. Two equivalent crystal facets ({1-101} which are Ga faced surfaces) have exhibited faster growth rates than the {0001} facet, which is an N-polarity face. Qian *et al.* reported the highly controlled formation of up to 26 (InGaN/GaN) quantum well structures at the {1-101} facets onto a GaN core with the thicknesses of each quantum well in the range of 1-3 nm [345]. MBE is also a viable tool for shell formation, which can be used to form homogeneous shell thicknesses for wires grown perpendicular to the surface and also to grow thicker shells on surfaces facing the source for tilted wires [346]. In addition, the non-epitaxial growth of coaxial structures such as Si/CdSSe is described by the thermal evaporation of three individual

sources, where the composition of the shell is dependent on the effective mass ratio of the CdSe and CdS sources [347]. The core was grown via Au promoted Si nanowire formation and acts as the template for the coaxial growth of the tuneable CdSSe shell. Several additional systems are described in relevant literature using various growth techniques. The essential part of vertical field effect transistors as shown in figure 23 could be seen as core-shell structures with a wrap around dielectric as shell material, such as described for thermally oxidized Si NWs to obtain Si/SiO_2 cables as core and dielectric [348], however this kind of electrical components will not described in detail.

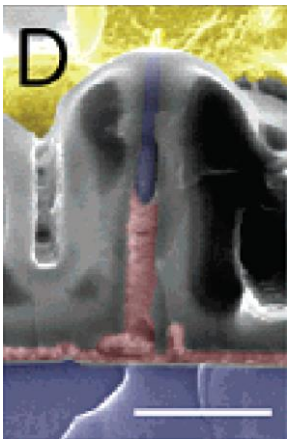

Figure 23. Cross-sectional SEM image of a VINFET device. Scale bar is 500 nm. False colour is added to the image for clarity. Blue corresponds to the Si source and nanowire, gray corresponds to SiO_2 dielectric, red corresponds to the gate material, and yellow corresponds to the drain metal. Reprinted from Ref. [348] with permission of ACS Publishers.

3.8.3 Hierarchical Heterostructures

The complexity of heterostructures can be increased by the growth of hierarchical or branched structures. Their morphology is described by terms, such as nanotrees, nanobrushes etc. Obviously, for controlled branching events a crystallographic relation should be present to guide the subsequently grown branches. Controlled branching

events have been demonstrated for GaP/GaAsP hierarchical structures, which were formed in a two stage VLS mode MOVPE growth process [349]. The GaP trunks were seeded by relatively large Au particles and grown on oriented gallium phosphide substrates. Thereafter, additional growth seeds were deposited onto these host structures, followed by the MOVPE growth of the branches. Non-epitaxial hierarchical ZnO branches can be grown on several 1D backbone materials, such as SiC, GaP, GaP and carbon nanotubes by In and Ga induced seeding of ZnO, which is formed by oxidation of the metallic Zn vapour source [350]. However, for metal oxide semiconductors merely a few such heterostructures are described in the literature. Most of these features are synthesised by vapour phase techniques and include combinations such as In_2O_3/Ga_2O_3 [351] and SnO_2/V_2O_5 [306]. Both of the described examples are grown via vapour phase routes, while In_2O_3/Ga_2O_3 is grown in one step and the SnO_2/V_2O_5 in a two step process, which includes a VLS-like growth of the initial trunk formation.

4. Alignment of 1D nanostructures

4.1 In-situ alignment of 1D Nanostructures

Most *in-situ* alignment techniques are based on either templates, etching or epitaxial metal-promoted growth techniques. The template based technique is already described in section 2.5 in detail. However hybrid approaches, such as the homo and hetero-epitaxial growth of Si nanowires, with unconventional growth directions, within AAO membranes on Si substrates has been described by Shimizu *et al.* [142, 352]. Etching techniques are a viable approach to produce horizontally or vertically aligned nanowire

assemblies, due to site-selective removal of material at the unprotected area (masking techniques) or metal-enhanced etching. The different techniques are already mentioned in section 2.7.

The most popular approach of *in-situ* alignment is the homo- or heteroepitaxial growth of single-crystalline 1D materials via metal promoted synthesis. Single crystalline substrates with appropriate lattice parameters are used to guide the growing crystals in specific directions, which is a key requirement for the successful integration of individual and arrays of 1D nanostructures into functional devices. The site-selective deposition of metal growth seeds is demonstrated by several techniques, including physical vapor deposition through masks which are fabricated with e-beam lithography [353], nanosphere lithography [290], and shadow masking using membranes. Moreover, liquid-based methodologies such as the capturing of individual colloidal metal particles on polymer inked surfaces by microcontact printing [354] or deposition of well spaced single particle lines from a dilute Langmuir-Blodgett particle monolayer via a stick-slip technique [355] are suitable to achieve site-selective metal deposition for nanowire growth. Moreover, a cost effective and large area metal deposition procedure is based on nanoimprint lithography using appropriate stamps for pattern transfer [356]. In addition to the directional alignment of wires on flat surfaces, nanowire interconnects can be defined by catalyst particle deposition on the sidewalls of single crystal Si microtrenches and subsequent nanowire growth as shown for homoepitaxial growth of Si nanowires (figure 24) [357, 358] and heteroepitaxial growth of InP [359]. He et al. demonstrated that the spacing, catalyst density and catalyst size control the length, number and diameter of the bridging nanowires, respectively [357].

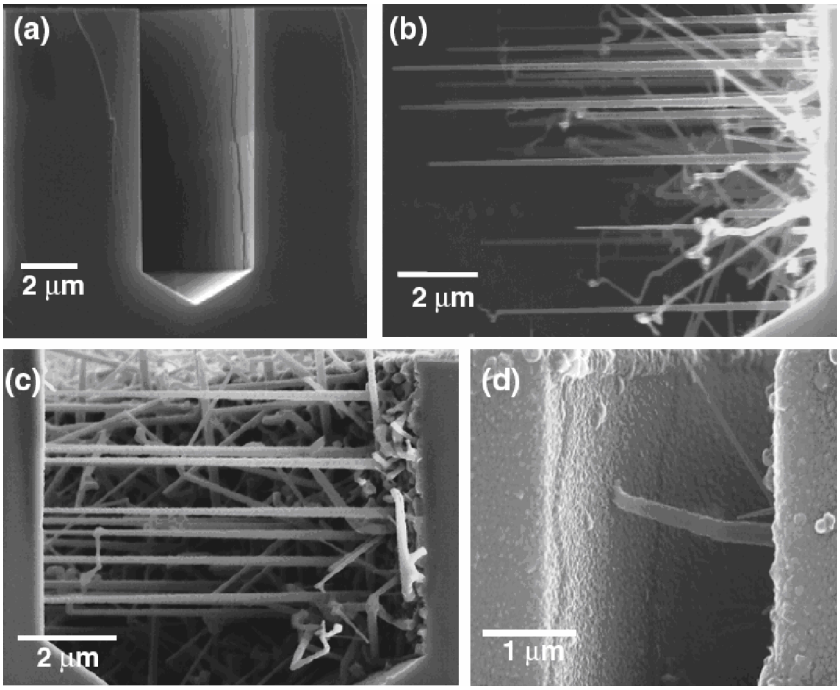

Figure 24. Cross-section scanning electron micrographs (SEMs) of (a) a 4 μm-wide, anisotropically etched trench in a Si(110) wafer; (b) Au-catalyzed, lateral epitaxial nanowire growth from a (111) sidewall surface into a 15 μm-wide trench; (c) Au-catalyzed, lateral epitaxial nanowire growth across an 8 μm-wide trench, connecting to opposing sidewall. (d) Ti-catalyzed lateral growth of a Si nanowire to form a bridge across a 2.5 μm-wide trench. The direction of nanowire growth is from the right to the left in (b)–(d). Reprinted from Ref. [358] with permission of IOP.

4.2. Post growth alignment techniques

Several methods have been described to successfully align 1D inorganic nanomaterials. An elegant way via a 'blown bubble film' technique, using a polymer-nanowire solution with appropriate viscosity, was demonstrated by Yu GH *et al.* [360]. The method involves expanding a bubble from a homogeneous suspension of stable epoxy solutions containing surface modified nanomaterials. The nanowires align during the bubble expansion and can be transferred to both rigid and flexible substrates. Si nanowire FETs produced from bubble-blown nanowire assemblies show reproducible device properties, which is necessary for large area electronics. The main advantage of using the bubble blow technique to align nanowires is that large substrates (up to

225x300 mm) can be decorated with aligned nanowires without the need of lithographic techniques. However, at present the bubble blown technique is lacking in control over the areal density of wires on the substrate.

In the Langmuir–Blodgett (LB) method, surfactant coated 1D nanostructures are slowly compressed onto an aqueous subphase to yield uniaxially-aligned assemblies [361]. The LB technique permits the arrangement of parallel nanostructures with controlled spacing, and can be used to assemble more complex structures by multiple layer transfer steps [362]. Functional devices based on such LB films consisting of nanowires have been fabricated [363] although upscaling to larger areas with high efficiency and transfer to non-rigid surfaces are not described

Dielectrophoresis (DE) has been used to assemble of nanowires from solution on substrates without the need for surface modification. The electrokinetic motion of dielectrically polarised materials in non-uniform electric fields can be used for the self alignment of nanowires. In this respect, an external field is induced between metal micoelectrodes by applying an AC voltage, resulting in a well defined space-charge region. This non-mechanical manipulation technique allows the assembly of different quantities of 1D structures, depending on the concentration of the nanostructures in the solvent, the magnitude and frequency of the applied field and the gap distance between the electrodes [364]. The alignment process can be optimised for single nanostructure bridging devices leading to reliable single nanonostructure diodes [365] and multi-wire FETs [366]. Appropriate bus bar spacing as well as very high frequencies allow almost exclusive alignment of single nanostructures between electrodes [367]. Medium frequencies attract the most wires, however they partially adhere to the buses or the aligned wires are accompanied by additional wires as illustrated by the histogram in

figure 25. Finite element simulation also helps to understand the role and improve the electrode geometry, such as the bus design for large area integration and reduced attraction of unaligned wires.

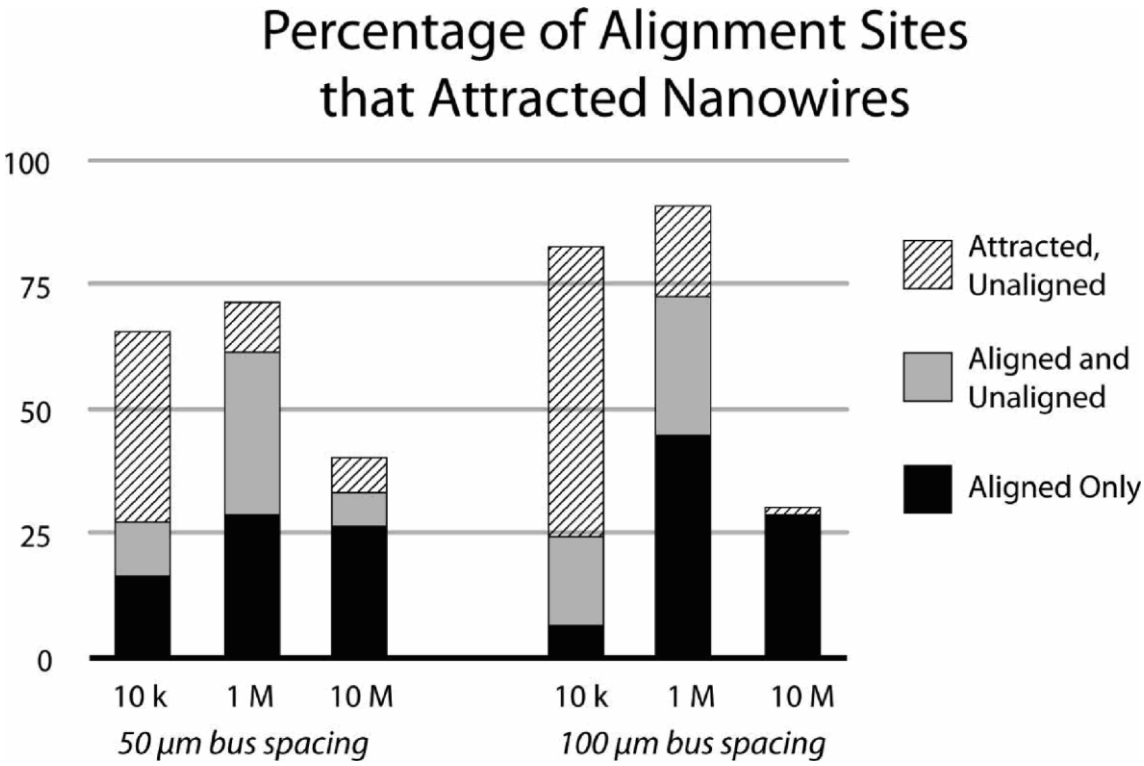

Figure 25. The histogram shows the percentage of alignment sites that attracted nanowires and the quality of alignment. Each bar is divided to show the percentage of sites that attracted and perfectly aligned a nanowire (black), sites that attracted and perfectly aligned a nanowire while others remained unaligned at the same site (gray), and sites that attracted but did not align nanowires (lines). Reprinted from Ref. [367] with permission of ACS Publishers.

Another viable approach uses the sheer-force, which is induced by sliding a nanowire-containing substrate against a second substrate, to orientate nanowires [368]. The as-grown non-oriented nanowires are well aligned due to the sliding process, which is a direct dry transfer of nanowires to the desired surface. Prior patterning of the device surface allows a side selective transfer and prevents the deposition of low quality wires as well as particular deposits close to the growth substrate surface. The wires deposited by this method are also used to build high performance 3D nanoelectronics, such as

FET's [368]. The use of a lubricant, differently modified surfaces as well as patterned substrates allow the alignment of a variable density of wires, due to significally minimised nanowire-nanowire mechanical interactions and enhanced nanowire-surface chemical binding interactions [369]. The methodology allows the deposition of nanowires on flexible and ridged surfaces and the controlled bonding of individual and arrays of aligned wires.

5. Applications

5.1 Nanowire sensors

The fundamental background of sensing is based on changes in the proximity of the active material, which leads to changes in the electrical or optical properties. In most cases the interaction between adsorbed (physi- or chemisorbed) species is responsible for these effects. The effective change of the local charge density can be detected by variations in the conductivity of the devices used to detect the species of interest. In the molecule-surface interaction the term ionosorption is used when an adsorbate captures an electron or a hole on the surface via chemisorption. Differences in tendency of physi- or chemisorptions are dependent on environmental conditions for energy transfer, due to the energy activated binding and desorption for chemisorbed species on surfaces. These energies can be either provided thermally or by illumination. For effective sensing the activation energy for the desorbtion of species has to be overcome, however the optimal operation conditions (temperature or photon energy and flux) have to be evaluated to ensure reversible chemisorption. This already implies that sensing is an equilibrium status, which changes with experimental conditions. The advantages of 1D nanostructures in comparison to 2D assemblies of particles (thick and thin films) is the

higher stability of 1D nanostructures due to their high crystallinity, their large surface-to-volume ratio, the potential to modify/functionalise the surface of the 1D objects with target-specific receptors or catalysts, the reduced impact of grain boundaries and the potential to tune the sensitivity and selectivity by gating in FET configuration. Similar to the impact of crystallite sizes in particle-based sensors [370, 371], the radial dimensions of the wires play an important role in the sensitivity of sensing devices due to increased surface states and higher impact of surface binding events on the electrical signal used for detection.

Nanowire-based chemical sensors are usually fabricated in two configurations, resistors and FET devices with single or multiple nanowires. Most literature reports in this field are based on these two configurations due to fairly simple fabrication, high reliability, low cost, and easy integration with heat transducers.

5.1.1 Bio-sensors

One-dimensional semiconductor nanowires for biosensing are usually used in FET devices. Silicon is one of the best characterised semiconductor nanowires and can be prepared as a p- or n-type material. In addition, the reliable electrical performance of silicon nanowire-based FETs is demonstrated, however comparing electrical data it has to be considered that the doping level of the nanowires and related contact resistances have a large impact on the electrical behaviour of the device [372, 373]. Attention must be paid to the buffer solution (pH and ionic strength) in which measurements are performed, because FETs respond to changes in surface charge. The detection of specific molecules at the surface of nanowires is generally enabled by linking nanowire receptor groups that recognise specific molecules to the surface of the 1D structure. In this respect, the surface is modified with organic molecules, which are covalently

bonded to the wire via the silicon oxide interface. Pre-treatments in a water atmosphere can be performed in order to increase the number of hydroxyl groups on the surface, which are necessary for the silanisation with specific organosilanes carrying functionalities for the attachment of the active biomolecule [374, 375]. When the sensor device with surface receptors is exposed to a solution containing a macromolecule, that has a net negative (or positive) charge in aqueous solution, specific binding will lead to an increase (or decrease) in the surface negative charge and an increase (or decrease) in conductance for a p-type nanowire device. The first example of electrical detection of proteins in solution with nanostructures was reported for p-Si nanowire devices by the Lieber group in 2001 [376]. Biotin, which binds with high selectivity to streptavidin, was linked to the oxide surface of the nanowires and used as a receptor. After injection of streptavidin containing solutions, the conductance increased to a stable value due to the surface charge of streptavidin and the retained signal after switching to pure buffer solution was attributed to the low dissociation tendency/rate of the streptavidin–biotin complex.

Binding of the biological molecules by the non-covalent immobilisation of peptide nucleic acid is successfully demonstrated to achieve reliable detection of DNA sequences versus mismatched DNA in the tens of femtomolar concentration [377]. This strategy circumvents the modification of the semiconductor surface during the silanisation process, which typically is based on a high amount of OH groups on the surface to bind the silanes. Another report describes the detection of up to 25 pM complementary single stranded DNA by covalently immobilised single strand DNA [374]. Highly sensitive and selective real-time and multiplexed detection of different protein cancer markers with good signal-to-noise ratios down to a 50- to 100-fg/mL

level is demonstrated for different monoclonal antibody modified Si nanowire arrays [378]. Moreover, high selectivity and sensitivity is achieved showing highly reproducible responses for concentrations of as low as 0.9 pg/ml in undiluted donkey serum samples. The detection of three different cancer marker proteins by different surface modified silicon nanowires is shown in figure 26.

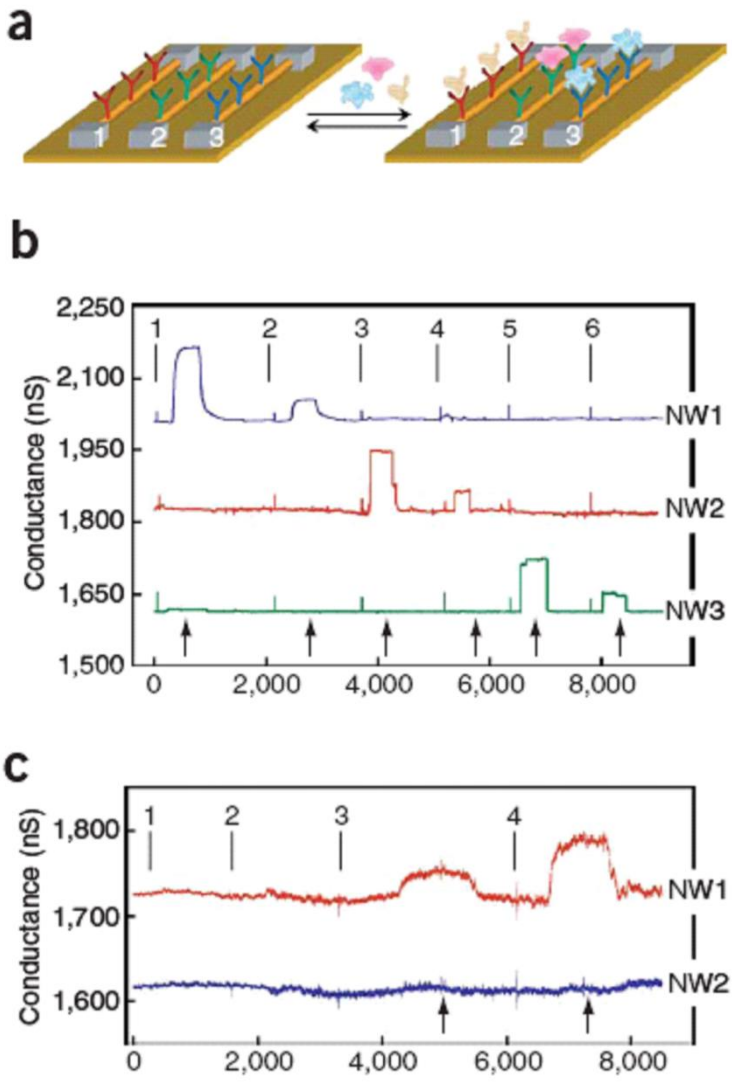

Figure 26. Multiplexed detection of cancer marker proteins with an array of Si nanowires, which are individually differentiated with distinct receptors as schematically shown in (a). (b) Conductance-versus-time data recorded for the simultaneous detection of prostate specific antigen (PSA), carcinoembryonic antigen (CEA) and mucin-1. The solutions were delivered to the nanowire array sequentially as follows: (1) 0.9 ng/ml PSA, (2) 1.4 pg/ml PSA, (3) 0.2 ng/ml CEA, (4) 2 pg/ml CEA, (5) 0.5 ng/ml mucin-1, (6) 5 pg/ml mucin-1. Buffer solutions were injected following each protein solution at

points indicated by black arrows. (c) Conductance-versus-time data recorded for the detection of PSA-containing donkey serum samples on a p-type Si nanowire array in which NW1 was functionalised with antibody 1 and NW2 was passivated with ethanolamine. The solutions were delivered to the nanowire array sequentially as follows: (1) 1 μM phosphate buffer + 2 μM KCL, pH = 7.4, (2) donkey serum, (3) a mixture of donkey serum and 90 pg/ml of PSA, (4) a mixture of donkey serum and 0.9 ng/ml of PSA. The donkey serum was injected at points indicated by the black arrows. Reprinted by permission from Macmillan Publishers Ltd: Nature Biotechnology [378], copyright (2005).

Nanowire FETs are also described to be able to detect single viruses with high selectivity, when the Si surface is functionalised with antibodies specific to the detectable virus species [379]. Similar to parallel detection of cancer markers, it is also shown that multiple viruses can be recognised and the electrical responses of the antibody containing devices recorded to determine the presence of various species. The detection of the binding and unbinding of an individual entity is also confirmed by simultaneous optical measurements of a fluorescently labelled virus showing a correspondence between the electrical signal recorded and the presence of the targeted species. The nanowires in the examples described above are synthesised via bottom up approach CVD methods which provide much greater flexibility in nanowire material properties and surface functionalisation, but does not yet offer the fabrication reliability of top-down approaches in terms of assembly onto a chip surface.

In top-down strategies, Stern *et al.* reported a complementary metal oxide semiconductor (CMOS) FET compatible technology to detect antibodies with 100 fM concentration [380]. The resulting Si nanowires had trapezoidal cross-sections with nm-scale width and height and the devices enabled the real-time detection of biomolecules. Figure 27 shows the scheme of the device used and the response of two differently functionalised wires to their respective antibody.

Recently, electrostatically adsorbed DNA probes on functionalised Si nanowires are used to demonstrate DNA detection in 165 mM salt despite the short Debye length at this ionic strength [381]. In addition, the authors show an enhanced sensitivity of an almost oxide free surface prior to functionalisation, which increases the detection limit by 2 orders of magnitude.

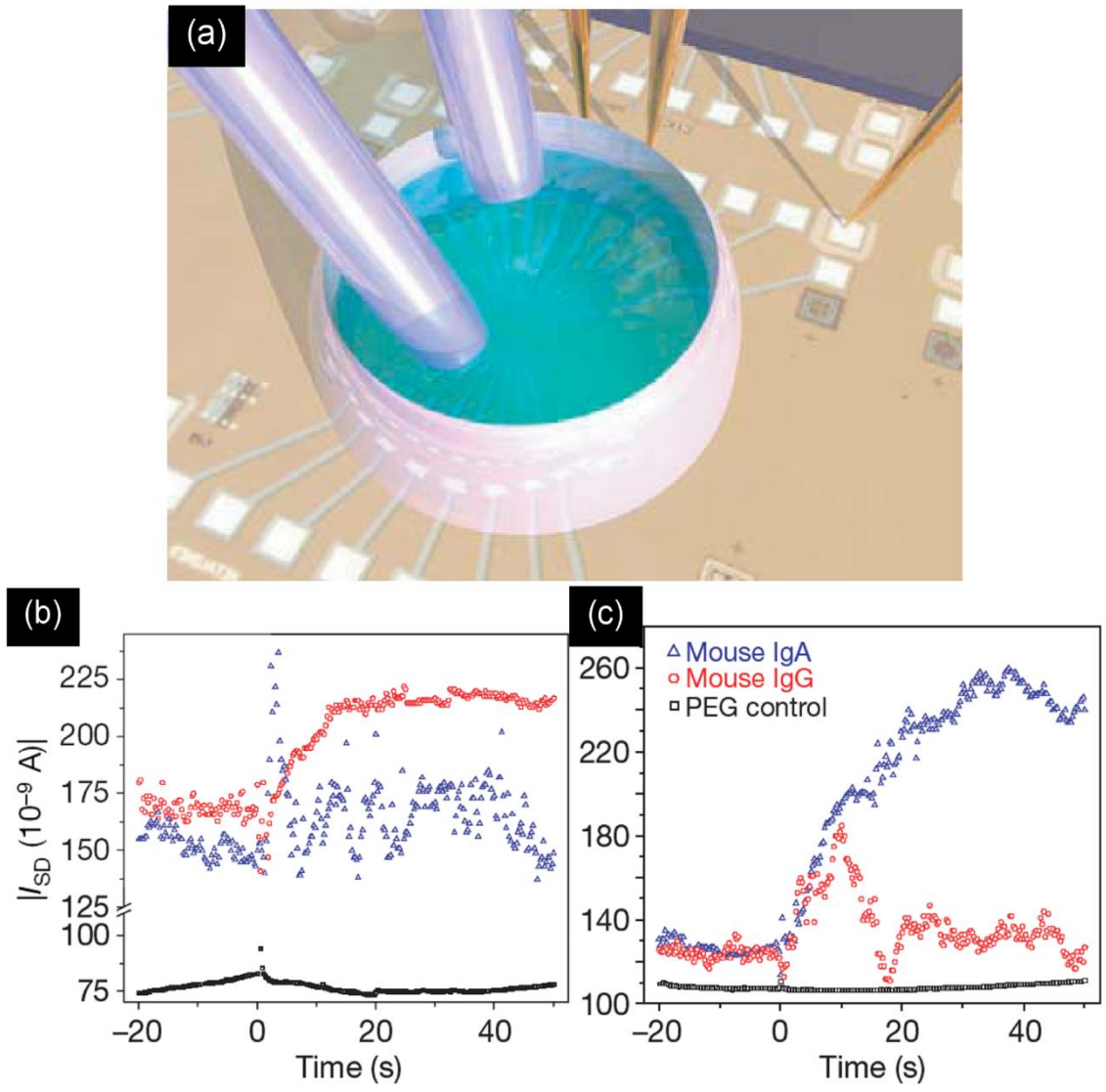

Figure 27. (a) Schematic of fluid exchange system superimposed on chip optical micrograph. Fluid supply and return are provided by Tygon tubes. Sensor responses to 100 fM mouse-IgG (red) or 100 fM mouse-IgA (blue) for goat anti-mouse IgG-functionalised sensor (b) or goat anti-mouse IgA-functionalised sensor (c). The PEG

functionalised sensor control is shown in black. Reprinted by permission from Macmillan Publishers Ltd: Nature [380], copyright (2007).

Top down techniques using thermal oxidation of Si nanowires and etching of the grown SiO_2 layer to tune the dimension of the nanowires, have been prepared from silicon-on-insulator wafers [382]. These devices show that PNA functionalised arrays of Si nanowires could detect complementary target DNA with high sensitivity (10 fM). However the readout signal, which is dependent on the distance of the DNA charge layer to the Si nanowire surface, has to be taken into account when determining the sensitivity of the field-effect based sensor, which is demonstrated in a systematic approach by Zhang *et al.* [383]. The field effect becomes much weaker when the charge layer is farther apart from the Si nanowire sensor surface, which is shown by PNA functionalsed Si nanowires. The evolution of signal strength by changes in the distance of the charge layer was illustrated by varying the hybridisation sites of DNA to the PNA capture probes while maintaining the total number of charges unchanged. The dependence on the distance of DNA strands to the Si nanowire surface demonstrates the significance of charge layer distance to ensure Si nanowire biosensing sensitivity. The graphical illustration of this effect is shown for two concentrations in figure 28.

In addition, the conductance level of Si nanowires reveals a clear and reproducible dependence on the flow velocity of the analyte. In addition, the conductance depends on the ionic strength and the composition of the electrolytic solution while the direction the conductance variation depends on the doping type of the Si nanowires [384]. The quantitative analysis of Si nanowire FETs suggests that flow velocity sensing is a consequence of the streaming potential generated by the movement of counter-ions inside the electrical double layer. The streaming potential, which varies with the flow

velocity, the ionic strength and the composition of the electrolytic solution, acts in the same way as charged analytes in affecting the conductance of Si nanowires. This demonstrates that in addition to the analyte binding events, the properties and the velocity of the electrolytic solution can significantly change the conductance of nanowire FET sensors and it is important to consider these factors when analysing and optimising the sensing. The results described in this subsection clearly indicate that nanowire-based devices could lead to multiplexed bioanalysis and are therefore beneficial for human health management.

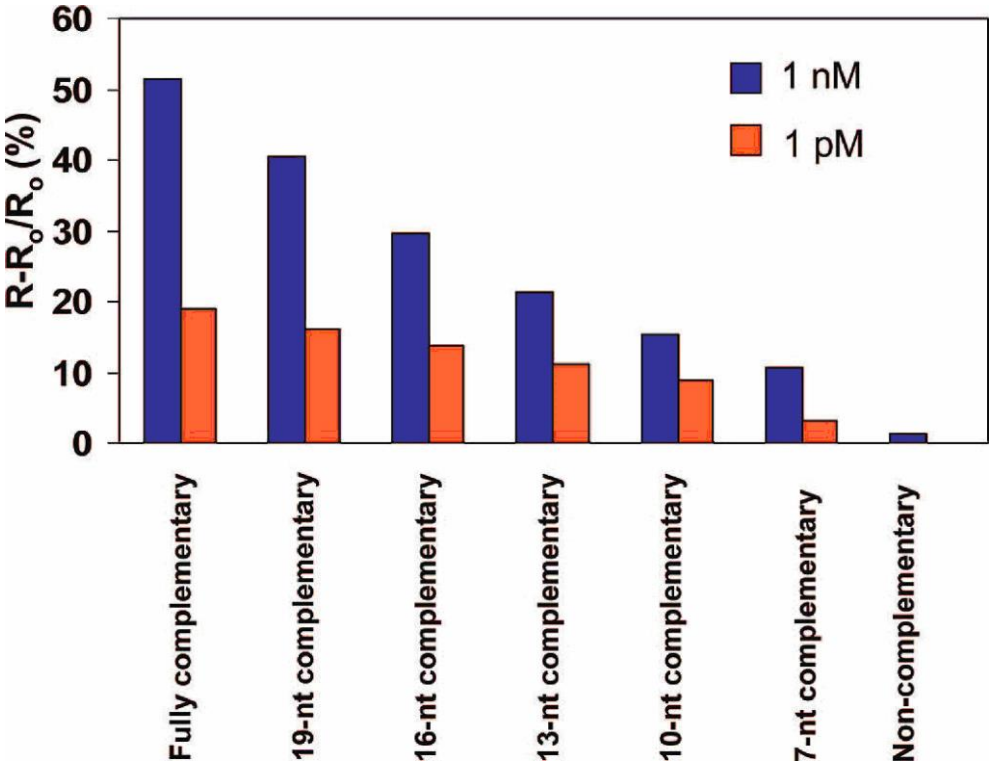

Figure 28. Distinguishable resistance change of the Si nanowire caused by varying hybridisation sites at two different concentrations of the target DNAs. Reprinted from Ref. [383] with permission of ACS Publishers.

5.1.2 Gas detection

Metal oxides are typically used for detecting changes in gaseous atmospheres, due to their ability to effectively ionosorb oxygen above 100 °C. The interaction between the

detectable species and oxygen are dependent on reactions or competition for the same adsorption sites with ionosorbed oxygen (molecular O_2^- or atomic O^-) [385]. The usual oxygen deficiency of metal oxides is responsible for the well known drift in the sensor baseline. The influence of oxygen diffusion in single wires during tin oxide sensor operation on nanowire-based devices with different diameter of the 1D nanostructure was described by Hernandez-Ramirez *et al.* [386]. In addition, the conductance of the oxide sensing material relates to the amount of adsorbed NO_2 molecules, which increase the resistance of the metal oxide due to electron capture on the surface by NO_2^- [387]. According to first-principles calculations [388], NO_2 molecules adsorb onto SnO_2 surface oxygen vacancies with typical desorption energies (E_{des}) ≥ 0.52 eV (T ≥ 80 ºC) [389]. Thus, at room temperature (T = 25 ºC) NO_2 desorption barely takes place and no recovery of the device baseline is observed. For this reason, metal oxide sensors are typically operated at temperatures above 150 ºC in order to guarantee a fast molecular desorption and full recovery of the initial sensor surface [384].

Reducing gases like CO increase the conductivity of metal oxides by releasing surface bound electrons, formerly captured by ionosorbed oxygen, in the conduction band due to oxidation to CO_2. However, the interaction of the metal oxide sensor surface with additional gaseous species such as water has to be taken into account due to the cross-sensitivity of metal oxides and therefore low selectivity [390, 391].

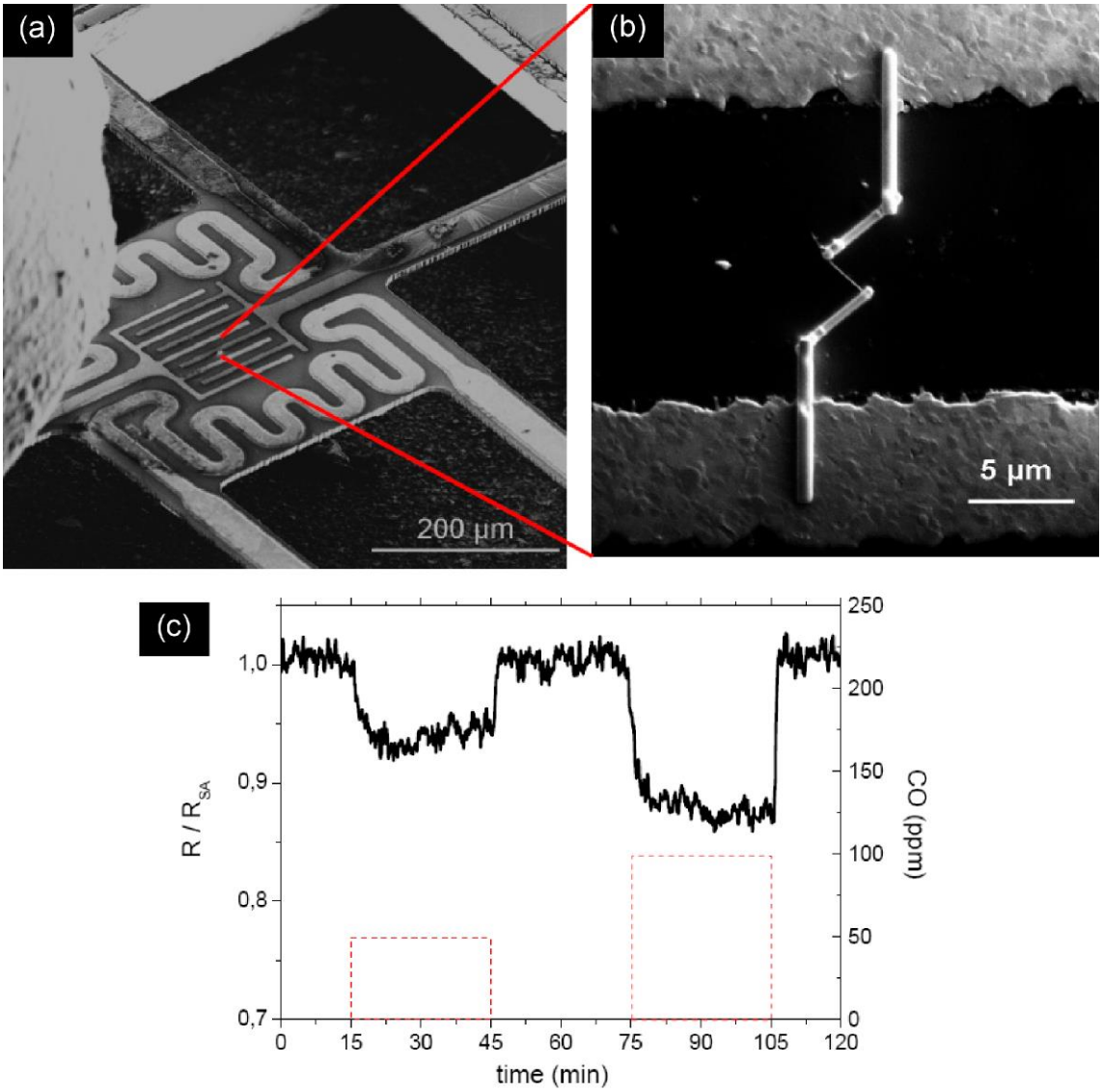

Figure 29. (a) SEM image of one suspended micromembrane with one integrated heater. The microneedle used during the nanolithography process to introduce the gas precursor inside the FIB chamber can be observed in the left part of the image. (b) A SnO_2 nanowire electrically contacted to the platinum microelectrodes. Dimensions: L = 2.1 µm (length) and R = 35 ± 5 nm (radius). (c) Response of one SnO_2 nanowire to different CO concentrations (50 and 100 ppm), when the membrane heater is switched on (P = 56 mW, T = 120 °C). The dashed line indicates the CO pulses. Reprinted from Ref. [397] with permission of IOP.

In the literature, there are several reports on thermally heated SnO_2 nanowire gas sensors spanning the use of multiwire [392] and individual nanostructure devices [393]. Polycrystalline individual wires have also been investigated for oxygen and CO sensing

[394]. However, the contribution from electrical contacts has to be taken into account for the determination of physical parameters [373, 395]. The properties of heterointerfaces in semiconducting nanowires were recently highlighted for several material systems by Agarwal [396]. Comini *et al.* report good sensor responses of tin oxide nanobelt meshes towards CO, NO_2 and ethanol [392]. A progression towards real devices is the fabrication of portable tin oxide single nanowire-based gas sensor devices on free standing membranes as shown in figure 29 [397]. The sensors are prepared using dual beam FIB techniques to contact individual wires to interdigital electrodes on the membrane and showed fast responses as well as comparable performance, when compared to bulk heating sources.

In addition, self heating (Joule heating) of tin oxide nanowires is demonstrated to be sufficient to ensure reliable sensor performance, which is comparable with the usage of conventional external heating sources [398, 399]. Surface modification and enhanced sensitivity of palladium nanoparticle decorated 1D tin oxide single crystals is shown by Kolmakov *et al.* to enhance oxygen dissociation on Pd (spillover effect) [400]. In order to target the well known problem of metal oxide cross sensitivity, SnO_2 nanowire-based electronic nose configurations are reported for a gradient gas sensor microarray, which enabled the detection of different gaseous species simultaneously (figure 30) [401]. The structural integrity of single-crystalline tin oxide nanowires during long term experiments results in stable responses of nanowire-mat devices in contrary to SnO_2 nanoparticle-based sensors [402]. The initially superior sensitivity of nanoparticle 3D network layers towards isopropyl alcohol dropped to the response level of nanowires within 46 days under changing atmospheres (dry nitrogen, humidity).

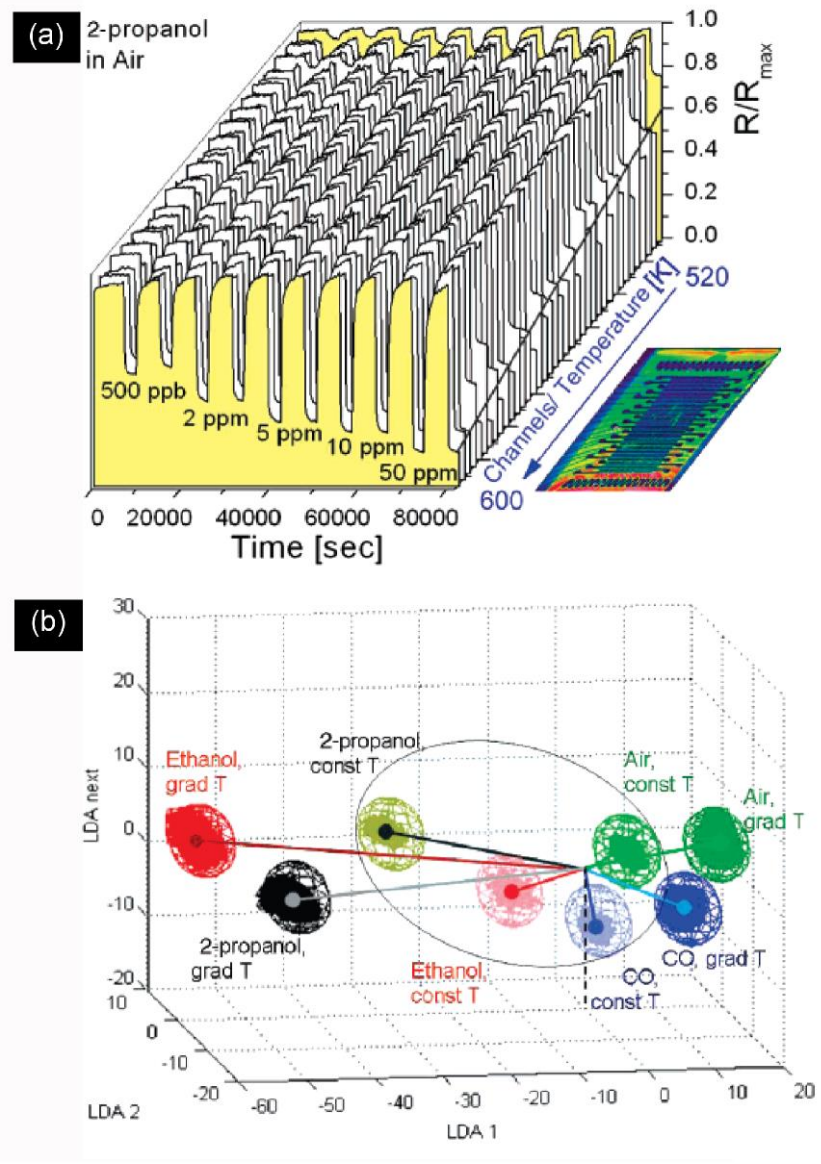

Figure 30. (a) Normalised resistance response of the 38 individual nanowire sensing elements toward 2-propanol pulses when 80 K thermal variation is established along the sensing array. The side line indicates the growth of responsiveness with the temperature. (b) LDA (linear discriminant analysis) of the conductivity patterns obtained with SnO_2 nanowire-based gradient microarray at exposure to the sample gases (2-10 ppm concentration range). The classification spheres correspond to normal distribution of data at 0.9999 confidence level. The microarray operates under (a) quasi-homogeneous heating at 580 K (const T areas inside the ellipse with dimmed colours) and (b) temperature gradient at 520-600 K (grad T areas with bright colours). Reprinted from Ref. [401] with permission of ACS Publishers.

ZnO nanowires with radial dimensions in the range of 25 nm were transferred to a membrane with interdigital platinum electrodes and a heater, in order to reduce the

power consumption during operation [403]. These devices showed high sensitivity to ethanol vapours in the range of a few ppm (S = 47 for 200 ppm ethanol), when operated at 300 °C. Nanorod containing paste sensors have been prepared by mixing an adhesion agent and hydrothermally grown ZnO nanorods [404]. The resulting paste was coated on an alumina tube containing electrical contacts. High sensitivities towards inflammable gases such as ethanol, gasoline and liquid petroleum gas as well as other gaseous species (H_2S, HCHO, CO and ammonia in the ppm range) were obtained. In addition to the mainly temperature driven gas sensors, Law *et al.* described the photochemical activated sensing of nitrogen dioxide using a room temperature operated SnO_2 nanobelt device [405]. The adsorption and desorption of gaseous species was promoted by UV activation of the metal oxide, which was triggered by the photon flux to achieve similar performance when compared to thermally heated devices as shown in figure 31 [406].

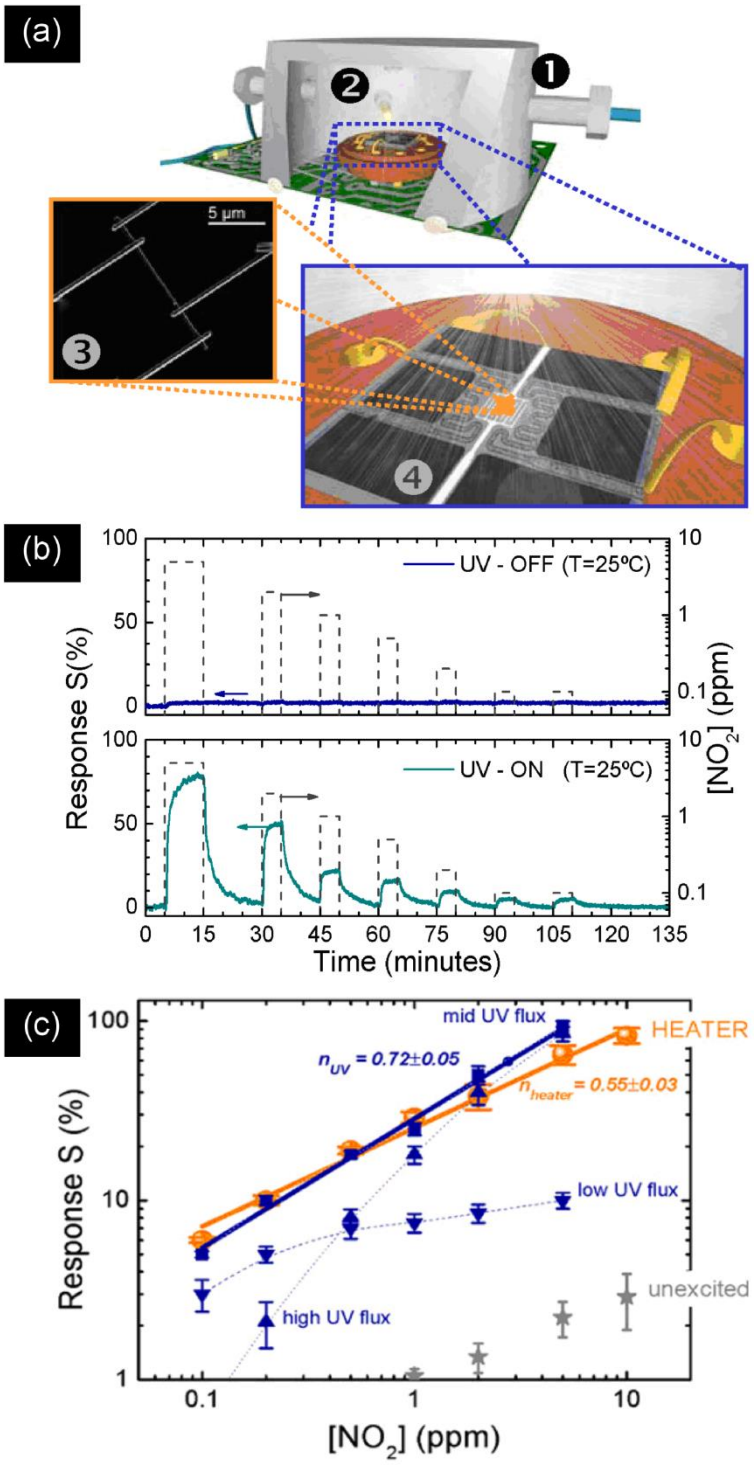

Figure 31. (a) Schematic representation of a nanowire device and experimental setup for UV promoted gas detection. The sensor is contained in (1) a gas tight measurement chamber with (2) embedded light sources. Active LED's trigger photoexcitation in the (3) individual nanowire, which is electrically contacted (in four-probes configuration) to (4) a microchip. (b) Response S of a SnO_2 nanowire, operated in dark and UV illuminated (Eph = 3.67±0.05 eV, ˚ph =30×1022 phm^{-2} s^{-1}), to NO_2 pulses of different

concentrations. Both measurements were carried out in the absence of external heating sources at room temperature (T = 25 °C). (c) Comparison of the sensor response when operated with conventional heating (T=175 °C) and UV illumination. The selection of the appropriate photon flux leads to sensor performances comparable to those of conventional heated sensors. Data presented in this figure correspond to the mean values of the responses obtained with 10 different devices and the error bars are the corresponding standard deviations. Reprinted from Ref. [406] with permission of Elsevier.

5.2 Nanowires for Energy Applications

Recent developments in materials research are related to energy storage or conversion. Progress in the design of semiconductor nanowires for enhanced thermoelectric efficiency has been demonstrated for Si nanowires [407] and the enhancement of the Seebeck coefficient by surface roughness has also been demonstrated [408]. The nanowire thermoelectric may find applications related to on-chip heat recovery, cooling and power generation, but are out of focus of the material class reviewed in this article. This section is devoted to generation of electrical energy by photovoltaic and mechanical energy conversion. Moreover, the impact of nanowire-based components on the storage of electrical power in lithium ion batteries will be highlighted

5.2.1 Electrical Power Generation

5.2.1a (Photovoltaics / Solar Cells)

The intention of this field of research is to capture the energy that is freely available from sunlight and convert it into a valuable asset, which is electric power. Photovoltaics (PV) take advantage of electron–hole pair formation in a semiconductor by impinging

photons and the creation of an electric potential across the interface between two materials. These solar cells are currently dominated by devices with junctions between inorganic solids (p-n junctions), but the liquid-solid combination to create a photochemical is also a valuable approach (exitonic solar cells) [409]. In both cases the charge carriers should be collected as electric current before recombination takes place.

Silicon nanowire heterostructures with doped segments can be formed either by VLS type growth or via etching techniques as described above. Large area fabrication of Si nanowires with low reflectance compared to Si thin films has been demonstrated (figure 32), which is beneficial for PV devices permitting their use without the necessity for anti-reflection coatings [410, 411]. The theoretical energy conversions using solid Si nanowire devices should be in the range between 15-18 % according to these investigations. Arrays of Si nanowires on glass substrates have been produced by electroless wet etching of a microcrystalline p-/n-/n^+ silicon stack on glass, which showed good performance as PV material [412]. Under AM 1.5 illumination open circuit voltages of V_{oc} = 450 mV and efficiencies up to 4.4 % were recorded in these devices.

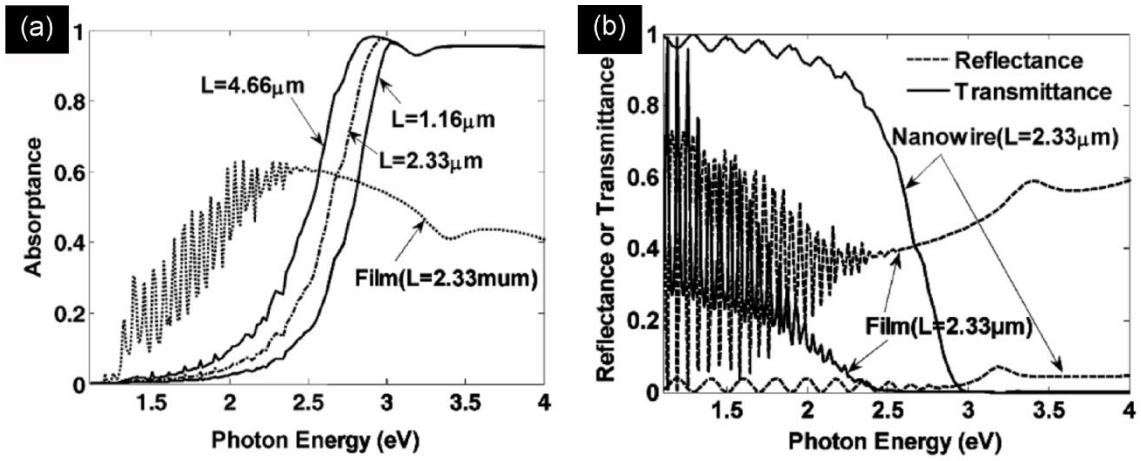

Figure 32. Radiative properties of nanowire structures with various thickness, (a) absorptance of nanowires with length of 1.16, 2.33, and 4.66 μm and nanowire diameter of 50 nm. The absorptance of a thin film is included as a reference. (b) illustrates the

reflectance of nanowires and the thin film. Reprinted from Ref. [411] with permission of ACS Publishers.

Investigations of PV properties at the single nanowire level could permit the determination of the intrinsic limits and potential benefits of nanoscaled devices and additionally reveal present flaws requiring further improvement. Individual coaxial p-type/intrinsic/n-type Si nanowires show efficiencies up to 3.4 % under 1-sun AM 1.5G illumination, producing 50–200 pW per nanowire at 1-sun illumination [413]. The output of these power supplies can be increased either by increasing the light intensity or using several coupled elements. For example, a single silicon nanowire PV device, operating under 8-sun illumination was used to drive a silicon nanowire pH sensor without additional power [413]. An amorphous shell of n-type silicon wrapped around a CVD-grown p-Si nanowire yielded core-shell diodes with $J_{sc} \sim 1.7$ mA/cm^2 and an efficiency of ~0.1 % for AM 1.5G illumination [414]. The open circuit voltage of the best devices was V_{oc}~ 130 mV, which is slightly lower than that of the single nanowire devices demonstrated by Tian (260 mV).

Recently, the realisation of a single nanowire tandem solar cell was described, which is basically an axial p-i-n+-p+-i-n silicon heterostructure as shown in figure 33. The device showed an average increase of 57 % in its open circuit voltage when compared to the single p-i-n device (figure 33) [415].

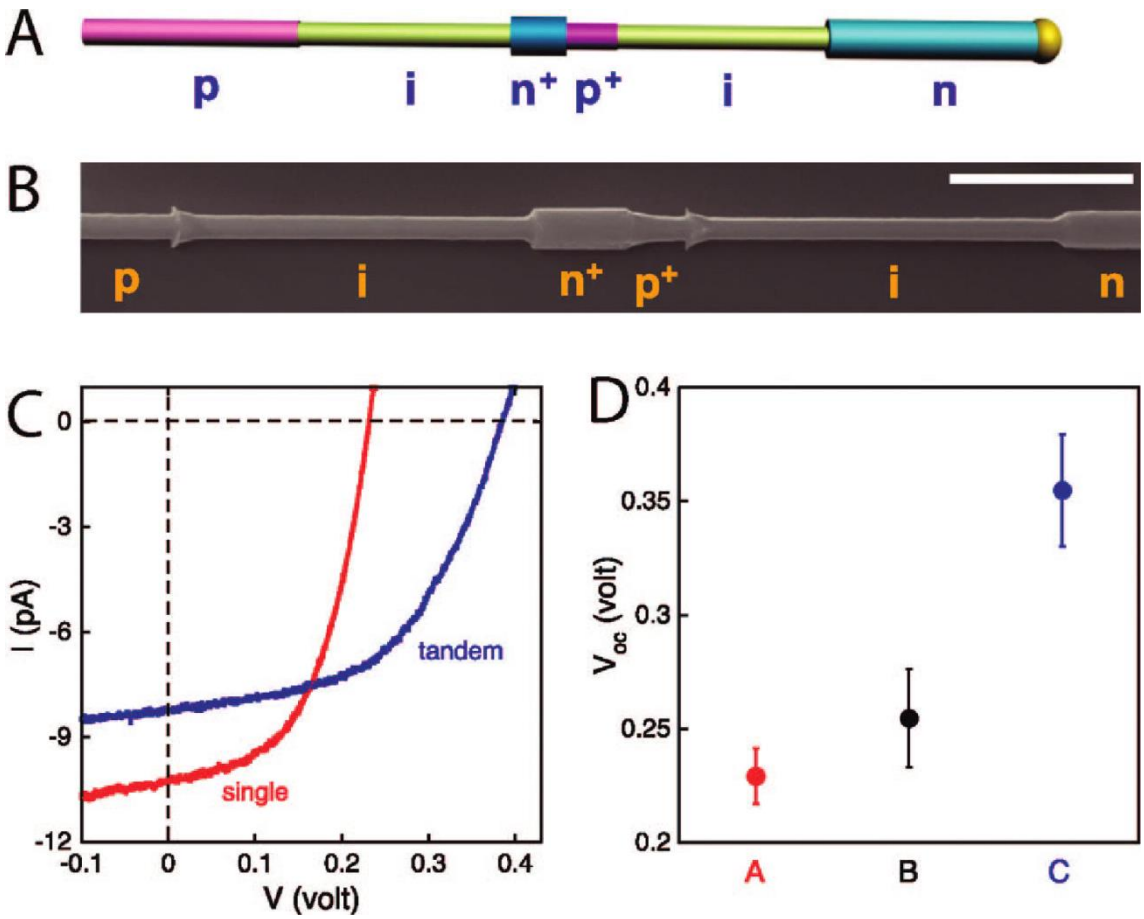

Figure 33. Tandem axial Si nanowire PV devices. (A) Schematic of two p-i-n diodes integrated in series on a single nanowire. (B) SEM images of a selectively etched tandem p-i-n+-p+-i-n Si nanowire; scale bar is 1 μm. (C) I-V responses recorded on p-i (2 μm) -n (red) and p-i-n+-p+-i-n, i) 2 μm (blue) Si nanowire devices under AM 1.5G illumination. (D) V_{oc} for p-i (2 μm) -n (red), p-i (4 μm) -n (black), and p-i-n+-p+-i-n, i) 2 μm (blue) axial Si nanowire devices. Error bars are ± 1 standard deviation. Reprinted from Ref. [415] with permission of ACS Publishers.

The V_{oc} values of single p-i-n radial and axial heterostructures are similar despite the very different diode junction geometries. This is most striking in comparison to the p-i-n axial versus coaxial Si nanowire devices where the junction areas differ by a factor of ~50-200 while the V_{oc}'s differ by only 10 %. While the much higher saturation current (I_0 = 3.24 pA) for a radial p-i-n Si nanowire device versus the axial p-i-n Si nanowire device (I_0 = 6.14 fA) reflects greater interfacial recombination in the former, the resultant effect on the V_{oc} is clearly not dominated exclusively by this factor. In both

configurations surface recombination effects could be responsible for the lower V_{oc} when compared to planar devices. However further investigations should be performed to obtain a deeper understanding of the defect density and surface recombination processes leading to the suppression of the absolute V_{oc} in both configurations, as the saturation current is three orders of magnitude higher in the radial heterostructure devices. The theoretical optimal dimensions should be obtained when the 1D structure has a radius approximately equal to the diffusion length of minority electrons and axial dimensions that are determined by the specific trade-off between the increase in J_{sc} and the decrease in V_{oc} with length for coaxial wires [416]. Besides the pure silicon heterojunction PV devices, a p-GaN nanorod array on n-Si exhibited a maximum power conversion efficiency of ~2.73 % under 1 sun simulated AM1.5 solar illumination with a high open-circuit voltage of ~0.95 V and a short-circuit current density of ~7.6 mA/cm^2 [417]. These studies highlight unique opportunities for integrated nanowire PV elements, yet the initial results show lower performance than state-of-the-art planar silicon devices at this stage. For further improvement, the defect/recombination centres should be minimized to facilitate the effective collection of photo-generated charges.

The first model system of Si nanowire-based electrochemical solar cells was recently fabricated by Mallouk and co-workers [418]. The Si nanowire Fermi level equilibrates with the electrochemical potential of the redox pair, leading to band bending and the formation of a space charge region where the photogenerated electrons and holes are separated. Photogenerated holes are subsequently collected and concentrated in the space charge region and transferred to the electrolyte (oxidation). An open circuit voltage of 230 mV was obtained, whereas under similar conditions a V_{oc} of ca. 500 mV was observed for p-Si single-crystal electrodes [419]. The cell included a Si nanowire

electrode, a platinum counterelectrode and a solution of 2 mM tris(2,2'-bipyridyl)ruthenium(II) hexafluorophosphate ($Ru(bpy)_3^{2+}$) (bpy) 2,2'-bipyridyl) and 100 mM tetra(*n*butyl) ammonium tetrafluoroborate ($TBABF_4$) in dry CH_3CN. At the same time, Maiolo *et al.* described an electrochemical solar cell based on unipolar n-type silicon nanowires in the 1,1'-dimethylferrocene $(Me_2Fc)^{+/0}$ redox system in CH_3OH [420]. The liquid electrolyte provided a convenient, conformal method of contacting the Si wires and allowed measurements of the performance of the wires without requiring a diffused metallurgical junction. The observed V_{oc} of 350-400 mV in these devices is relatively large given the high surface area per unit projected area. Similar findings were reported for another redox-system with the wire samples exhibiting superior performance to thin film electrodes [421]. The nanowire electrodes are sensitive to the light intensity, the doping level -which influences the dimension of the space charge region- and surface traps. Recently, Yuan et al. described experimental results with the optimal Si nanowire dimensions of ~ 20 μm length and ~ 150 nm diameter [422]. Longer wires would theoretically absorb more photons and thus generate more charges, but at the same time increased length includes more charge traps and scattering centres. The radial dimensions should not be significantly wider than the space charge region (~30 nm for the presented doping level), but the unaffected core should still be thick enough to transport charges efficiently.Exitonic solar cells include purely organic solar cells, hybrid solar cells and dye-sensitised solar cells, which will be described in this subsection. The principle of these photoelectrochemical cells was reviewed in detail by Gratzel in 2001 [409]. The anodes in dye-sensitised solar cells are typically constructed using sintered thick films of nanocrystalline oxides such as TiO_2, ZnO, SnO_2 and Nb_2O_5, or chalcogenides such as CdSe nanoparticles. The films exhibit a large internal

surface area to interact with the chromophore, but electrons injected into the semiconductor have to pass a large number of traps in the semiconductor materials before they are collected. The benefit of using these types of cells is the relatively low production costs and their applicability to almost any substrate. The negative charge carriers move through the bulk of the semiconductor to the current collector and the external circuit. The positive holes are driven to the surface where they are scavenged by the the redox-active molecule (R). Single crystalline nanowire electrodes can increase the effectiveness of charge collection, because they minimise losses due to traps and grain boundaries. The generally lower energy conversion efficiency is due to the lower surface area for dye adsorption and subsequently the energy transfer is limited. However, recently some approaches were published to overcome these limitations by different designs.Common to all these cells is an ultrafast initial charge separation step, occurring in femtoseconds, and a much slower back-reaction. Law *et al.* showed a full sun efficiency of 1.5 % using solution grown ZnO nanowires as shown in figure 34, while the device performance was primarily limited by the surface area and low dye loading of the nanowire surface [423]. At a full Sun intensity of 100 ± 3 mW cm^{-2}, the highest-surface-area devices were characterised by J_{sc} = 5.3–5.85 mA cm^{-2}, V_{oc} = 0.61–0.71 V and efficiencies of 1.2-1.5 %. In addition, the diffusion coefficients of the nanowire samples were two orders of magnitude higher than that reported for TiO_2 and ZnO based devices.

The importance of the surface area available for dye adsorption was described by comparison of devices with a low density of straight wires and dendritic wires with almost the same trunk number, respectively [272]. Typical solar cell photocurrent, photovoltage, and overall efficiencies of 1.3 $mAcm^{-2}$, 0.7 V and 0.3% are described for

8 μm long nanowires [424]. Photocurrent and efficiency increase with nanowire length and improved light harvesting, while internal quantum efficiencies are similar for nanowires of all lengths, indicating that electron transport is not limited by the nanowire dimensions.

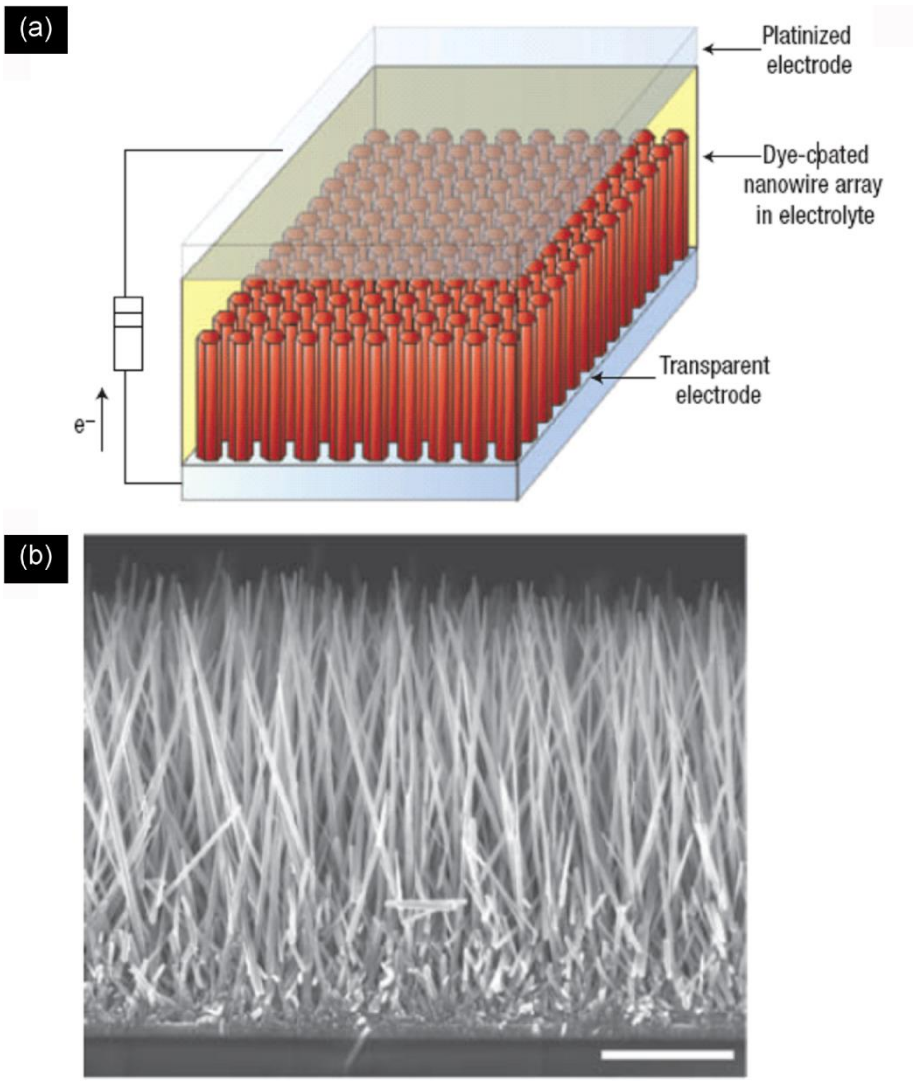

Figure 34. The nanowire dye-sensitised cell, based on a ZnO wire array. (a) Schematic diagram of the cell. Light is incident through the bottom electrode. (b) Typical scanning electron microscopy cross-section of a cleaved nanowire array on FTO. The wires are in direct contact with the substrate, with no intervening particle layer. Scale bar, 5 μm. Reprinted by permission from Macmillan Publishers Ltd: Nature Materials [423], copyright (2005).

Branching of 1D ZnO nanostructures enhances the dye absorption and leads to an increase in efficiency from 1.0 % to 1.9 % and higher short circuit current for zinc oxide nanoflowers in comparison to straight wires [425]. Similarly, a superior performance of ZnO-NW array/NP composite dye-sensitised solar cell compared to that of the ZnO nanowire cell is described [426]. The enrichment of the light harvesting and the reduction of the electron back reaction on the TCO surface without significantly sacrificing electron transport efficiency at the same time is achieved by synthesising dense nanoparticles among the ZnO NW array.

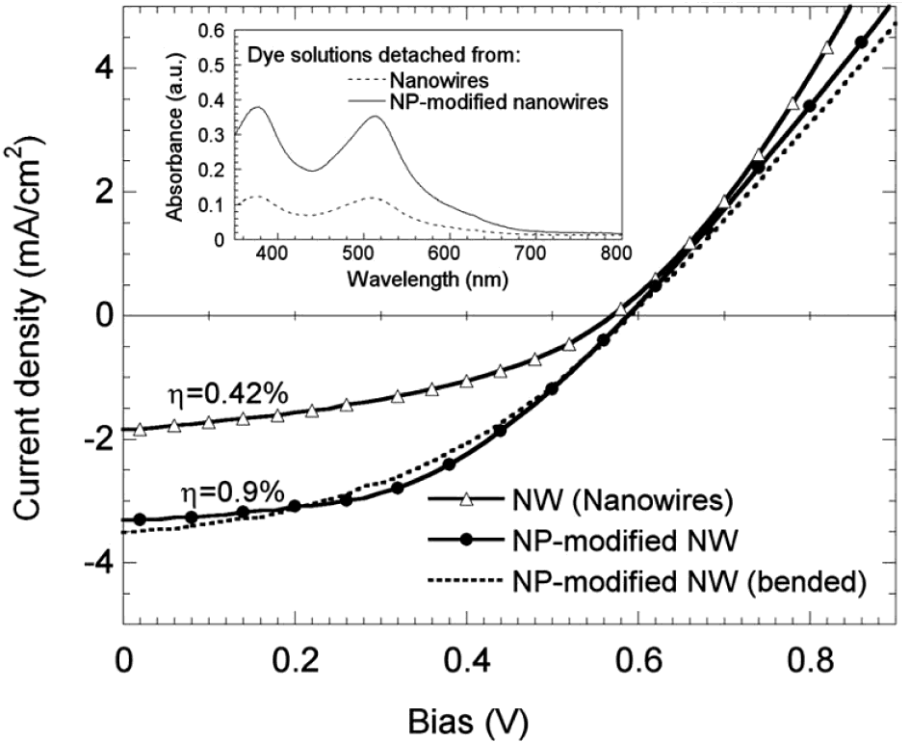

Figure 35. Current-voltage I-V characteristics of dye-sensitised solar cells constructed using ZnO nanowires (triangle) and NP-modified ZnO nanowires (circle), and the I-V curve (dashed) of the NP-modified ZnO-nanowire DSSC after bending to 5 mm radius for 5 cycles under illumination: 100 mW/cm2, AM1.5G. Inset: absorptions of dye solutions containing dyes from ZnO-nanowire film (solid) and NP-modified ZnO-nanowire film (dashed), respectively. The dye solutions were prepared by detaching dye molecule from 1 cm^2 ZnO film (nanowires or NP-modified nanowires) into 8 ml KOH (0.1 mM) aqueous solution. Reprinted from Ref. [425] with permission of American Institute of Physics.

Using a similar approach to fabricate bendable devices, allowed the combined flexibility of the nanowire based devices and enhanced performance of a particle based cell due to higher dye loading (figure 35) [427]. ZnO-Al_2O_3 and ZnO-TiO_2 core-shell nanowire dye sensitised solar cells have been compared to cells built from ZnO nanowires without shells and showed coating dependent device performance [428]. Thin Al_2O_3 shells act as tunnel barriers that reduce recombination only at the expense of a larger reduction in electron injection yield and lower device efficiency. TiO_2 shells suppress recombination and markedly improve cell open-circuit voltage and fill factor, leading to efficiencies of 2.25 % under 100 mW cm^{-2} AM 1.5 simulated sunlight. The superior performance of the ZnO-TiO_2 core-shell nanowire cells is a result of a radial surface field within each nanowire that decreases the rate of recombination in these devices. However, the 2D design still limits the surface area for dye absorption by the requirement that the electron transport distance remains significantly smaller than the electron diffusion length in order to minimize the recombination of electrons and holes. A potential solution to overcome this limitation is presented by Weintraub et al. who describe a hybrid structure that integrates optical fibres and ZnO nanowires as 3D dye-sensitised solar cells [429]. The distance between the counterelectrode and the active nanowire electrode should be small, which impliies that only 3 sides of the waveguiding fibre are decorated with nanowires and the fourth serves as a mirror that deflects the light back to the active side and thus increases the energy conversion efficiency to 3.3 %. This configuration allows light to have multiple interactions with the dye molecules and the cell can be located in a device without direct contact to the light source, which would be beneficial for surface confined applications, due to the use of optical fibres.

Despite the significant progress in recent years, the degradation and lifetime of the organic component must be considered for dye-sensitised solar cells. In addition, the theoretical advantages of nanowire-based cells, such as the higher carrier transport properties, do not overcompensate their limitations in surface area for dye adsorption. Therefore, nanoparticle dye-sensitised solar cells are still superior to their nanowire counterparts, which makes up for their inferior carrier transport properties. Further research and optimization of devices and components is required to exploit the limits of nanowire-based dye-sensitised solar cells.

In addition to the organic dyes, inorganic nanoparticle sensitised solar cells are also described, such as CdSe quantum dot decorated ZnO wires (figure 36) [430]. Using a liquid electrolyte containing I^-/I_3^- the viability of the approach was demonstrated and power conversion efficiencies of 0.4 % and open circuit voltages in the range of 0.5-0.6 V are obtained. However, this approach should allow tuning of the optical absorption in the solar cell through appropriate selection of semiconductor material and particle size. Moreover, higher efficiencies could be expected through multiple electron-hole pair generation per photon in the semiconductor particles. All oxide solar cells using ZnO wire electrodes, TiO_2 blocking layer and Cu_2O nanoparticle light absorbing material show promising long term stability, but the efficiencies are still pretty low (0.053 %) [431]. However, this proof-of-concept device is a promising result for the realisation of an exitonic all-inorganic solar cell by choosing appropriate material combinations and processing strategies

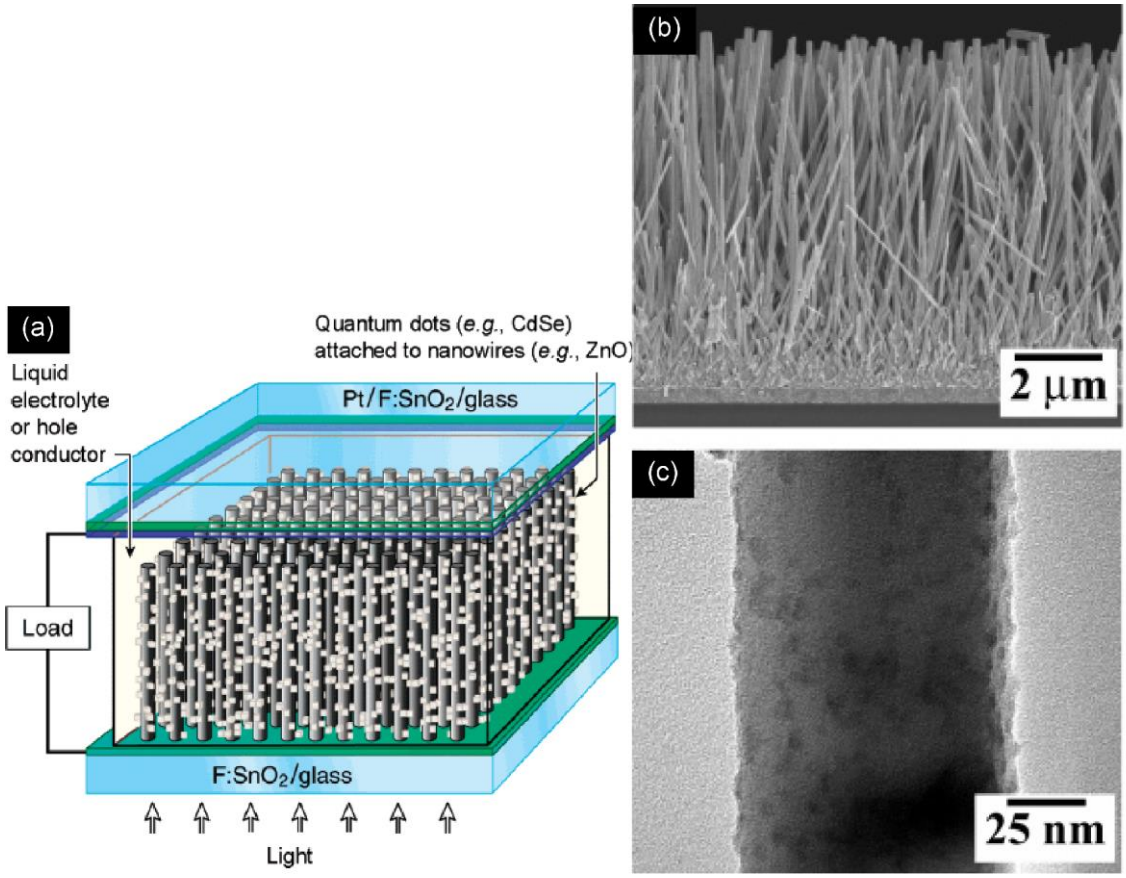

Figure 36. (a) Schematic of the quantum-dot-sensitized solar cell. An array of ZnO nanowires, grown vertically from an F-doped SnO2/ glass substrate and decorated with CdSe quantum dots, serves as the photoanode. A second F-doped SnO2/glass substrate, coated with a 100 Å layer of Pt, is the photocathode. The space between the two electrodes is filled with a liquid electrolyte, and the cell is illuminated from the bottom, as shown. (b) Cross-sectional scanning electron micrograph of ZnO nanowires. (c) Bright-field transmission electron micrograph of a ZnO nanowire decorated with CdSe quantum dots. Reprinted from Ref. [430] with permission of ACS Publishers.

5.2.1b Nanogenerators

An approach that converts mechanical energy into electric power using aligned ZnO nanowires was described for the first time by Z. L. Wang *et al.* [432]. The devices were based on vertical aligned ZnO nanowires grown on a *c*-plane oriented α-Al_2O_3 substrate covered by a layer of ZnO film. Contact-mode atomic force microscopy images of both the topography (feedback signal from the scanner) and the corresponding output voltage across the load were recorded simultaneously as the conductive AFM tip scanned over

the nanowire arrays. In the voltage output images, many sharp output voltage peaks were registered at the locations of the nanowires. The physical principle for creating, separating, and preserving piezoelectric charges in the nanowires is a coupling of piezoelectric and semiconducting properties [433]. The piezoelectric effect is required to create electric potential of ionic charges from elastic deformation by the AFM tip creating a strain field, with one surface being stretched and the opposite surface compressed, which results in an electric field along the nanowire. The semiconducting property is required to preserve the charges and then release the potential via the rectifying behaviour of the Schottky barrier at the metal-ZnO interface, which serves as a switch in the entire process. Theoretical calculations showed that the maximum potential at the surface of the nanowire is directly proportional to the lateral displacement of the nanowire and inversely proportional to the cube of the length-to-diameter aspect ratio of the nanowire [434]. The magnitude of piezoelectric potential for a nanowire of diameter 50 nm and length 600 nm is ~0.3 V. The effect of the piezoelectric properties underlying the ZnO based power-generating devices is questioned by Alexe *et al.* [435]. The presented model and results are similar for Si and ZnO, which shows that the piezoelectric effect is not responsible for the electrical output they observe. However, it represents an example that these electrical effects should be measured and interpreted with caution to avoid contradicting results [436].

The design of a nanowire nanogenerator includes vertically aligned zinc oxide nanowire arrays with a counterelectrode which is driven by an ultrasonic wave to produce continuous direct-current output [437]. The Schottky contacts are realised by a zigzag metal electrode with a small gap between the wires and the contacts. The wave drives the electrode up and down to bend and/or vibrate the nanowires and the

piezoelectric semiconducting coupling process converts mechanical energy into electricity. The zigzag electrode acts as an array of parallel integrated metal tips that simultaneously and continuously create, collect, and output electricity from all of the nanowires (figure 37). The stability of the generated current output over more than one hour also shows the applicability of this concept.

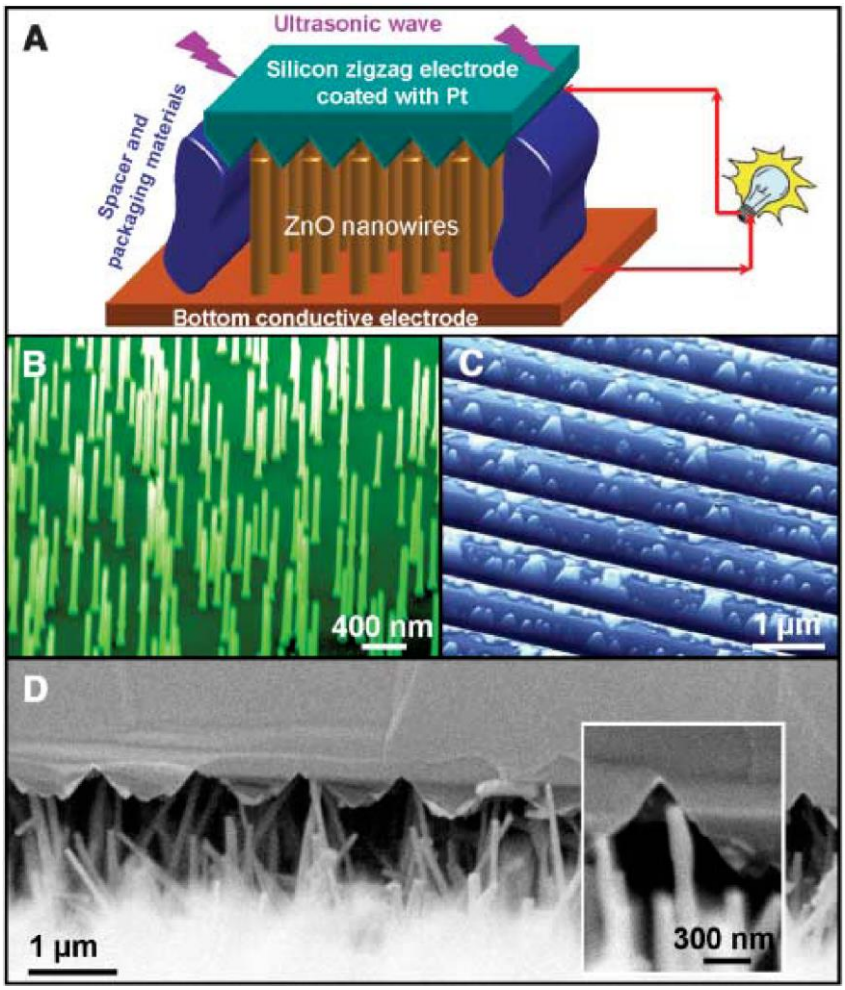

Figure 37. Nanogenerators driven by an ultrasonic wave. (A) Schematic diagram of the nanogenerator. Aligned ZnO nanowires are grown on a solid/polymer substrate, covered by a zigzag electrode and the substrate as well as the electrode are directly connected to an external load. (B) Aligned ZnO nanowires grown on a GaN substrate. The gold catalyst particles used for the growth had been mostly vaporised; thus, the final nanowire were purely ZnO with flat top ends. (C) Zigzag trenched electrode fabricated by the standard etching technique after being coated with 200 nm of Pt. The surface features are due to non-uniform etching. (D) Cross-sectional SEM image of the nanogenerator, which is composed of aligned NWs and the zigzag electrode. (Inset) A typical nanowire that is forced by the electrode to bend. Reprinted from Ref. [437] with permission of The American Association for the Advancement of Science.

While this device is operated in pure water, the same device are successfully used in biofluids under ultrasonic actuation and the potential of increasing the output current and voltage is demonstrated [438]. The potential of increasing output current and voltage is illustrated by connecting multiple NGs (nanogenerators) in parallel and series, respectively, unambiguously demonstrating the possibility of raising output power by three-dimensional integration and architecture. Three-dimensional integrated multilayer nanogenerator architectures based on stacks of ZnO nanowires and metal coated ZnO nanotips as electrodes, grown on two opposite surfaces of a silicon wafer, are shown to increase the output current, voltage and power as described for single device electrical circuits [439]. A layer-by-layer stacking of the as-fabricated Si wafers forms an integrated architecture that demonstrates a linear superposition of current and voltage for parallel and serial connection, respectively. Advantages of this procedure include the wet chemical synthesis of both wires and nanotips at low temperature (< 100 °C), and a simpler synthesis process due to the variability of nanostructure length given flexible interaction of electrode and ZnO wires. The low temperature growth of ZnO nanowires on any material allows the decoration of textile microfibers to produce 1D hybrid structures with potential for energy scavenging (figure 38) [440]. The approach uses a similar configuration to that described previously with one metal coated ZnO NW yarn as an electrode and others as power generating fibres and permits the fabrication of flexible, foldable, wearable and robust power sources in any shape, with enhanced output electricity using a bundle of fibres as a yarn, which is the basic unit for fabrics. Moreover, the operation frequency of these nanogenerators is very low and in the range of mechanical vibrations, such as footsteps, which broadens the field of applications of these nanogenerators. The optimum output power density from such

textile fabrics is estimated to be in the range of 24-16 mW per square metre of fabric [441].

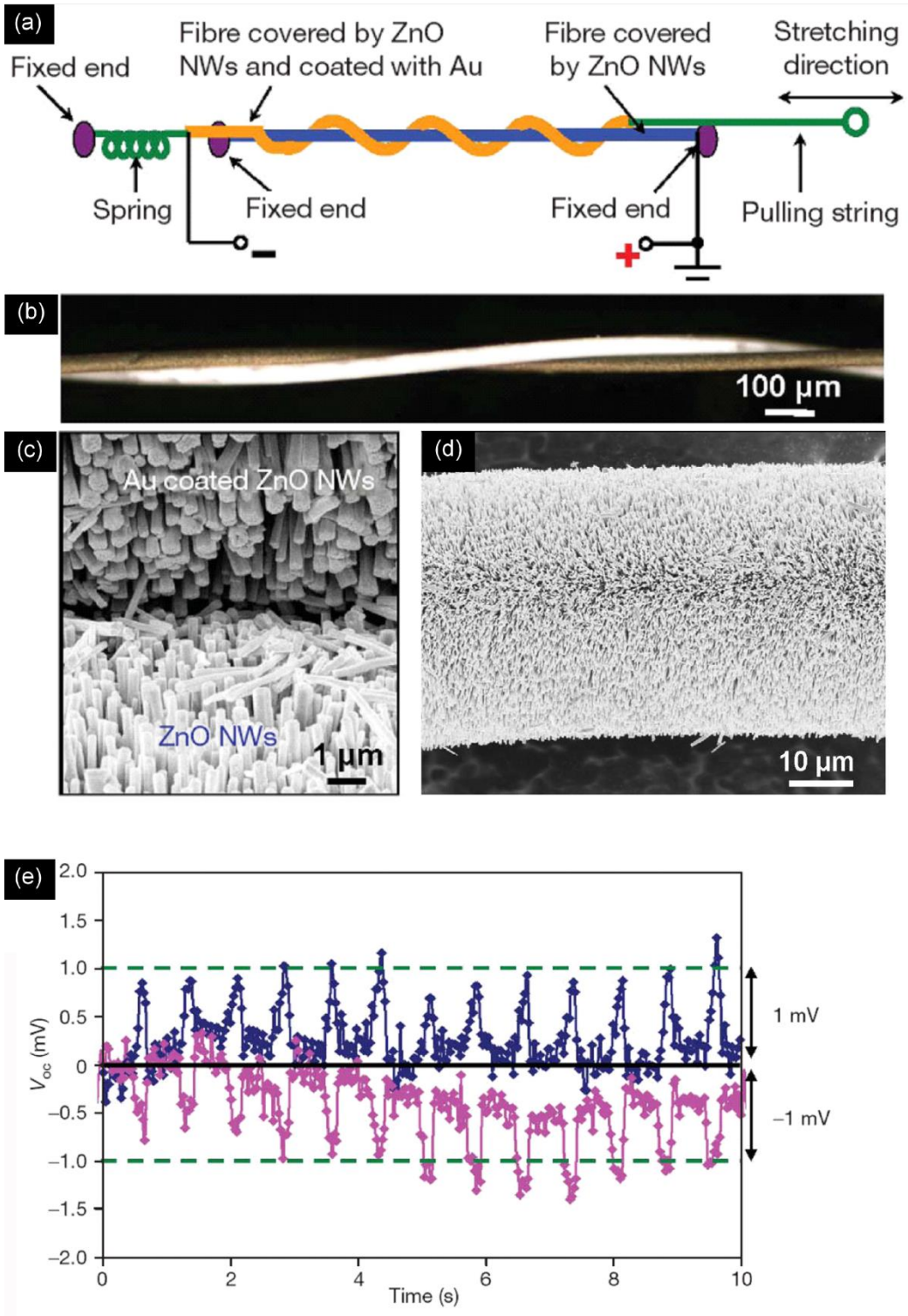

Figure 38. (a) Schematic experimental set-up of the fibre-based nanogenerator. (b) An optical micrograph of a pair of entangled fibres, one of which is coated with Au (in darker contrast). (c) SEM image at the 'teeth-to-teeth' interface of two fibres covered by

nanowires, with the top one coated with Au. The Au-coated nanowires at the top serve as the conductive 'tips' that deflect/bend the nanowires at the bottom. (d) individual ZnO nanowire coated Microfiber and (e) output of a device the open-circuit output voltage (V_{oc}) of a double-fibre nanogenerator measured by applying an external pulling force. When the measurement circuit was forward connected to the nanogenerator, which means that the positive and negative probes were connected to the positive and negative output electrodes of the nanogenerator, respectively, the output signals are represented by a pink curve. By reversing the polarity of the connection of the nanogenerator output electrodes, the output signals are presented by the blue curve. Reprinted by permission from Macmillan Publishers Ltd: Nature [440], copyright (2008).

Similarly to the vertical generators, the use of laterally assembled ZnO wires is also feasible to create energy by bending the support [442]. In addition, these studies on micron-sized wires show the necessity of Schottky contacts to observe a sufficient power generation with energy conversion efficiency as high as 6.8 % by cyclic stretching–releasing of the nanowire with a strain of 0.05–0.1 %. Biomechanical energy conversion from muscle stretching, such as bending of a finger or the running of a hamster, showed the power generation from vertical single-wire devices on flexible substrates [443]. The serial connection and synchronisation (electrical output in phase) of up to four individual single-wire nanogenerators allowed producing an output voltage of up to ~0.1-0.15 V. Validation of the charge separation effect by the bending ZnO nanowires was demonstrated with bottom-gate and top-gate ZnO nanowire FETs in horizontal geometry using polymer dielectrics on plastic substrates and various strains to bend the FET devices [444]. The piezoelectric effect on ZnO nanowires induced by bending the flexible substrate influences the electrical transport characteristics of ZnO nanowire FETs in terms of current levels, transconductance, mobility, and threshold voltage. The different behaviour of the back and top-gated devices can be explained by the piezoelectric effect with the electron trapping effect at the interfaces between the nanowire and the dielectrics.

The charge separation and the effective power generation are not limited to ZnO nanowire devices. Piezoelectric semiconducting axial heterostructures such as ZnO/ZnS wires as well as pure ZnS [445] and CdS [446] nanowires also show potential for use in nanogenerators, the mechanism of which is the same as that for ZnO-based devices. The effectiveness of CdS nanogenerators can also be influenced by the crystallographic phase, with higher output for pure wurtzite wires.

5.2.2 Energy storage (Lithium ion batteries)

A key issue for future energy supply and use of alternative energy sources are effective storage media, such as batteries. It is well known that the capacity loss is often caused by stress-induced material failure arising from the volume change in charging and discharging reactions. Therefore, high surface to volume ratio structures, which additionally contribute to higher conduction values, are promising materials for lithium ion battery anodes. For many metal oxides, which do not form Li intercalation compounds, the reduction and formation of metallic species is mandatory for the effective incorporation of Li in the electrode material, which includes the formation of Li_2O in the first cycle and can be expressed by: $M_xO_y + 2y\ Li \rightarrow x\ M + y\ Li_2O$

The formed metal reacts with the reduced Li atoms to form an alloy which acts as the storage medium. Tin oxide is one of the most promising materials for lithium ion batteries due to the high amount of Li which can theoretically be alloyed in metallic tin ($SnLi_x$ with $x \leq 4.4$). The battery with SnO_2 nanowires as an anode electrode is discharged (Li inserted) and charged (Li released) at room temperature. First experiments with SnO_2 describe a good performance of the SnO_2 nanowire / carbon

black anodes used in these studies [447]. During the first successive 15 cycles, the reversible capacity stays in the range of 1250–700 $mAhg^{-1}$ with a capacity fading of 3.89 % per cycle. In addition, the formation of nanoparticles on the wire surface is observed after Li intercalation (figure 40b). Lower capacity fading of 1.45 % per cycle is described for self-catalyzed SnO_2 nanowires after the 5^{th} cycle, but lower reversible capacity also [448]. Nanowire samples were compared with SnO_2 particles and exhibit improved cyclic performance with a higher reversible specific capacity of over 300 $mAhg^{-1}$ up to the 50th cycle. In another report, the effect of morphological modification on the electrochemical performance of SnO_2, using three different types of tin oxide nanomaterials (nanotubes, nanowires, and nanopowders) for use as anode materials have been investigated [449].

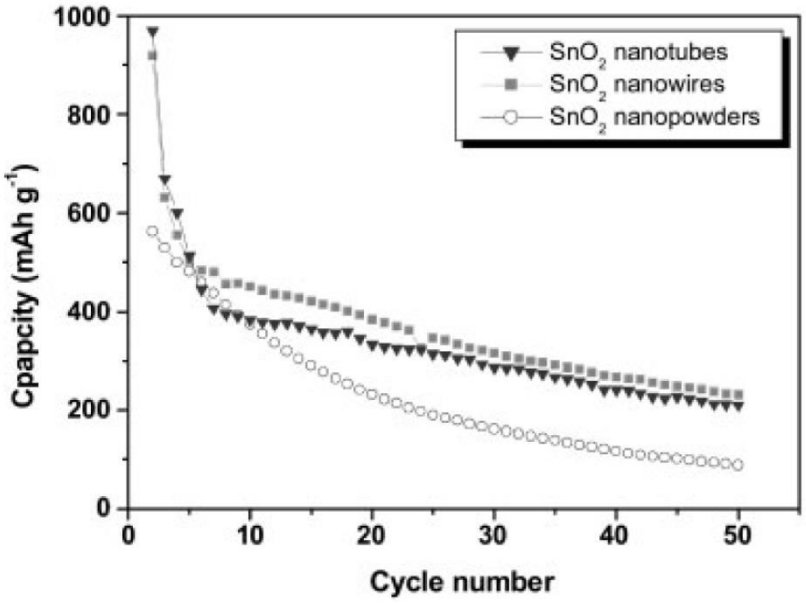

Figure 39. The anodic performances of the SnO_2 nanomaterials: (a) the galvanostatic voltage profiles between 0.05 V and 1.50 V for the first cycle, (b) the cyclic performance of SnO_2 nanomaterials up to the fiftieth cycle at the same current density, 100 mA g^{-1}. Reprinted from Ref. [449]. Copyright Wiley-VCH Verlag GmbH & Co. KGaA. Reproduced with permission.

SnO_2 nanowire and nanotube electrodes exhibited a higher reversible specific capacity of over 300 $mAhg^{-1}$ up to the fiftieth cycle, with relatively stable cyclic

performance, whereas the nanopowder electrode showed an abrupt capacity fading. The average capacity fading of the nanowires and nanotubes was estimated to be 1.45 % and 1.87 % per cycle after the second cycle, which was much smaller than that of the SnO_2 nanopowders, at 3.46 %. The very small disparity between the cyclic retention of the nanowires and nanotubes implies that the electrochemical improvement in nanowires and nanotubes should be mainly attributed to their 1D microstructure. Considering that the faradaic reaction is determined by ion transfer and electron conduction, the better electronic conductivity of the nanowires is assumed to play the crucial role in the reduction of the resistance.

Partial reduction of SnO_2 nanowires in a hydrogen plasma lead to well separated Sn nanoparticles on SnO_2 NWs (figure 40) [450]. The increased Sn:O ratio, good separation and high density of the Sn nanoclusters on the surface lead to a reversible storage capacity greater than 800 $mAhg^{-1}$ over 100 cycles. These hybrid structures with improved stable capacity can relieve the stresses associated with volume changes better than pure phase SnO_2 nanowires. However, TEM images of the Sn/SnO_2 resemble the results for pure SnO_2 NWs after cycling, which also show the formation of metallic particles on the wire surface as shown in figure 40 [447]. The capacity fading after the first few cycles is the lowest at less than 1 % per cycle and post-lithiated samples show the intact hybrid structure after 100 cycles.

SnO_2/In_2O_3 co-axial heterostructures show an increase of the specific capacity by 60 % when compared to pure tin oxide nanowires [451]. The formation of In metal during cycling is described, which does not act as lithium storage media but enhances the overall conductivity facilitating efficient charging. A reversible capacity of ~700 $mAhg^{-1}$ after 10 cycles was observed for the SnO_2-In_2O_3 nanowires.

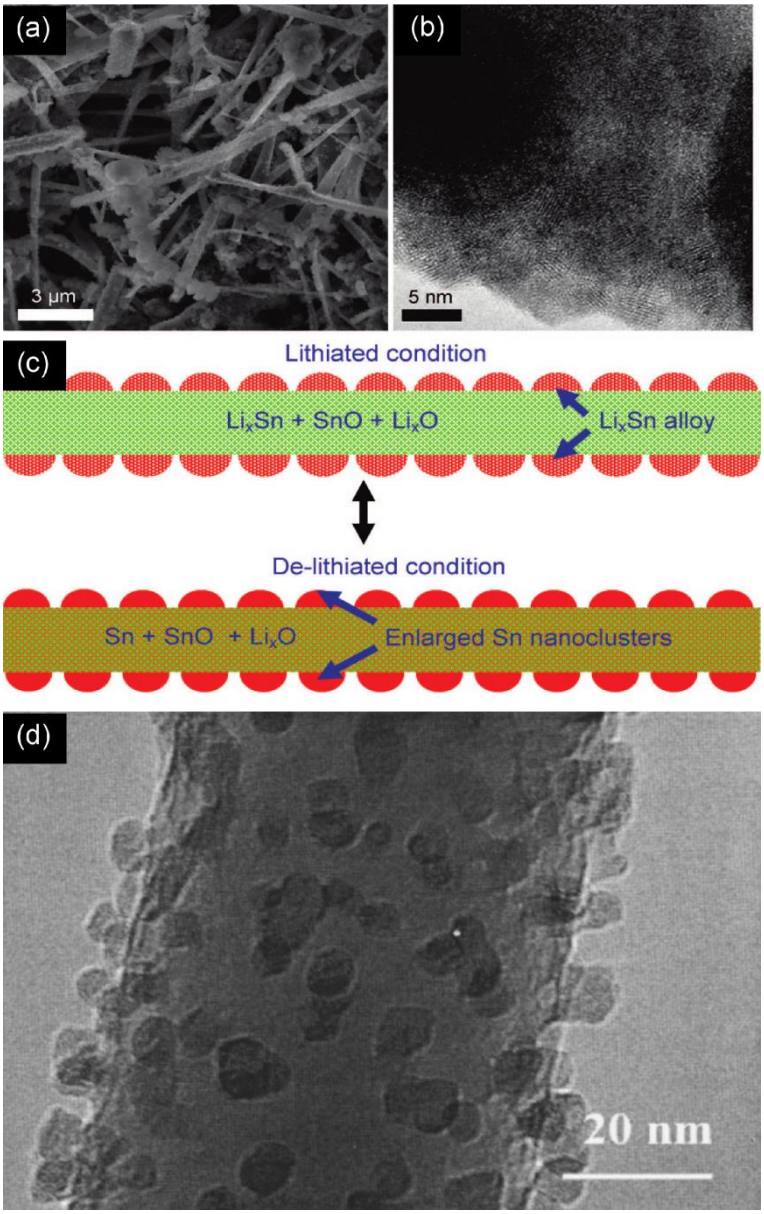

Figure 40. Characterisation of hybrid structures after 100 cycles of charge and discharge. (a) SEM image of hybrid nanowires. (b) HRTEM image of the Sn nanocluster-covered SnO_2 nanowires. (c) A schematic illustrating the reversible Li alloying and dealloying steps in the Sn-nanocluster-covered-SnO_2 nanowires. (Reprinted from Ref. [450] with permission of ACS Publishers.) (d) TEM image of a Li-intercalated single-crystalline SnO_2 nanowire. Lots of nanoparticles are observed on the surface of the nanowire which can be attributed to Sn/Sn-Li species, similar to the findings in plasma treated tin oxide wires before cycling. Reprinted from Ref. [447] with permission of American Institute of Physics.

Tin oxide carbon nanotube core-shell heterotubes also prevented the tin oxide material from degradation and can be repeatedly charged and discharged up to 200

cycles with good cyclability [452]. The initial specific capacity of 586 $mAhg^{-1}$ was reduced to 542 $mAhg^{-1}$, or 92.5 % of the initial capacity after 200 cycles. The capacity fade rate was only 0.0375 % per cycle, which placed it on par with the performance of commercially available graphite-based anodes (< 0.03 % per cycle) but with superior capacity. The outstanding electrochemical properties are likely to be related to several unique features of this nanocomposite: tubular organization of tin-oxide nanoparticles, stress absorption by the CNT matrix, and the existence of a hollow interior allowing freedom of expansion, increased electrical contact, and enhanced lithium-ion transport. The inverse heterostucture with tin oxide nanocrystal decoration of carbon nanotubes also showed a good specific capacity of more than 400 $mAhg^{-1}$ after 30 cycles, however the performance of this configuration was not as stable as the configuration described above [453]. Difficulties in comparing the results are due to insufficient data of SnO_2 loading. However, SnO_2 decorated carbon nanotubes were also shown to display very high reversible capacities and excellent cyclability, which was confirmed by the cyclic performance with reversible capacities in the range of 1002–900 $mAhg^{-1}$ (fade rate 0.102 % per cycle) during 100 cycles [454].

1D group IV semiconductors have recently gained tremendous attention for use in lithium battery anodes due to the demonstration of incredibly high specific capacity of silicon nanowires. Theoretically silicon can incorporate 4.2 equivalents of lithium during alloying, which corresponds to a 400 % increase in volume. This fact traditionally limited the applicability of Si in anode materials for lithium ion batteries, because the material tended to crack or degrade under the huge strain accompanied with the Li incorporation. Recently, Chan *et al.* demonstrated huge capacities of CVD-grown Si nanowire anodes [455]. Significantly, the observed capacity during this first charging

operation was 4,277 $mAhg^{-1}$, which is essentially equivalent to the theoretical capacity within experimental error. The first discharge capacity was 3,124 mAh g^{-1}, indicating a coulombic efficiency of 73 %. However this low efficiency is likely to be a result of the formation of passivating solid electrolyte interphase layers and not due to surface oxides [456]. The second charge capacity decreased by 17 % to 3,541 $mAhg^{-1}$, although the second discharge capacity increased slightly to 3,193 mAh g^{-1}, giving a coulombic efficiency of 90 %. Both charge and discharge capacities remained nearly constant for subsequent cycles, with little fading up to 10 cycles, which is considerably better than previously reported results for nanocrystalline and amorphous thin films [457]. Improved cycling performance was observed when tuning the voltage cutoffs to avoid large changes in the solid electrolyte interphase morphology, suggesting that the cycle life in Si nanowire anodes may rely greatly on the solid electrolyte interphase layer [456].

After the discharge the Si nanowires became amorphous and no crystalline alloys were observed in *in-situ* XRD measurements. Potential spectroscopy analysis revealed four different amorphous lithium silicides which can contribute to the reversibility and cycling retention as demonstrated by galvanostatic studies at different rates and voltage cutoffs [458]. The increased volume of the anode material, by incorporation of lithium, leads to axial and radial expansion of the nanowires to release the strain that is typically responsible for the pulverisation of the silicon anode materials. Both effects were observed in Si nanowires after charging. An increase in nanowire diameter and a wrapping of the nanowires around a predeposited rigid nickel backbone in a helical manner were observed as shown in figure 41 [455].

The destruction of the Si lattice during Li insertion is described in an earlier report by Li *et al.*, which also reports the partial reconstruction of small Si crystals within the nanowire after Li extraction [459]. A solution to retain the crystalline Si as structure directing conductive backbone is presented by Cui *et al.* using vapour grown crystalline-amorphous core-shell Si nanowires [460]. The amorphous Si shells can be selectively electrochemically activated due to the difference of the lithiation potential of crystalline and amorphous silicon. Therefore, crystalline Si cores function as a stable mechanical support and an efficient electrical conducting pathway while amorphous shells store Li+ ions. These core-shell nanowires have high charge storage capacity (~1000 $mAhg^{-1}$) with ~90 % capacity retention over 100 cycles and show excellent electrochemical performance at high rate of charging and discharging (6.8 A/g, ~20 times that of carbon at 1 h rate).

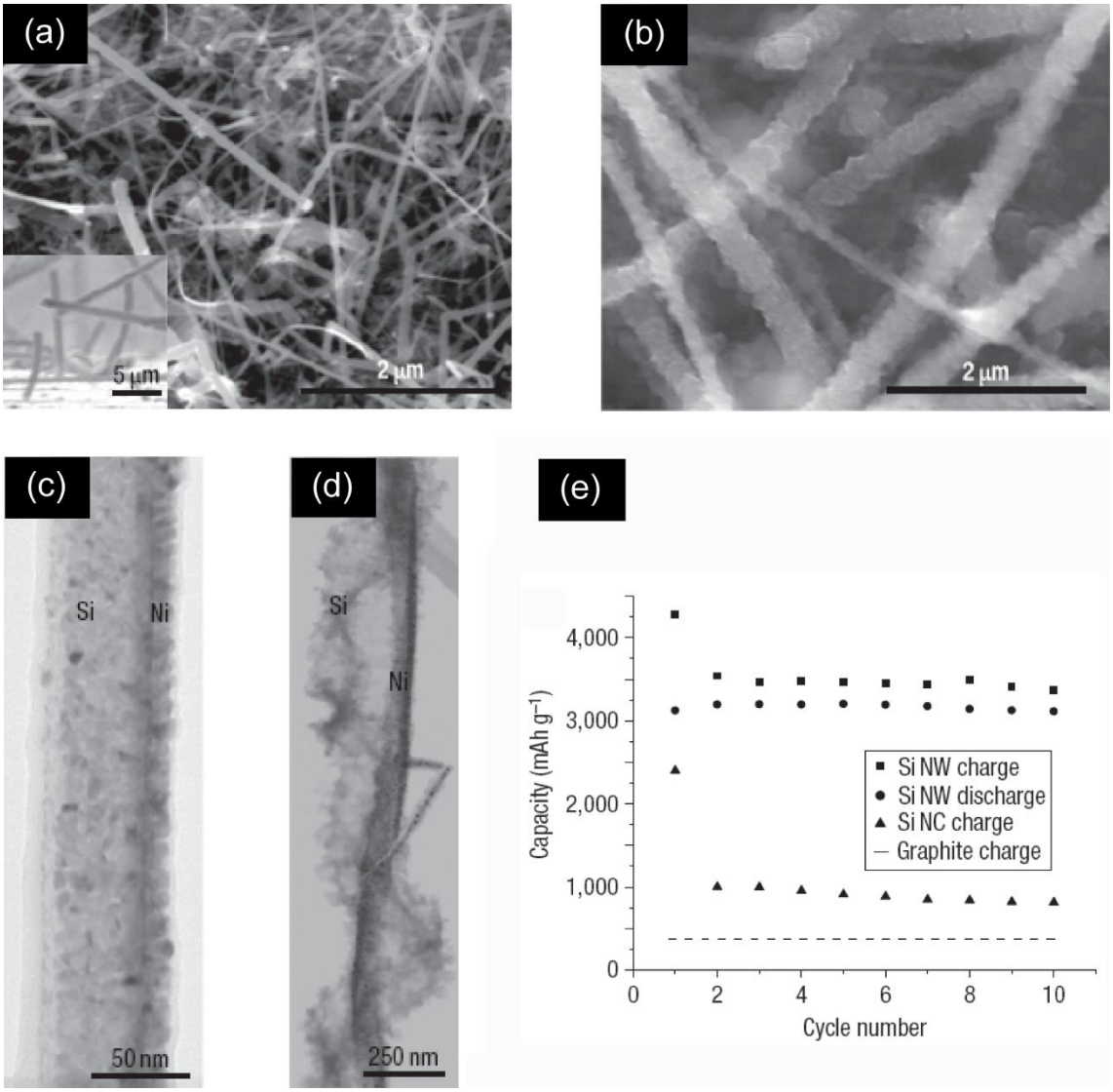

Figure 41. (a) SEM image of Si nanowires before (a) and after (b) electrochemical Li intercalation cycles (same magnification). The inset in (a) is a cross-sectional image showing that the nanowires are directly contacting the stainless steel current collector. (c), (d) TEM images of a Si nanowire with a partial Ni coating before (c) and after (d) Li cycling. (e) Capacity versus cycle number for the Si nanowires at the C/20 rate showing the charge (squares) and discharge capacity (circles). The charge data for Si nanocrystals (triangles) and the theoretical capacity for lithiated graphite (dashed line) are shown as a comparison to show the improvement when using Si nanowires. Reprinted by permission from Macmillan Publishers Ltd: Nature Nanotechnology [455], copyright (2008)

Large-area, wafer-scale silicon nanowire arrays prepared by metal-induced chemical etching are also described as promising scalable anode materials for rechargeable lithium batteries [461]. However, the exact Si nanowire loading per surface area in the silicon electrode is hard to estimate. Therefore, it is not possible to make a reliable comparison between the specific capacity of this Si nanowire anode and that of the VLS-CVD Si nanowire anode, particularly since the contribution of the Si wafer substrate is unknown. Similarly, silicon coated carbon fibres (Si/C ratio ~3:1) revealed high specific capacities of 2000 $mAhg^{-1}$ after 30 cycles at a charging rate of C/5 [462]. Solution-based synthesis of carbon sheated Si nanotubes showed enormous 89 % coulombic efficiency in the first cycle and revealed a capacity retention of 89 % after 200 cycles [463].

Similar to Si nanowire anodes, vapour grown Ge nanowires are also a viable candidate for anode materials with stable discharge capacities of 1141 $mAhg^{-1}$ over 20 cycles without pulverisation of the material [464]. The Coulombic efficiency for the third to 20th cycle is 84-96 %, showing reversible cycling after the surface reactions, such as oxide lithium interactions and formation of a surface-electrolyte interphase film due to electrolyte decomposition, are completed. Table 2 summarises the results obtained using 1D semiconductor materials as lithium ion battery anodes and gives the value of reversible specific capacity of the commercially used graphite anode. However changes in charge/discharge rate affects the specific capacity, which is not considered due to variations in the procedures the electrochemical characterisation was carried out.

Table 2: Specific capacity of 1D semiconductor anodes in comparison to graphite.

Material	Investigated cycles (number)	Specific Capacity at last cycle (mAh g^{-1})	Reference
Graphite		~310	[465]
SnO_2 NWs	15	~700	[447]
	50	~300	[448]
SnO_2 NTs	50	~300	[449]
SnO_2/Sn NWs	100	~800	[450]
SnO_2/In_2O_3 NWs	10	~700	[451]
SnO_2@CNT NWs	200	~540	[452]
	100	~900	[454]
Si	10	~3200	[455]
a-Si/c-Si NWs	100	~1000	[460]
a-Si/C NWs	30	~2000	[462]
C @Si NTs	200	~2880	[463]
Ge NWs	20	~1140	[464]

5.3 Photonic and optoelectronic applications of nanowires

II/VI and III/V semiconductors with direct bandgaps are of particular interest for nanophotonics because of their high optoelectronic efficiencies relative to indirect bandgap group IV crystals. Another important feature of these semiconductors is the ability to tune their bandgaps due to quantum confinement effects, allowing the fabrication of different photonic and optoelectronic devices with tuneable optical properties that can differ dramatically to their bulk or thin-layer counterparts. Additionally, the small lateral dimension of the nanostructures allows the growth of almost defect-free single crystals, due to the release of strain on the surface, overcoming

some of the problems associated with the epitaxial growth of 2D heterostructures, such as the generation of structural defects that strongly limit the light emitting action due to non-radiative carrier recombination phenomena.

5.3.1 Nanowire-based LED

Nanowire-based light emitting devices (LED) mimic the device structure of commercially available LEDs, which require the presence of at least one pn-junction. This junction can be realised by either physical contact between different nanowires (crossed-wire approach) [466] or as-grown 1D heterostructures which is described in section 3.8.

The direct growth of radial nanowire heterostructures for LED applications was first described by Haraguchi *et al.* in 1992 [467]. The heterostructure was formed in a gold particle assisted VPE growth procedure by switching the precursor from a disilane/trimethylgallium/arsine mixture (n-type GaAs) to trimethylgallium/trimethylarsine, which incorporates carbon acting as a p-dopant. Spin on glass acted as a spacer before the top-electrode was deposited to ensure the electrical contact to the p-GaAs and the n-GaAs could be contacted through the n^+-GaAs substrate. The current-voltage characteristics of these devices were similar to conventional bulk diodes. Core-shell structures based on GaN nanowire cores and heteroepitaxially grown shells of differently doped GaN, AlGaN and InGaN thin layers have also attracted attention for their use in LED devices [468, 469]. The reported structure allowed the tuning of the emission wavelength between 370 and 580 nm by adjusting the In content in the InGaN quantum well. On chip fabrication of site-specific vertically grown nano LEDs has been described for GaAs and Si substrates with a GaN

nanowire core and InGaP shell [470]. However, the external quantum efficiency in these devices is rather low (8×10−4), which could be attributed to absorbance of the contacts, twinning and surface defects and requires further improvement to solve these growth related issues.

Diodes constructed from crossed junctions of n- and p-type nanowires was first demonstrated by Lieber's group for differently doped nanowires of the same material, such as GaN [202] or InP [466], and combinations of p-Si nanowires and a broad range of n-type nanowires [471]. When forward biased, light emission occurred at the junction between both nanowires, as shown in figure 42. The emission wavelength was dependent on the materials used and therefore a series of different junctions creates multicolor emission, when various n-type nanowire devices were simultaneously addressed by one p-type Si nanowire. Using SOI wafers to etch p-silicon nanowire assemblies and fluid based alignment techniques, scalable fabrication of reliable LED structures have been obtained [471]. The feasibility of the crossed wire approach to fabricate LED devices on flexible surfaces and the robustness of these devices was demonstrated by bending the nanowires diode circuits deposited on polymer substrates [472]. In addition, individual axial heterostructure nanowires with differently doped segments create p-n junctions which can effectively emit photons at the interface region by applying a voltage to both ends, as described for InP [473] and GaN [474] nanowires.

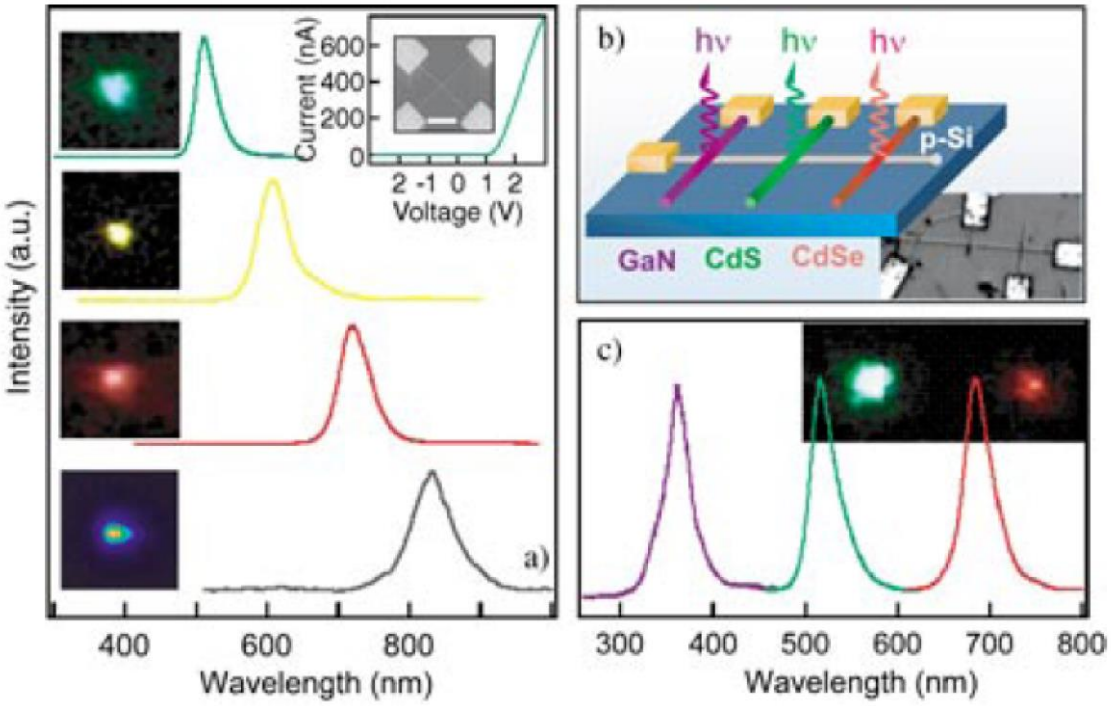

Figure 42. (a) Electroluminescence (EL) spectra from crossed p–n diodes of p-Si and n-CdS, CdSSe, CdSe, and InP, respectively (top to bottom). Insets to the left are the corresponding EL images for CdS, CdSSe, CdSe (all colour CCD), and InP (liquid-nitrogen-cooled CCD) nanoLEDs. The inset top-right shows representative I–V and SEM data recorded for a p-Si/n- CdS crossed nanowire junction (scale bar = 1 mm); (spectra and images were collected at +5 V); (b) schematic and corresponding SEM image of a tricolour nanoLED array. The array was obtained by fluidic assembly and photolithography with 5 mm separation between nanowire emitters; (c) normalised EL spectra and colour images from the three elements. Reprinted from Ref. [471]. Copyright Wiley-VCH Verlag GmbH & Co. KGaA. Reproduced with permission.

ZnO has a large exciton binding energy, which should give rise to high stability, room temperature LEDs, but the difficulty in achieving p-type doping is still an important issue. This issue has been circumvented by a design based on vertically-grown ZnO nanowire/ semiconducting polymer diodes, with a buffer layer of insulating polymer filling the gaps between the nanowires [475]. These devices can act as UV emitting light sources exhibiting a blue shift of the electroluminescence peak of ZnO. Similar devices have been prepared on flexible polyethylene terephthalate polymer substrates resulting in bendable LEDs, whose performance is most certainly limited by a thin layer of the spacer polymer [476]. The characteristics of this configuration was an

excitonic luminescence around 380 nm accompanied by a broader defect-related band covering all of the visible range [477].

Large numbers of axial heterostructered multi-quantum-well nanorods such as GaN/InGaN on conducting substrates have been grown via MOVPE for LED applications [478]. Filling the space between them by spin on glass and a contact on the upper end, with a preferably transparent electrode, results in high brightness and high efficiency LEDs, which are superior to common broad area devices. Similar structures can be observed by RIE etching from planar 2D heterostructured films which can take advantage of well established growth techniques of the semiconductor industry [479].

Another Si technology compatible approach for the fabrication of LEDs is based on single-step self-masked dry etching of a p-type Si wafer and PLD deposition of a thin n-type ZnO layer and an ITO top electrode [480]. The devices have lower turn on voltages and show stronger electroluminescence in the infrared region than their film counterparts. A modified approach giving rise to the fabrication of lateral Si/ZnO p-n junctions has been recently proposed [481, 482]. The method consists of dispersing n-type doped ZnO nanowires on a p-type silicon conducting substrate, forming in this way the lateral p-n junction (figure 43). Covering the silicon, but not the nanowires, with an isolating layer and patterning metal electrodes on the top completes the diode fabrication process. This flexible fabrication approach represents a simplification when compared to the most usual contact fabrication methodologies and could be combined with assembly techniques as described in section 5 to obtain controlled device orientation. However, ZnO nanowire/Si substrate diodes require a dielectric SiO_2 layer, which results in a sufficient potential energy difference between the components. This barrier makes tunnelling of electrons from the valence band of ZnO into p-Si

energetically possible, which is equivalent to hole injection in the opposite direction. Similar results are observed for GaN nanowires on Si substrates [483, 484].

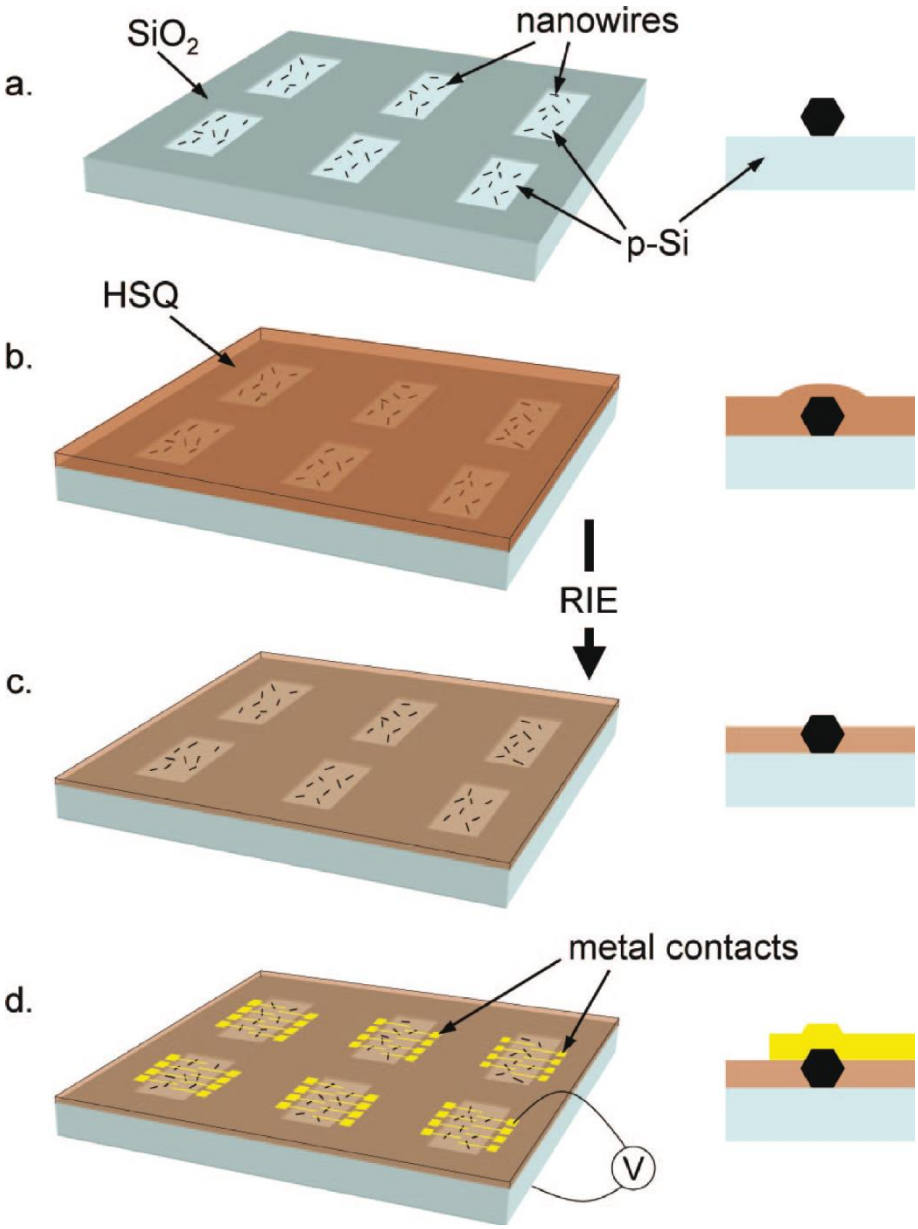

Figure 43. Scalable method for the fabrication of nanowire/substrate photonic and electronic circuits. The schematics illustrate the key steps for the fabrication of p(substrate)-n(nanowire) heterojunction diodes, including (a) deposition of nanowires over the substrate, (b) spin-coating with an isolating layer, (c) RIE of the isolator and (d) deposition of a periodic metal electrode array. Both top and cross-section views are presented. Reprinted from Ref. [481] with permission of ACS Publishers.

5.3.2 Nanowire-based lasers and waveguides

Semiconductor nanowires with refractive index (n>2) are highly attractive materials for the fabrication of semiconducting lasers due to their geometric features. Nanowires owning atomically smooth surface facets can be used both as an active medium and as a Fabry-Perot optical cavity, while its longitudinal axis can serve as the optical waveguide. The end facets of the nanowire serve as the mirrors that limit the optical cavity. Another advantage with nanowires is the expected lower threshold for laser emission than for their thin-film counterparts; however the surface has to be smooth to avoid large losses from surface emission.

Over the last 8 years, lasers constructed from various binary semiconducting materials have been reported, such as ZnO [277, 284], CdS [485] and GaN [486, 487]. These materials emit photons with wavelengths corresponding to the band energies of the semiconductor material. Tuning the emission wavelength of a nanobelt-laser in the range of 340-515 nm and 515-710 nm has been demonstrated by either cation substitution in $Cd_{1-x}Zn_xS$ [488] or anion replacement in $CdS_{1-x}Se_x$ [489], respectively.

In contrast to conventional edge emitting semiconductor lasers where typically the waveguide loss is bigger than the losses at the side facets, in nanowire lasers the much smaller cavity length and the smaller reflection coefficient leads to the opposite phenomenon [490]. The reason for this is that in nanowires with diameters comparable to or smaller than the wavelength of light, diffraction causes the optical field to “spill out” of the nanowire (evanescent field). This contributes to the losses since only the fraction of the optical field inside the nanowire experiences a refractive index contrast at the end facets, thus reducing the amount of reflection. Since the threshold gain is a strong function of the length and diameter of the nanowire it is not surprising that there

are lower limits of the nanowire diameter, where no threshold can be reached as shown for ZnO (<150 nm) [491].

In addition to the pure binary compounds, radial heterostructures of III/V semiconductors have been described to be effective multicolour laser materials where the GaN core acts as the primary part of the optical cavity and the epitaxial InGaN/GaN multi-quantum well shells as the composition-tuneable gain medium (figure 44) [345]. The smooth interfaces between the different layers are consistent with the growth of continuous quantum-well shells on the GaN nanowire core, and are also expected to reduce optical losses at the nanowire–air interface, which is an important factor for reducing threshold in nanowire lasers [492]. However, these photonic nanolasers are in reality submicron laser sources and the realisation of true nanolasers requires revolutionary combination of semiconductor nanowires, such as cadmium sulphide, and metallic surfaces leading to subwavelength plasmonic lasers [493]. The two active components are separated by a small insulating gap to avoid exciton recombination, which would lead to non-radiative quenching and prevent the devices from lasing. The cadmium sulphide acts in these devices as a gain medium and enables lasing using nanowire diameters as low as 52 nm, which is impossible using purely dielectric nanowires that are not forming hybrid plasmons.

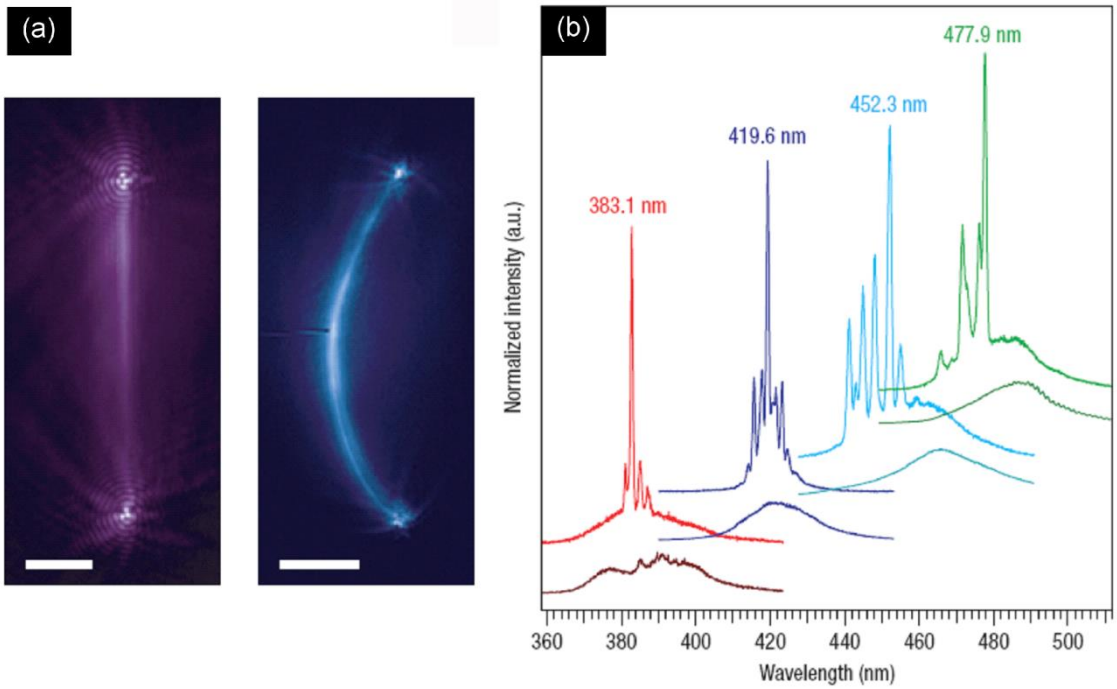

Figure 44. (a) Photoluminescence images (false colour) recorded from GaN/$In_{0.05}Ga_{0.95}N$ (left) and GaN/$In_{0.23}Ga_{0.77}N$ (right) multi-quantum well nanowire structures. Scale bars are 5 μm. (b) Normalised photoluminescence spectra collected from four representative 26 multi-quantum well nanowire structures with increasing In composition pumped at ~250 kW cm^{-2} and ~700 kW cm^{-2}, respectively. Spectra are offset for clarity. Reprinted by permission from Macmillan Publishers Ltd: Nature Materials [345], copyright (2008).

Moreover, 1D semiconductors such as CdS [494] and SnO_2 [495] nanobelts can act as excellent flexible waveguides which makes them important components for future optoelectronic devices. For instance, nanowire-generated photons can be captured and directed to additional components acting as sensors, photodetectors and switches. Similarly to the requirements on laser cavities, the single crystalline nature of the nanobelts, the large refractive index and the smooth surface qualify these 1D nanostructures to act as viable waveguides. These nanostructures can effectively guide the intrinsic photoluminescence as well as photons emitted by other sources. The waveguiding can be simply achieved by focusing laser diodes on the 1D nanostructure or by attachment of light emitting nanostructures [496]. Optical linkages between

photon emitting nanowires, such as GaN and ZnO, and passive nanobelts can be achieved by physical attachment of wires where they can couple via the evanescent field. This arrangement out-performed the end-to-end and crossed-wire configurations because the emission of these subwavelength waveguides is poorly collimated. SnO_2 nanobelts are able to act as multi-laser waveguides, which was demonstrated by the attachment of ZnO and GaN nanowires to one end of the tin oxide nanobelt and recording the output at the other end during simultaneous lasing of the wires as shown in figure 45 [496].

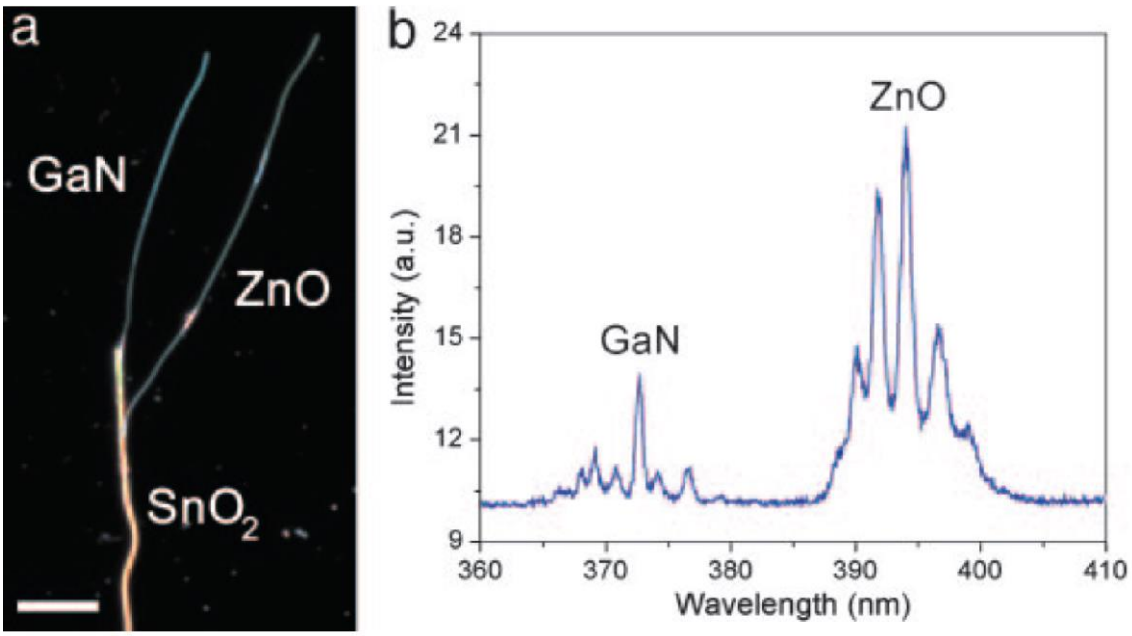

Figure 45. Multilaser waveguiding. (a) Dark-field image of a GaN and a ZnO nanowire coupled to the same nanoribbon. (Scale bar: 10 μm.). (b) Spectrum of guided light collected at the far end of the ribbon when both wires were pumped above their lasing thresholds by the same train of optical pulses. Reprinted from Ref. [496]. Copyright (2005) National Academy of Sciences, U.S.A..

In addition, the selective fluorescence excitation of fluorophores in polystyrene particles attached to waveguides in contrast to particles in the proximity of the waveguide showed that the evanescent field in these structures is located [497].

6. Summary

This article reviews viable approaches for the synthesis of one-dimensional semiconductors and highlights the formation of high aspect-ratio semiconductors. The efforts to understand the fundamental underlying mechanisms for the controlled formation of high quality 1D nanostructures have been tremendous. However, addressing fundamental scientific questions will also lead to both expected and unexpected advances in this field of research.

The improved theoretical support already helped to understand experimental findings, but it should provide further knowledge and support for groups specialised in the material synthesis to predict and explain the results of experimental procedures. However some aspects of the formation of nanowires are not well understood and will require ongoing efforts to gain insight into the underlying mechanisms. In addition to understanding nanowire growth, it will be a challenging task to explore reliable methodologies for the synthesis of 1D nanostructures with diameters below the exciton bohr radius. Moreover, doping of semiconductors to induce further functionalities such as magnetic impurity incorporation in the host matrix, will broaden their potential application portfolio [498]. For these studies one-dimensional semiconductors are perfect model systems, because potential stress can be easily accommodated in these structures, which should prevent phase separation and allow the synthesis of single crystalline materials. In addition, homogeneous and reliable surface functionalisation and novel heterostructures will pave the way to novel applications and devices.

The fundamental properties of 1D nanoscaled semiconductors have been intensively studied for the last decade, leading to progress and fundamental understanding in the

design and performance of novel devices for sensors, solar cells, batteries, lasers etc. We have shown in this review that high aspect ratio semiconductors are reliable materials for a manifold of applications. Nanometre precision synthesis, positioning and interconnection of these building blocks has to be established for the direct integration, or a reliable post assembly process of nanowires, to implement them in well established manufacturing processes. These tasks have to be achieved in order to guarantee a knowledge transfer to an industrial level, in particular the assembly and contact procedure must be optimised to ensure reliable devices at reasonable manufacturing costs. Unfortunately the post-alignment techniques described in Section 4 are still lacking in the transfer of nanowires to non-rigid surfaces and high efficiency transfer to large areas with a controlled nanowire density, which is a key feature for true technology. For fundamental research one has to evaluate the optimum device performance and limits of the materials even in single nanostructure configuration and reveal present flaws requiring further improvement. Even though some of the initial devices presented here show lower performance than state-of-the-art technology the improvement in their implementation could lead to tremendous improvement of their characteristics. However, for commercial use reliable and easy upscaling processes have to be developed. Additionally, the defect density in nanostructures, surface recombination processes, interface effects of heterojunctions (contacts) and effects of diminishing dimensions have to be evaluated to get the best of these amazing materials. Establishing reliable growth techniques to visualise different sections of doped semiconductors and their controlled interfaces (e.g. by kinks) will pave the way to an easier integration of these semiconducting building blocks in devices [499].

References

[1] Weisbuch C, Vinter B. Quantum Semiconductor Structures: Fundamentals and Applications, Boston: Academic Press; 1991.

[2] Hong BH, Bae SC, Lee CW, Jeong S, Kim KS. Science 2001;294:348-51.

[3] Nishizawa M, Menon VP, Martin CR. Science 1995;268:700-2.

[4] Liang CH, Chen LC, Hwang JS, Chen KH, Hung YT, Chen YF. Appl Phys Lett 2002;81:22-4.

[5] Ma RZ, Bando Y, Sato T. Adv Mater 2002;14:366-8.

[6] Patzke GR, Krumeich F, Nesper R. Angew Chem Int Ed 2002;41:2446-61.

[7] Mathur S, Barth S, Werner U, Hernandez-Ramirez F, Romano-Rodriguez A. Adv Mater 2008;20:1550-4.

[8] Pan ZW, Lai HL, Au FCK, Duan XF, Zhou WY, Shi WS, Wang N, Lee CS, Wong NB, Lee ST, Xie SS. Adv Mater 2000;12:1186-90.

[9] Ho GW, Wong ASW, Wee ATS, Welland ME. Nano Lett 2004;4:2023-6.

[10] Li QG, Penner RM. Nano Lett 2005;5:1720-5.

[11] Mao GZ, Dong WF, Kurth DG, Mohwald H. Nano Lett 2004;4:249-52.

[12] Ziemelis K. Nature 2000;406:1021.

[13] Hayden O, Agarwal R, Lieber CM. Nature Mater 2006;5:352-6.

[14] Zhang ZB, Ying JY, Dresselhaus MS. J Mater Res 1998;13:1745-8.

[15] Ohnishi H, Kondo Y, Takayanagi K. Nature 1998;395:780-783.

[16] Chem CQ, Shi Y, Zhang YS, Zhu J, Yan YJ. Phys Rev Lett 2006;96:075505.

[17] Ngo LT, Almecija D, Sader JE, Daly B, Petkov N, Holmes JD, Erts D, Boland JJ. Nano Lett 2006;6:2964-8.

[18] Barth S, Harnagea C, Mathur S, Rosei F. Nanotechnology 2008;20:115705.

[19] Hernandez-Ramirez F, Prades JD, Liminez-Diaz R, Casals O, Cirera A, Romano-Rodriguez A, Morante JR, Barth S, Mathur S. Fabrication of Electrical Contacts on Individual Metal Oxide Nanowires and Novel Device Architectures, In: DixonCJ, Curtines OW, editors. Nanotechnology: Nanofabrication, Patterning, and Self Assembly, Nova Science Publishers, 2009.

[20] Vayssieres L, Beermann N, Lindquist SE, Hagfeld A. Chem Mater 2001;13:233-5.

[21] Gates B, Mayers B, Cattle B, Xia YN. Adv Funct Mater 2002;12:219-27.

[22] Gates B, Yin Y, Xia YN. J Am Chem Soc 2000;122:12582-3.

[23] Gates B, Mayers B, Grossman A, Xia YN. Adv Mater 2002;14:1749-52.

[24] Puntes VF, Krishnan KM, Alivisatos AP. Science 2001;5511:2115-7.

[25] Jun YW, Jung YY, Cheon J. J Am Chem Soc 2002;124:615-9.

[26] Greene LE, Law M, Goldberger J, Kim F, Johnson JC, Zhang YF, Saykally RJ, Yang PD. Angew Chem Int Ed 2003;42:3031-4.

[27] Cheng C, Yu KF, Cai Y, Fung KK, Wang N. J Phys Chem C 2007;111:16712-6.

[28] Burton WK, Cabrera N, Frank FC. Nature 1949, 163, 398-9.

[29] Sears GW. Acta Metallurgica 1955;3:361-6.

[30] Dai ZR, Pan ZW, Wang ZL. Adv Funct Mater 2003;13:9-24.

[31] Wang ZL, Kong XY, Zou JM. Phys Rev Lett 2003;91:185502.

[32] Hughes WL, Wang ZL. J Am Chem Soc 2004;126:6703-9.

[33] Kong XY, Wang ZL. Nano Lett 2003;3:1625-31.

[34] Zhang RQ, Lifshitz Y, Lee ST. Adv Mater 2003;15:635-40.

[35] Li CP, Lee CS, Ma XL, Wang N, Zhang RQ, Lee ST. Adv Mater 2003;15:607-9.

[36] Zhang YF, Tang YH, Wang N, Lee CS, Bello I, Lee ST. Phys Rev B 2000;61:4518-21.

[37] Shi WS, Zheng YF,Wang N, Lee ST. Appl Phys Lett 2001;78:3304-6.

[38] Wang N, Tang YH, Zhang YF, Lee CS, Lee ST. Phys Rev B 1998;58:16024-6.

[39] Kim BS, Koo TW, Lee JH, Kim DS, Jung YC, Hwang SW, Choi BL, Lee EK, Kim JM, Whang D. Nano Lett 2009;9:864-9.[40] Wagner RS, Ellis WC. Appl Phys Lett 1964;4:89-90.

[41] Givargizov EI. J Cryst Growth 1975;31:20-30.

[42] Wagner RS. VLS mechanism of crystal growth. In: Levitt AP, editor. Whisker Technology,New York: Wiley-Interscience;1970, p. 47-119.

[43] Kodambaka S, Tersoff J, Reuter MC, Ross FM. Phys Rev Lett 2006;96:096105.

[44] Verheijen MA, Immink G, De Smet T, Borgstrom MT, Bakkers EPAM. J Am Chem Soc 2006;128:1353-9.

[45] Schubert L, Werner P, Zakharov ND, Gerth G, Kolb FM, Long L, Gosele U, Tan TY. Appl Phys Lett 2004:84:4968-70.

[46] Cornet DM, Mazzetti VGM, Lapierre RR. Appl Phys Lett 2007;90:013116.

[47] Aagesen M, Johnson E, Sorensen CB, Mariager SO, Feidenhans R, Spiecker E, Nygard J, Lindelof PE. Nature Nanotech 2007;2:761-4.

[48] Stringfellow GB. Organometallic vapor-phase epitaxy: theory and practice. London: Academic Press, 1989.

[49] Jensen LE, Bjork MT, Jeppesen S, Persson AI, Ohlsson BJ, Samuelson L. Nano Lett 2004;4:1961-4.

[50] Borgstrom MT, Immink G, Ketelaars B, Algra R, Bakkers EPAM. Nature. Nanotechn 2007;2:541-4.

[51] Persson AI, Froberg LE, Jeppesen S, Bjork MT, Samuelson L. Appl Phys Lett 2007;101:034313.

[52] Kim Y, Joyce HJ, Gao O, Tan HH, Jagadish C, Paladugu M, Zou J, Suvorova AA. Nano Lett 2006;6:599-604.

[53] Dubrovskii VG, Cirlin GE, Soshnikov IP, Tonkikh AA, Sibirev NV, Samsonenko YB, Ustinov VM. Phys Rev B 2005;71:205325.

[54] Clark TE, Nimmatoori P, Lew KK, Pan L, Redwing JM, Dickey EC. Nano Lett 2008;8:1246-52.

[55] Algra RE, Verheijen MA, Borgstrom MT, Feiner LF, Immink G, Van Enckevort WJP, Vlieg E, Backers EPAM. Nature 2008;456:369-72.

[56] Persson AI, Larsson MW, Stenstrom S, Ohlsson BJ, Samuelson L, Wallenberg LR. Nature Mater 2004;3:677-81.

[57] Nebol'sin VA, Shchetinin AA. Inorg Mater 2003;39:899-902.

[58] Glas F, Harmand JC, Patriarche G. Phys Rev Lett 2007;99:146101.

[59] Dick KA, Kodambaka S, Reuter MC, Deppert K, Samuelson L, Seifert W, Ross FM. Nano Lett 2007;7:1817-22.

[60] Cheyssac P, Sacilotti M, Patriarche G. J Appl Phys 2006;100:044315.

[61] Dubrovskii VG, Sibirev NV, Harmand JC, Glas F. Phys Rev B 2008;78:235301.

[62] Givargizov EI, Chernov AA. Kristallografiya 1973;18:147-53.

[63] Baron T, Gordon M, Dhalluin F, Ternon C, Ferret P, Gentile P. Appl Phys Lett 2006;89:233111.

[64] Arbiol J, Kalache B, Cabarrocas PRI, Morante JR, Morral AFI. Nanotechnology 2007;18:305606.

[65] Kamins TI, Li X, Williams RS, Liu X. Nano Lett 2004;4:503-6.

[66] Adhikari H, Marshall AF, Chidsey CED, McIntyre PC. Nano Lett 2006;6:318-23.

[67] Wang GT, Talin AA, Werder DJ, Creighton JR, Lai E, Anderson RJ, Arslan I. Nanotechnology 2006;17:5773-80.

[68] Kirkham M, Wang XD, Wang ZL, Snyder RL. Nanotechnology 2007;18:365304.

[69] Regolin I, Khorenko V, Prost W, Tegude FJ, Sudfeld D, Kastner J, Dumpich G, Hitzbleck K, Wiggers H. J Appl Phys 2007;101:054318.

[70] Kodambaka S, Tersoff J, Reuter MC, Ross FM. Science 2007;316:729-32.

[71] Hannon JB, Kodambaka S, Ross FM, Tromp RM. Nature 2006;440:69-71.

[72] den Hertog MI, Rouviere JL, Dhalluin F, Desre PJ, Gentile P, Ferret P, Oehler F, Baron T. Nano Lett 2008;8:1544-50.

[73] Kodambaka S, Hannon JB, Tromp RM, Ross FM. Nano Lett 2006;6:1292-6.

[74] Kawashima T, Mizutani T, Nakagawa T, Torii H, Saitoh T, Komori K, Fujii M. Nano Lett 2008;8:362-8.

[75] Wiethoff C, Ross FM, Copel M, Horn-von Hoegen M, Meyer zu Heringdorf FJ Nano Lett 2008;8:3065-8.

[76] Barth S, Estrade S, Hernandez-Ramirez F, Peiro F, Arbiol J, Romano-Rodriguez A, Mathur S. Cryst Growth Design 2009;9:1077-81.

[77] Allen JE, Hemesath ER, Perera DE, Lensch-Falk JL, Li ZY, Yin F, Gass MH, Wang P, Bleloch AL, Palmer RE, Lauhon LJ. Nature Nanotechn 2008;3:168-73.

[78] Huang SM, Cai QR, Chen JY, Qian Y, Zhang LJ. J Am Chem Soc 2009;131:294-5.

[79] Takagi D, Kobayashi Y, Homma Y. J Am Chem Soc 2009;131:6922-3.]

[80] Li Z, Larsson JA, Larsson P, Ahuja R, Tobin JM, O'Byrne J, Morris MA, Attard G, Holmes JD. J Phys Chem C 2008;112:12201-6.

[81] Trentler TJ, Hickman, KM, Goel SC, Viano AM, Gibbons PC, Buhro WE. Science 1995;270:1791-4.

[82] Holmes JD, Johnston KP, Doty RC, Korgel BA. Science 2000;207:1471-3.

[83] Sun JW, Buhro WE. Angew Chem Int Ed 2008;47:3215-8.

[84] Tuan HY, Lee DC, Korgel BA. Angew Chem Int Ed 2006;45:5184-7.

[85] Tuan HY, Lee DC, Hanrath T, Korgel BA. Nano Lett 2005;5:681-4.

[86] Tuan HY, Lee DC, Hanrath T, Korgel BA. Chem Mater 2005:17:5705-11.

[87] Zhao LL, Yosef M, Steinhart M, Goring P, Hofmeister H, Gosele U, Schlecht S. Angew Chem Int Ed 2006;45:311-315.

[88] Brumlik CJ, Martin CR. J Am Chem Soc 1991;113:3174-5.

[89] Zheng MJ, Zhang LD, Li GH, Shen WZ. Chem Phys Lett 2002;363:123-8.

[90] Martin CR, Nishizawa M, Jirage K, Kang M. J Phys Chem B 2001;105:1925-34.

[91] Yu SF, Li NC, Wharton J, Martin CR. Nano Lett 2003;3:815-8.

[92] Bachmann J, Jing J, Knez M, Barth S, Shen H, Mathur S, Gosele U, Nielsch K. J Am Chem Soc 2007;129:9554-5.

[93] Zhang Z, Gekhtman D, Dresselhaus MS, Ying JY. Chem Mater 1999;11:1659-65.

[94] Erts D, Polyakov B, Daly B, Morris M A, Ellingboe S, Boland J, Holmes J D. J Phys Chem B 2006;110:820-6.

[95] Redmond G, Bein T, Morris MA, Holmes JD. Chem Phys Chem 2007;8:235-40.

[96] Lew KK, Redwing JM. J Cryst Growth 2003;254:14-22.

[97] Bogart TE, Dey S, Lew KK, Mohney SE, Redwing JM. Adv Mater 2005;17:114-7.

[98] Petkov N, Birjukovs P, Phelan R, Morris MA, Erts D, Holmes JD. Chem Mater 2008;20:1902-8.

[99] Zhang Y, Dai HJ. Appl Phys Lett 2000;77:3015-7.

[100] Fan HJ, Knez M, Scholz R, Nielsch K, Pippel E, Hesse D, Zacharias M, Gosele U. Nature Mater 200;5:627-31.

[101] Li M, Schnablegger H, Mann S. Nature 1999;402:393-5.

[102] Hopwood JD, Mann S. Chem Mater 1997;9:1819-28.

[103] Li M, Mann S. Adv Funct Mater 2002;12:773-9.

[104] Filankembo A, Pileni MP. J Phys Chem B 2000;104:5865-8.

[105] Tanori J, Pileni MP. Adv Mater 1995;7:862-4.

[106] Pileni MP. Nature Mater 2003;2:145-50.

[107] Bose GM. Recherches sur la cause et sur la Véritable théorie de l'électricité. Wittenberg. 1745.

[108] Lord Rayleigh. Philos Mag 1882;14:184-6.

[109] Li D, Xia YN. Nano Lett 2003;3:555-60.

[110] Bashouti M, Salalha W, Brumer M, Zussman E, Lifshitz E. Chem Phys Chem 2006;7:102-6.

[111] Li D, Wang YL, Xia YN. Nano Lett 2003;3:1167-71.

[112] Li D, Ouyang G, McCann JT, Xia YN. Nano Lett 2005;5:913-6.

[113] Li D, Xia YN. Nano Lett 2004;4:933-8.

[114] Sun ZC, Zussman E, Yarin AL, Wendorff JH, Greiner A. Adv Mater 2003;15:1929-32.

[115] Li D, McCann JT, Xia YN. Small 2005;1:83-6.

[116] Melosh NA, Boukai A, Diana F, Gerardot B, Baldato A, Petroff PM, Heath JR. Science 2003;300:112-5.

[117] Edelstein AS, Cammarata RC. Nanomaterials: Synthesis, Properties and Applications, 2nd Ed. Institute of Physics Publishing, 1998.

[118] Sun YG, Khang DY, Hua F, Hurley K, Nuzzo RG, Rogers JA. Adv Funct Mater 2005;15:30-40.

[119] Sun Y, Rogers JA. Nano Lett 2004;4:1953-9.

[120] Peng KQ, Yan YJ, Gao SP, Zhu J. Adv Mater 2002;14:1164-7.

[121] Peng KQ, Huang ZP, Zhu J. Adv Mater 2004;16:73-6.

[122] Bootsma GA, Gassen HJ. J Cryst Growth 1971;10:223-34.

[123] Wu Y, Cui Y, Huynh L, Barrelet CJ, Bell DC, Lieber CM. Nano Lett 2004;4:433-6.

[124] Givargizov EI, Sheftal NN. J Cryst Growth 1971;9:326-9.

[125] Zhang YJ, Zhang Q, Wang NL, Yan YJ, Zhou HH, Zhu J. J Cryst Growth 2001;226:185-91.

[126] Hofmann S, Ducati C, Neill RJ, Piscanec S, Ferrari AC, Geng J, Dunin-Borkowski RE, Robertson J. J Appl Phys 2003;94:6005-12.

[127] Park WI, Zheng GF, Jiang XC, Tian BZ, Lieber CM. Nano Lett 2008;8:3004-8.

[128] Lincoln YC, Lauhon J, Gudiksen MS, Wang J, Lieber CM. Appl Phys Lett 2001;78:2214-6.

[129] Lombardi I, Hochbaum AI, Yang P, Carro C, Maboudian R. Chem Mater 2006;18:988-91.

[130] Westwater J, Gosain DP, Tomiya S, Usui S, Ruda H. J Vac Sci Technol B 1997;15:554-7.

[131] Wu Y, Fan R, Yang P. Nano Lett 2002;2:83-6.

[132] Lauhon LL, Gudiksen MS, Wang D, Lieber CM. Nature 2002;420:57-61.

[133] Cui Y, Duan X, Hu J, Lieber CM. J Phys Chem B 2000;104:5213-6.

[134] Sunkara MK, Sharma S, Miranda R, Lian G, Dickey EC. Appl Phys Lett 2001; 79:1546-8.

[135] KaminsTI, Williams RS, Basile DP, Hesjedal T, Harris JS. J Appl Phys 2001;89:1008-16.

[136] Jeon M, Uchiyama H, Kamisako K. Mater Lett 2009;63:246-48.

[137] Schmidt V, Senz S, Gosele U. Z Metallkd 2005;96:427-8.

[138] Wang YW, Schmidt V, Senz S, Gosele U. Nature Nanotechn 2006;3:186-9.

[139] Yu JY, Chung SW, Heath JR. J Phys Chem B 2000;104:11864-70.

[140] Schmidt V, Senz S, Gosele U. Nano Lett 2005;5:931-5.

[141] Garnett EC, Liang WJ, Yang PD. Adv Mater 2007;19:2946-50.

[142] Shimizu T, Xie T, Nishikawa T, Shingubara S, Senz S, Gosele U. Adv Mater 2007;19:917-20.

[143] Morral AFI, Arbiol J, Prades JD, Cirera A, Morante JR. Adv Mater 2007;19:1347-51.

[144] Wei DP, Chen Q. J Phys Chem C 2008;112:15129-33.

[145] Morales AM, Lieber CM. Science 1998;279:208-11.

[146] Zhang YF, Tang YH, Wang N, Yu DP, Lee CS, Bello I, Lee ST. Appl Phys Lett 1998;72:1835-7.

[147] Liu JL, Cai SJ, Jin GL, Thomas SG, Wang KL. J Cryst Growth 1999;200:106-11.

[148] FuhrmannB, Leipner HS, Höche HR, Schubert L, Werner P, Gosele U. Nano Lett 2005;5:2524-7.

[149] Feng SQ, Yu DP, Zhang HZ, Bai ZG, Ding Y. J Cryst Growth 2000;209:513-7.

[150] Sivakov V, Heyroth F, Falk F, Andra G, Christiansen S. J Cryst Growth 2007;300:288-93.

[151] Sivakov V, Andra G, Hincinschi C, Gosele U, Zahn DRT, Christiansen S. Appl Phys A 2006;85:311-5.

[152] Kolb FM, Hofmeister H, Scholz R, Zacharias M, Gosele U, Ma DD, Lee ST. J Electrochem Soc 2004;151:G472-5.

[153] Zhang YF, Tang YF, Wang N, Lee CS, Bello I, Lee ST. J Cryst Growth 1999;197:136-40.

[154] Wang N, Tang YH, Zhang YF, Lee CS, Bello I, Lee ST. Chem Phys Lett 1999;299:237-42.

[155] Shi WS, Peng HY, Zheng YF, Wang N, Shang NG, Pan ZW, Lee CS, Lee ST. Adv Mater 2000;12:1343-5.

[156] Shi W, Peng H, Wang N, Li CP, Xu L, Lee CS, Kalish R, Lee ST. J Am Chem Soc 2001;123:11095-6

[157] Coleman NRB, Morris MA, Spalding TR, Holmes JD. J Am Chem Soc 2001;123:187-8.

[158] Mallet J, Molinari M, Martineau F, Delavoie F, Fricoteaux P, Troyon M. Nano Lett 2008;8:3468-74.

[159] Al-Salman R, Mallet J, Molinari M, Fricoteaux P, Martineau F, Troyon M, Zein El Abedin S, Endres F. Phys Chem Chem Phys 2008;10:6233-7.

[160] Coleman NRB, O'Sullivan N, Ryan KM, Crowley TA, Morris MA, Spalding TR, Steytler DC, Holmes JD. J Am Chem Soc 2001;123:7010-6.

[161] Lyons DM, Ryan KM, Morris MA, Holmes JD. Nano Lett 2002;2:811-6.

[162] Hu J, Bando Y, Liu Z, Zhan J, Golberg D, Sekiguchi T. Angew Chem Int Ed 2004;43:63-6.

[163] Heitsch AT, Fanfair DD, Tuan HY, Korgel BA. J Am Chem Soc 2008;130:5436-7.

[164] Shah PS, Hanrath T, Johnston KP, Korgel BA. J Phys Chem B 2004;108:9574-87.

[165] Hanrath T, Korgel BA. Adv Mater 2003;15:437-40.

[166] Peng KQ, Xu Y, Wu Y, Yan Y, Lee ST, Zhu J. Small 2005;1:1062-7.

[167] Huang ZP, Zhang XX, Reiche M, Liu, L, Lee W, Shimizu T, Senz S, Gosele U. Nano Lett 2008;8:3046-51.

[168] Huang ZP, Fang H, Zhu J. Adv Mater 2007;19:744-8.

[169] Peng KQ,. Zhang ML, Lu AJ, Wong NB, Zhang R, Lee ST. Appl Phys Lett 2007;90:163123.

[170] Juhasz R, Elfstrom N, Linnros J. Nano Lett 2005;5:275-80.

[171] Beckman RA, Johnston-Halperin E, Melosh NA, Luo Y, Green JE, Heath JR. J Appl Phys 2004;96:5921-3.

[172] Ko HC, Baca AJ, Rogers JA. Nano Lett 2006;6:2318-24.

[173] Elfstrom N, Karlstrom AE, Linnros J. Nano Lett 2008;8:945-9.

[174] Miyamoto Y, Hirata M. Japan J Appl Phys 1975;14: 1419-20.

[175] Wu YY, Yang PD. Chem Mater 2000;12:605-7.

[176] Woodruff JH, Ratchford JB, Goldthorpe IA, McIntyre PC, Chidsey CED. Nano Lett 2007;7:1637-42.

[177] Yu B, Sun XH, Calebotta GA, Dholakia GR, Meyyappan M. J Clust Sci 2006;17:579-97.

[178] Mathur S, Shen H, Sivakov V, Werner U. Chem Mater 2004;16:2449-56.

[179] Mathur S, Barth S. Z Phys Chem 2008;222:307-17.

[180] Lew KK, Pan L, Dickey EC, Redwing JM. Adv Mater 2003;15:2073-6.

[181] Greytak AB, Lauhon LJ, Gudiksen MS, Lieber CM. Appl Phys Lett 2004;84:4176-8.

[182] Wang D, Dai H. Angew. Chem. Int. Ed., 2002, 41, 4783-6.

[183] Jin CD, Yang JE, Jo MH. Appl Phys Lett 2006;88:193105.

[184] Zhang R, Tu R, Dai H. Nano Lett 2006;6:2785-9.

[185] Nguyen P, Ng HT, Meyyappan. Adv Mater

[186] Gu G, Burghard M, Kim GT, Duesberg GS, Cihiu PW, Krstic V, Han WQ. J Appl Phys 2001;90:5747-51.

[187] Wu YY, Yang PD. J Am Chem Soc 2001;123:3165-6.

[188] Sun XH, Didychuk C, Sham TK, Wong NB. Nanotechnology 2006;17:2925-30.

[189] Sutter E, Ozturk B, Sutter P. Nanotechnology 2008;19:435607.

[190] Ryan KM, Erts D, Olin H, Morris MA, Holmes JD. J Am Chem Soc 2003;125:6284-8.

[191] Heath JR, LeGoues FK. Chem Phys Lett 1993;208: 63-8.

[192] Hanrath T, Korgel BA. J Am Chem Soc 2002;124:1424-9.

[193] Gerung H, Boyle TJ, Tribby LJ, Bunge SD, Brinker CJ, Han SM. J Am Chem Soc 2006;128:5244-50.

[194] Chockla AM, Korgel BA. J Mater Chem 2009;19:996-1001.

[195] Lu X, Fanfair DD, Johnston KP, Korgel BA. J Am Chem Soc 2005;127:15718-9.

[196] Hanrath T, Korgel BA. Small 2005;1:717-21.

[197] Fang C, Foll H, Carstensen J. Nano Lett 2006;6:1578-80.

[198] Chen CC, Yeh CC, Chen CH, Yu MY, Liu HL, Wu JJ, Chen KH, Chen LC,. Peng JY, Chen YF. J Am Chem Soc 2001;123:2791-98.

[199] Chen X, Xu J, Wang RM, Yu D. Adv Mater 2003;15:419-21.

[200] Peng HY, Wang N, Zhou XT, Zheng YF, Lee CS, Lee ST. Chem Phys Lett 2002;359:241-45.

[201] Chang KW, Wu JJ. J Phys Chem B 2002;106:7796-9.

[202] Zhong ZH, Qian F, Wang DL, Lieber CM. Nano Lett 2003;3:343-6.

[203] Kuykendall T, Pauzauskie P, Lee S, Zhang Y, Goldberger J, Yang P. Nano Lett 2003;3:1063-6.

[204] Kuykendall T, Pauzauskie PJ, Zhang YF, Goldberger J, Sirbuly D, Denlinger J, Yang PD. Nature Mater 2004;3:524-8.

[205] He M, Minus I, Zhou P, Mohammed SN, Halpern J, Jacobs R, Sarney WL, Salamanca-Riba L, Vispute RD. Appl Phys Lett 2000;77:3731-3.

[206] Yoo J, Hong YL, An SJ, Yi GC, Chon B, Yoo T, Kim JW, Lee JS. Appl Phys Lett 2006;89:043124.

[207] Chen CC, Yeh CC. Adv Mater 2000;12:738-41.

[208] Ha B, Kim HC, Kang SG, Kim YH, Lee JY, Park CY, Lee CJ. Chem Mater 2005;17:5398-403.

[209] Bae SY, Seo HW, Park J, Yang H, Kim H, Kim S. Appl Phys Lett 2003;82:4564-6.

[210] Qian F, Li Y, Gradecak S, Wang D, Barrelet CJ, Lieber CM. Nano Lett 2004;4:1975-9.

[211] Oh E, Choi JH, Seong HK, Choi HJ. Appl Phys Lett 2006;89:092109.

[212] Bae SY, Seo HW, Park J, Yang H, Park JC, Kim S. Appl Phys Lett 2002;81:126-8.

[213] Xu B, Yang D, Wang F, Liang J, MA S, Liu X. Appl Phys Lett 2006;89:074106.

[214] Duan X, Lieber CM. J Am Chem Soc 2000;122:188-9.

[215] Shi W, Zheng Y, Wang N, Lee CS, Lee ST. Adv Mater 2001;13:591-4.

[216] Shi WS, Zheng YF, Wang N, Lee CS, Lee ST. Chem Phys Lett 2001;345:377-80.

[217] Huang Y, Duan X, Cui Y, Lieber CM. Nano Lett 2002;2:101-4.

[218] Zhang J, Zhang LD, Wang XF, Liang CH, Peng XS, Wang YW. J Chem Phys 2001;115:5714-7.

[219] Cheng GS, Zhang LD, Zhu Y, Fei GT, Li L, Mo CM, Mao YQ. Appl Phys Lett 1999;75:2455-7.

[220] Jung WG, Jung SH, Kung P, Razeghi M. Nanotechnology 2006;17:54-9.

[221] Goldberger J, He RR, Zhang YF, Lee SW, Yan HQ, Choi HJ, Yang PD. Nature 2003;422:599-602.

[222] Youtsey C, Romano LT, Adesia I. Appl Phys Lett 1998;73:797-9.

[223] Lee KJ, Lee J, Hwang H, Reitmeier ZJ, Davis RF, Rogers JA, Nuzzo RG. Small 2005;1:1164-8.

[224] Hiruma K, Katsuyama T, Ogawa K, Koguchi M, Kakibashi H, Morgan GP. Appl Phys Lett 1991;59:431-3.

[225] Hiruma K, Yazawa M, Haraguchi K, Ogawa K, Katsuyama T, Koguchi M, Kakibayashi H. J Appl Phys 1993;74:3162-71

[226] Joyce HJ, Gao Q, Tan HH, Jagadish C, Kim Y, Fickenscher MA, Perera S, Hoang TB, Smith LM, Jackson HE, Yarrison-Rice JM, Zhang X, Zou J. Nano Lett 2009;9:695-701.

[227] Noborisaka J, Motohisa J, Fukui T. Appl Phys Lett 2005;86: 213102.

[228] SeifertW, Bergstroem M, Deppert K, Dick KA, Johansson J, Larsson MW, Martensson T, Skoeld N, Svensson CPT, Wacaser BA, Wallenberg LR, Samuelson L. J Cryst Growth 2004;272:211-20.

[229] Samuelson L, Thelander C, Bjoerk MT, Bergstroem M, Deppert K, Dick KA, Hansen AE, Martensson T, Panev N, Persson AI, Seifert W, Skoeld N, Larsson MW, Wallenberg LR. Physica E 2004;25:313-8.

[230] Duan X, Lieber CM. Adv Mater 2000;12:298-302.

[231] Morkoc H, Stamberg R, Krikorian E. J J Appl Phys 1982;21:L230-2.

[232] Colombo C, Spirkoska, D, Frimmer M, Abstreiter G, Morral AFI. Phys Rev B 2008;77:155326.

[233] Martelli F, Rubini S, Piccin M, Bais G, Tchernycheva M, Patriarche G, Travers L, Glas F, Cirlin G. J Cryst Growth 2007;301:853-6.

[234] Davidson III FM, Schricker AD, Wiaceck RJ, Korgel BA. Adv Mater 2004;16: 646-9.

[235] Yu H, Buhro WE. Adv Mater 2003;15: 416-9.

[236] Sun YG, Kim HS, Menard E, Kim S, Adesida I, Rogers JA. Small 2006;2:1330-4.

[237] Sun YG, Graff RA, Strano MS, Rogers JA. Small 2005;1:1052-7.

[238] Sun YG, Kim S, Adesida I, Rogers JA. Appl Phys Lett 2005;87:083501.

[239] Barrelet CJ, Wu Y, Bell DC, Lieber CM. J Am Chem Soc 2003;125:11496-7.

[240] Hsu YJ, Lu SY. Appl Phys A 2005;81:573-8.

[241] Ge J, Li Y. Adv Funct Mater 2004;14:157-62

[242] Lin YF, Hsu YJ, Lu SY, Kung SC. Chem Comm 2006:2391-3.

[243] Wang Y, Meng G, Zhang L, C. Liang C, Zhang J. Chem Mater 2002;14:1773-7.

[244] Kar S, Satpati B, Satyam PV, Chaudhuri S. J Phys Chem B 2005;109:19134-8.

[245] Ye C, Meng G, Wang Y, Jiang Z, Zhang L. J Phys Chem B 2002;106:10338-41.

[246] Wu XC, Tao YR. J Cryst Growth 2002;242:309-12.

[247] Liu W, Jia C, Jin C, Yao L, Cai W, Li X. J Cryst Growth 2004;269:304.

[248] Gao T, Wang T. J Phys Chem B 2004;108:20045-9.

[249] Kar S, Chaudhuri S. J Phys Chem B 2006;110:4542.

[250] Wang ZQ, Gong JF, Duan JH, Huang HB, Yang SG, Zhao XN, Zhang R, Du YW. Appl Phys Lett 2006;89:033102.

[251] Pan A, Liu D, Liu R, Wang F, Zhu X, Zou B. Small 2005;1:980-3.

[252] Zhou XT, Kim PSG, Sham TK, Lee ST. J Appl Phys 2005;98:024312.

[253] Zhang J, Jiang F, Zhang L. J Phys Chem B 2004;108:7002-5.

[254] Liu W, Jin C, Jia C, Yao L, Cai W, Li X. Chem Lett 2004;33:228-9.

[255] Dong L, Jiao J, Coulter M, Love L. Chem Phys Lett 2003;376:653-8.

[256] Routkevich D, Bigioni T, Moskovits M, Xu JM. J Phys Chem 1996;100:14037-7.

[257] Xu D, Xu Y, Chen D, Guo G, Gui L, Tang Y. Adv Mater 2000;12:520-2.

[258] Cao H, Xu Y, Hong J, Liu H, Yin G, Li B, Tie C, Xu Z. Adv Mater 2001;13:121-3.

[259] Li Y, Xu DS, Zhang QM, Chen DP, Huang FZ, Xu YJ, Guo GL, Gu ZN. Chem Mater 1999;11:3433-5.

[260] Petkov N, Xu J, Morris MA, Holmes JD. J Phys Chem C 2008;112:7345-55.

[261] Shen XP, Yuan AH, Wang F, Hong JM, Xu Z. Solid State Commun 2005;133:19-22.

[262] Cao H, Xu Y, Hong J, Liu H, Yin G, Li B, Tie C, Xu Z. Adv Mater 2001;13:121-3.

[263] Cao BL, Jiang Y, Wang C, Wang WH, Wang LZ, Niu M, Zhang WJ, Li YQ, Lee ST. 2007;17:1501-6.

[264] Yan P, Xie Y, Qian YT, Liu XM. Chem Commun 1999;1293-4.

[265] Rao CNR, Govindaraj A, Deepak FL, Gunari NA, Nath M. Appl Phys Lett 2001;78:1853-5.

[266] Wu J, Jiang Y, Li Q, Liu X, Qiiang Y. J Cryst Growth 2002;235:421-4.

[267] Liu HB, Li YL, Luo HY, Fang HJ, Li HM, Xiao SQ, Shi SQ, Xiao SX, Zhu DB. Eur Phys D 2003;24:405-8.

[268] Chen M, Xie Y, Lu J, Xioung Y, Zhang S, Qiang Y, Liu X. J Mater Chem 2002;12:748-53.

[269] Park WI, Kim DH, Jung SW, Yi GC. Appl Phys Lett 2002;80:4232-4.

[270] Park WI, Yi GC. Adv Mater 2004;16:87-90.

[271] Ho ST, Chen KC, Chen HA, Lin HY, Cheng CY, Lin HN. Chem Mater 2007;19:4083-86.

[272] Baxter JB, Aydil ES. Appl Phys Lett 2005;86:053114.

[273] Tseng YK, Chia CT, Tsay CY, Lin LJ, Cheng HM, Kwo CY, Chen IC. J Electrochem Soc 2005;152:G95-8.

[274] Zhang Y, Russo RE, Mao SS. Appl Phys Lett 2005;87:133115.

[275] Zuniga-Perez J, Rahm A, Czekalla C, Lenzner J, Lorenz M, Grundmann M. Nanotechnology 2007;18:195303.

[276] Heo YW, Varadarajan V, Kaufman M, Kim K, Norton DP, Ren F, Fleming PH. Appl Phys Lett 2002;81:3046-8.

[277] Wang ZL. Adv Mater 2003;15:432-6.

[278] Pan ZW, Dai ZR, Wang ZL. Science 2001;291:1947-9.

[279] Wang ZL, Kong YY, Ding Y, Gao P, Hughes WL, Yang R, Zhang Y. Adv Funct Mater 2004;14:943-56.

[280] Kong XY, Ding Y, Yang RS, Wang ZL. Science 2004;303:1348-51.

[281] Gao PX, Ding Y, Mai WJ, Hughes WL, Lao CS, Wang ZL. Science 2005;309:1700-4.

[282] Gao PX, Wang ZL. Small 2005;1:945-9.

[283] Yan H, Johnson J, Law M, He R, Knutsen K, McKinney JR, Pham J, Saykally R, Yang PD. Adv Mater 2003;15:1907-11.

[284]Huang MH, Mao S, Feick H, Yan HQ, Wu YY, Kind H, Weber E, Russo R, Yang PD. Science 2001;292:1897-9.

[285] Jie J, Wang G, Wang Q, Chen Y, Han X, Wang X, Hou JG. J Phys Chem B 2004;108:11976-80.

[286] Huang MH, Wu YY, Feick H, Tran N, Weber E, Yang PD. Adv Mater 2001;13:113-6

[287] Li SY, Lee CY, Tseng TY. J Cryst Growth 2003;247:357-62.

[288] Jie J, Wang G, Wang Q, Chen Y, Han X, Wang X, Hou JG. J Phys Chem B 2004;108:11976-80.

[289] Kim DS, Ji R, Fan HJ, Bertram F, Scholz R, Dadgar A, Nielsch K, Krost A, Christen J, Gosele U, Zacharias M. Small 2007;3:76-80.

[290] Wang XD, Summers CJ, Wang ZL. Nano Lett 2004;4:423-6.

[291] Prades JD, Jininez-Diaz R, Hernandez-Ramirez F, Fernandez-Romero L, Andreu T, Cirera A, Romano-Rodriguez A, Cornet A, Morante JR, Barth S, Mathur S. J Phys Chem C 2008;112:14639-44.

[292] Wang XD, Song JH, Li P, Ryou JH, Depuis RD, Summers CJ, Wang ZL. J Am Chem Soc 2005;127:7920-3.

[293] Yan HQ, He RR, Pham J, Yang PD. Adv Mater 2003;15:402-5.

[294] Wang XD, Ding Y, Summers CJ, Wang ZL. J Phys Chem B 2004;108:8773-7.

[295] Zou BS, Liu RB, Wang FF, Pan AL, Cao L, Wang ZL. J Phys Chem B 2006;110:12865-73.

[296] Li Y, Meng GW, Zhang LD, Phillipp F. Appl Phys Lett 2000;76:2011-3.

[297] Yuhas BD, Zitoun DO, Pazauskie PJ, He RR, Yang PD. Angew Chem Int Ed 2006;45:420-3.

[298] Vayssieres L. Adv Mater 2003;15:464-6.

[299] Cui JB, Daghlian CP, Gibson UJ, Pusche R, Gleithner P, Ley L. J Appl Phys 2005;97:44315.

[300] Chen SY, Lin CC, Chen SY. J Cryst Growth 2005;283:141-6.

[301] Greene LE, Law M, Tan DH, Montano M, Goldberger J, Somorjai G, Yang PD. Nano Lett 2005;5:1231-6.

[302] Yang X, Shao C, Guan H, Li X, Gong J. Inorg Chem Commun 2004;7:176-8.

[303] Viswanathamurthi P, Bhattarai N, Kim HY, Lee DR. Nanotechnology 2004;15:320-3.

[304] Wu H, Pan W. J Am Ceram Soc 2006;89:699-701.

[305] Wang W, Huang H, Li Z, Zhang H, Wang Y, ZhengW, Wang C. J Am Ceram Soc 2008;91:3817-9.

[306] Mathur S, Barth S, Shen H, Pyun JC, Werner U. Small 2005;1:713-7.

[307] Mathur S, Barth S. Small 2007;3:2070-5.

[308] Ma YJ, Zhou F, Lu L, Zhang Z. Solid State Commun 2004; 130:313-6.

[309] Lou SH, Fan JY, Liu WL, Zhang M, Song ZT, Lin CL, Wu XL, Chu PK. Nanotechnology 2006;17:1695-9.

[310] Lilach Y, Zhang JP, Moskovits M, Kolmakov A. Nano Lett 2005;5:2019-22.

[311] Arbiol J, Comini E, Faglia G, Sbeveglieri G, Morante JR. J Cryst Growth 2008;310:253-60.

[312] Dai ZR, Gole JL, Stout JD, Wang ZL. J Phys Chem B 2002;106:1274-9.

[313] Calestani D, Zha M, Zappettini A, Lazzarini L, Salviati G, Zanotti L, Sberveglieri G. Mater Sci Engin C 2005:25:625-30.

[314] Wan Q, Wang TH. Chem Comm 2005;3841-3.

[315] Yang R, Wang ZL. J Am Chem Soc 2006;128:1466-7.

[316] Comini E, Faglia G, Sberveglieri G, Calestani D, Zanotti L, Zha M. Sens Actuators B 2005;111:2-6.

[317] Liu ZQ, Zhang DH, Han S, Li C, Tang T, Jin W, Liu XL, Lei B, Zhou CW. Adv Mater 2003;15:1754-7.

[318] Hu JQ, Bando Y, Liu QL, Golberg D. Adv Funct Mater 2003;13:493-6.

[319] Dai ZR, Pan ZW, Wang ZL. Solid State Commun 2001;118:351-4.

[320] Zhang J, Jiang F, Zhang L. Phys Lett A 2004;322:363-8.

[321] Wang B, Yang YH, Wang CX, Yang GW. J Appl Phys 2005;98:073520.

[322] Nguyen P, Ng HT, Kong J, Cassel AM, Quinn R, Li J, Han J, McNeil M, Meyyappan M. Nano Lett 2003;3:925-8.

[323] Budak S, Miao GX, Ozdemir M, Chetry KB, Gupta A. J Cryst Growth 2006;291:405-11.

[324] Wang JX, Liu DF, Yan XQ, Yuan HJ, Ci LJ, Zhou ZP, Gao Y, Song L, Liu LF, Zhou WY, Wang G, Xie SS. Solid State Commun 2004;130:89-94.

[325] Hu JQ, Ma XL, Shang NG, Xie ZY, Wong NB, Lee CS, Lee ST. J Phys Chem B 2002;106:3832.

[326] Zheng MJ, Li GH, Zhang XY, Huang SY, Lei Y, Zhang LD. Chem Mater 2001;13:3859-61.

[327] Kolmakov A, Zhang Y, Cheng G, Moskovits M. Adv Mater 2003;15:997-1000.

[328] Wang Y, Aponte M, Leon N, Ramos I, Furlan R, Pinto N, Evoy S, Santiago-Aviles JJ. J Am Ceram Soc 2005;88:2059-63.

[329] Wang Y, Aponte M, Leon N, Ramos I, Furlan R, Evoy S, Santiago-Aviles J J. Semicond Sci Technol 2004;19:1057-60.

[330] Zhang Y, He X, Li J, Miao Z, Huang F. Sens Actuators B 2008;132:67-73.

[331] Wang CX, Hirano M, Hosono H. Nano Lett 2006;6:1552-5.

[332] Cayron C, Den Hertog M, Latu-Romain L, Mouchet C, Secouard C, Rouviere JL, Rouviere E, Simonato JP. J Appl Cryst 2009;42:242-52.

[333] Mieszawska AJJalilian R, Sumanasekera GU, Zamborini FP. Small 2007;3:722-56.

[334] Zakharov ND, Werner P, Gerth G, Schubert L, Sokolov L, Gosele U. J Cryst Growth 2006;290:6-10.

[335] Wu YY, Fan R, Yang PD. 2002. Nano Lett 2002;2:83-6.

[336] Geyer N, Hunag Z, Fuhrmann B, Grimm S, Reiche M, Nguyen-Duc TK, de Boor J, Leipner HS, Werner P, Gosele U. Nano Lett 2009;9:3106-10.

[337] Bjork MT, Ohlsson BJ, Sass T, Persson AI, Thelander C, Magnusson MH, Deppert K, Wallenberg LR, Samuelson L. Nano Lett 2002;2:87-9.

[338] Gudiksen MS, Lauhon LJ, Wang J, Smith DC, Lieber CM. Nature 2002;415:617-20.

[339] Ouyang L, Maher KN, Yu CL, McCarty J, Park H. J Am Chem Soc 2007;129:133-8.

[340] Wu Y, Xiang J, Yang C, Lu W, Lieber CM. Nature 2004;430:61-5.

[341] Maynor BW, Li JY, Lu CG, Liu J. J Am Chem Soc 2004;126:6409-13.

[342] Lauhon LJ, Gudiksen MS, Wang CL, Lieber CM. Nature 2002;420:57-61.

[343] Lu W, Xiang J, Timko BP, Wu Y, Lieber CM. PNAS 2005;102:10046-51.

[344] Qian F, Gradecak S, Li Y, Lieber CM. Nano Lett 2005;5:2287-91.

[345] Qian F, Li Y, Gradecak S, Park HG, Dong Y, Ding Y, Wang ZL, Lieber CM. Natur Mater 2008;7:701-6.

[346] Morral AFI, Spiroska D, Arbiol J, Heigold M, Morante JR, Abstreiter G. Small 2008;4:899-903.

[347] Pan AL, Yao L, Qin Y, Yang Y, Kim DS, Yu R, Zou B, Werner P, Zacharias M, Gosele U. Nano Lett 2008;8:3413-7.

[348] Goldberger J, Hochbaum AI, Fan R, Yang PD. Nano Lett 2006;6:973-7.

[349] Dick KA, Deppert K, Larsson MW, Martensson T, Seifert W, Wallenberg LR, Samuelson L. Nature Mater 2004;3:380-4.

[350] Bae SY, Seo HW, Choi HC, Park J. J Phys Chem B 2004;108:12318-26.

[351] Xu L, Su Y, Li S, Chen YQ, Zhou QT, Yin S, Feng Y. J Phys Chem B 2007;111:760-6.

[352] Shimizu T, Zhang Z, Shingubara S, Senz S, Gosele U. Nano Lett 2009;9:1523-6.

[353] Ng HT, Han J, Yamada T, Nguyen P, Chen YP, Meyyappan M. Nano Lett 2004;4:1247-52.

[354] Hochbaum AI, Fan RR, He R, Yang PD. Nano Lett 2005;5:457-60.

[355] Huang JX, Tao AR, Connor S, He R, Yang PD. Nano Lett 2006;6:524-9.

[356] Martensson T, Carlberg P, Bergstrom M, Montelius L, Seifert W, Samuelson L. Nano Lett 2004;4:699-702.

[357] He RR, Gao D, Fan R, Hochbaum AI, Carraro C, Maboudian R, Yang PD. Adv Mater 2005;17:2098-2102.

[358] Islam MS, TI Kamins, RS Williams. Nanotechology 2004;15:L5-8.

[359] Yi SS, Girolami G, Amano J, Islam MS, Sharma S, Kamins TI, Kimukin I. Appl Phys Lett 2006;89:133121.

[360] Yu GH, Cao AY, Lieber CM. Nature Nanotechn 2007;2:372-7.

[361] Yang PD, Kim F. Chem Phys Chem 2002;3:503-6.

[362] Whang D, Jin S, Wu Y, Lieber CM. Nano Lett 2003;3:1255-9.

[363] Jin S, Whang DM, McAlpine MC, Friedman RS, Wu Y, Lieber CM. Nano Lett 2004;4:915-9.

[364] Wang D, Zhu R, Zhou Z, Ye X. Appl Phys Lett 2007;90:103110.

[365] Lao CS, Liu J, Gao PX, Zhang LY, Davidovic D, Tummala R, Wang ZL. Nano Lett. 2006;6:263-6.

[366] Suh DI, Lee SY, Hyung JH, Kim TR, Lee SK. J Phys Chem C 2008;112:1276-81.

[367] Raychaudhuri S, Dayeh SA, Wang D, Yu ET. Nano Lett 2009;9:2260-6.

[368] Javey A, Friedman RS, Yan H, Lieber CM. Nano Lett 2007;7:773-7.

[369] Fan ZY, Ho JC, Jacobson ZA, Yerushalmi R, Alley RL, Razavi H, Javey A. Nano Lett 2008;8:20-5.

[370] Xu CN, Tamaki J, Miura N, Yamazoe N. Sens Actuators B 1991;3:147-155.

[371] Yamazoe N. Sens Actuators B 1991;3:7-19.

[372] Zheng GF, Lu W, Lieber CM. Adv Mater 2004;16:1890-3.

[373] Lu W, Xie P, Lieber CM. IEEE Transactions on Electron Devices 2008;55:2859-76.

[374] Li Z, Chen Y, Li X, Kamins TI, Nauka K, Williams RS. Nano Lett 2004;4:245-7.

[375] Wang WU, Chen C, Lin KH, Fang Y, Lieber CM. PNAS 2005;102:3208-12.

[376] Cui Y, Wei QQ, Park HK, Lieber CM. Science 2001;293:1289-92.

[377] Hahm J, Lieber CM. Nano Lett 2004;4:51-4.

[378] Zheng GF, Patolsky F, Cui Y, Wang WU, Lieber CM. Nature Biotechn 2005;23:1294-301.

[379] Patolsky F, Zheng G, Hayden O, Lakadamyali M, Zhuang XW, Lieber CM. PNAS 2004:14017-22.

[380] Stern E, Klemic JF, Routenberg DA, Wyrembak PN, Turner-Evans DB, Hamilton AD, LaVan DA, Fahmy TM, Reed MA. Nature 2007;445:519-22.

[381] Bunimovich YL, Shin YS, Yeo W-S, Amori M, Kwong G, Heath JR. J Am Chem Soc 2006;128:16323-31.

[382] Gao ZQ, Agarwal A, Trigg AD, Singh N, Fang C, Tung C-H, Fan Y, Buddharaju KD, Kong J. Anal Chem 2007;79:3291-7.

[383] Zhang GJ, Zhang G, Chua JH, Chee RE, Wong EH, Agarwal A, Buddharaju KD, Singh N, Gao Z, Balasubramanian N. Nano Lett 2008;8:1066-70.

[384] Kim DR, Lee CH, Zheng X. Nano Lett 2009;9:1984-8.

[385] Barsan N, Weimar U. J Electroceram 2001;7:143-67.

[386] Hernandez-Ramirez F, Prades JD, Tarancon A, Barth S, Casals O, Jimenez-Diaz R, Pellicer E, Rodriguez J, Morante JR, Juli MA, S.Mathur, Romano-Rodriguez A. Adv Funct Mater 2008;18:2990-4.

[387] Batzill M, Diebold U. Prog Surf Sci 2005;79:47-154.

[388] Prades JD, Cirera A, Morante JR. J Electrochem Soc 2007;154:H675-80.

[389] Prades JD, Cirera A, Morante JR, Pruneda JM, Ordejon P. Sens. Actuators B 2007;126:62-7.

[390] Heiland G, Kohl D. Physical and chemical aspects of oxidic semiconductor gas sensors. In: Seiyama T, editor. Chemical sensor technology, vol. 1. Tokyo: Kodansha:, 1988, p 15-38.

[391] Hernandez-Ramirez F, Barth S, Tarancon A, Casals O, Pellicier E, Rodriguez J, Romano-Rodriguez A, Morante JR, Mathur S. Nanotechnology 2007;18:424016.

[392] Comini E, Faglia G, Sberveglieri G, Pan Z, Wang ZL. Appl Phys Lett 2002;81:1869-71

[393] Hernandez-Ramirez F, Tarancon A, Casals O, Arbiol J, Romano-Rodriguez A, Morante JR. Sens Actuators B 2007;121:3-17.

[394] Kolmakov A, Zhang YX, Cheng GS, Moskovits M. Adv. Mater. 2003;15:997-1000.

[395] Hernandez-Ramirez F, Tarancon A, Casals O, Pellicier E, Rodriguez J, Romano-Rodriguez A, Morante JR, Barth S, Mathur S. Phys Rev B 2007, 76, 085429.

[396] Agarwal R. Small 2008;4:1872-93.

[397] Hernandez-Ramirez F, Prades JD, Tarancon A, Barth S, Casals O, Jimenez-Diaz R, Pellicer E, Rodriguez J, Juli MA, Romano-Rodríguez A, Morante JR, Mathur S, Helwig A, Spannhake J, Mueller G. Nanotechnology 2007;18:495501.

[398] Prades JD, Jiminez-Diaz R, Hernandez-Ramirez F, Barth S, Cicera A, Mathur S, Romano-Rodriguez A, Morante JR. Appl Phys Lett 2008;93:123110.

[399] Strelcov E, Dmitriev S, Button B, Cothren J, Sysoev V, Kolmakov A. Nanotechnology 2008;19:355502.

[400] Kolmakov A, Klenov DO, Y Lilach, S. Stemmer, Moskovits M. Nano Lett 2005;5:667-73.

[401] Sysoev VV, Goschnick J, Schneider T, Strelchov E, Kolmakov A. Nano Lett 2007;7:3182-8.

[402] Sysoev VV, Schneider T, Goschnick J, Kiselev I, Habicht W, Hahn H, Strelchov E, Kolmakov A. Sens Actuators B 2009;139:699-703.

[403] Wan Q, Li QH, Chen YJ, Wang TH, He XL, Li JP, Lin CL. Appl Phys Lett 2004;84:3654-6.

[404] Xu JQ, Chen YP, Li YD, Shen JN. J Mater Sci 2005;40:2919-21.

[405] Law M, Kind H, Messer B, Kim F, Yang PD. Angew Chem Int Ed 2002;41:2405-8.

[406] Prades JD, Jiminez-Diaz R, Hernandez-Ramirez F, Barth S, Cirera A, Romano-Rodriguez A, Mathur S, Morante JR. Sens Actuators B 2009; 140:337-41.

[407] Boukai AI, Bunimovich Y, Tahir-Kheli J, Yu JK, Goddard III WA, Heath JR. Nature 2008;451:168-71.

[408] Hochbaum AI, Chen RK, Delgado RD, Liang WJ, Garnett EC, Najarian M, Majumdar A, Yang PD. Nature 2008;451:163-5.

[409] Gratzel M. Nature 2001;414:338-44.

[410] Tsakalakos L, Balch J, Fronheiser J, Shih MY, LeBoeuf SF, Pietrzykowski M, Codella PJ, Korevaar BA, Sulima O, Rand J, Davuluru A, Rapol U. J Nanophoton 2007;1:013552.

[411] Hu L, Chen G. Nano Lett 2007;7:3249-54.

[412] Sivakov V, Andra G, Gawlik A, Berger A, Plentz J, Falk F, Christiansen SH. Nano Lett 2009;9:1549-54.

[413] Tian BZ, Zheng XL, Kempa TJ, Fang Y, Yu NF, Yu GH, Huang JL, Lieber CM. Nature 2007;449:885-8.

[414] Tsakalakos L, Balch J, Fronheiser J, Korevaar BA, Sulima O, Rand J. Appl Phys Lett 2007;91:233117.

[415] Kempa TJ, Tian BZ, Kim DR, Hu JS, Zheng XL, Lieber CM. Nano Lett 2008;8:3456-60.

[416] Kayes BM, Atwater HA, Lewis NS. J Appl Phys 2005;97:1143020.

[417] Tang YB, Chen ZH, Song HS,. Lee CS, Cong HT, Cheng HM, Zhang WJ, Bello I, Lee ST. Nano Lett 2008;8:4191-5.

[418] Goodey AP, Eichfeld SM, Lew KK, Redwing JM, Mallouk TE. J Am Chem Soc 2007;129:12344-5.

[419] Bard AJ, Bocarsly AB, Fan FRF, Walton EG, Wrighton MS. J Am Chem Soc 1980;102:3671-7.

[420] Maiolo JR, Kayes BM, Filler MA, Putnam MC, Kelzenberg MD, Atwater HA, Lewis NS. J Amer Chem Soc 2007;129:12346-7.

[421] Peng K, Wang X, Lee ST. Appl Phys Lett 2008;92:163103.

[422] Yuan G, Zhao H, Liu X, Hasanali ZS, Zou Y, Levine A, Wang D. Angew Chem Int Ed 2009; DOI: 10.1002/anie.200902861.

[423] Law M, Greene LE, Johnson JC, Saykally R, Yang PD. Nature Mater 2005;4:455-9.

[424] Baxter JB, Walker AM, van Ommering K, Aydil AS. Nanotechnology 2006;17:S304-12.

[425] Jiang CY, Sun XW,. Lo GQ, Kwon DL, Wang JX. Appl Phys Lett 2007;90:263501.

[426] Ku CH, Wu JJ. Appl Phys Lett 2007;91:093117.

[427] Jiang CY, Sun XW, Tan KW, Lo GQ, Kyaw AKK, Kwong DL. Appl Phys Lett 2008;92:143101.

[428] Law M, Greene LE, Radenovic A, Kuykendall T, Liphardt J, Yang PD. J Phys Chem B 2006;110:22652-63.

[429] Weintraub B, Wei Y, Wang ZL. Angew Chem Int Ed 2009;48:8981-5.

[430] Leschkies KS, Divakar R, Basu J, Enache-Pommer E, Boercker JE, Carter CB, Kortshagen UR, Norris DJ, Aydil ES. Nano Lett 2007;7:1793-8.

[431] Yuhas BD, Yang PD. J Am Chem Soc 2009;131:3756-61.

[432] Wang ZL, Song JH. Science 2006;312:242-6.

[433] Song JH, Zhou J, Wang ZL. Nano Lett 2006;6:1656-62.

[434] Gao Y, Wang ZL. Nano Lett 2007;7:2499-505.

[435] Alexe M, Senz S, Schubert MA, Hesse D, Gosele U. Adv Mater 2008;20:4021-6.

[436] Wang ZL. Adv Mater 2009;21:1311-5.

[437] Wang XD, Song JH, Liu J, Wang ZL. Science 2007;316:102-5.

[438] Wang XD, Liu J, Song JH, Wang ZL. Nano Lett 2007;7:2475-9.

[439] Xu S, Wei YG, Liu J, Yang R, Wang ZL. Nano Lett 2008;8:4027-32.

[440] Qin Y, Wang XD, Wang ZL. Nature 2008;451:809-14.

[441] Qin Y, Wang X, Wang ZL. Nature 2009;457:340.

[442] Yang RS, Qin Y, Dai LM, Wang ZL. Nature Nanotechn 2009;4:34-9.

[443] Yang R, Qin Y, Li C, Zhu g, Wang ZL. Nano Lett 2009;9:1201-5.

[444] Kwon SS, Hong WK, Jo G, Maeng J, Kim TW, Song S, Lee T. Adv Mater 2008;20:4557-62.

[445] Yu MY, Song J, Lu MP, Lee CY, Chen LJ, Wang ZL. ACS Nano 2009;3:357-62.

[446] Lin YF, Song J, Ding Y, Lu SY, Wang ZL. Appl Phys Lett 2008;92:022105.

[447] Ying Z, Wang Q, Cao H, Song ZT, Feng SL. Appl Phys Lett 2005;87:113108.

[448] Park MS, Wang GX, Kang YM, Wexler D, Dou SX, Liu HK. Angew Chem Int Ed 2007;46:750-3.

[449] Park MS, Kang YM, Wang GX, Dou SX, Liu HK. Adv Funct Mater 2008;18:455-61.

[450] Meduri P, Pendyala C, Kumar V, Sumanasekera GU, Sunkara MK. Nano Lett 2009;9:612-6.

[451] Kim DW, Hwang IS, Kwon SJ, Kang HY, Park KS, Choi YJ, Choi KJ, Park JG. Nano Lett 2007;7:3041-5.

[452] Wang Y, Zeng HC, Lee JY. Adv Mater 2006;18:645-9.

[453] An G, Na N, Zhang X, Miao Z, Miao S, Ding K, Liu Z. Nanotechnology 2007;18:435707.

[454] Chen YJ, Zhu CL, Xue XY, Shi XL, Cao MS. Appl Phys Lett 2008;92:223101.

[455] Chan CK, Peng HL, Liu G, McIlwrath K, Zhang XF, Huggins RA, Cui Y. Nature Nanotechn 2008;3:31-5.

[456] Chan CK, Ruffo R, Hong SS, Cui Y. J Power Sources 2009;189:1132-40.

[457] Graetz J, Ahn CC, Yazami R, Fultz B. Electrochem Solid State Lett 2003;6:A194-7.

[458] Chan CK, Ruffo R, Hong SS, Huggins RA, Cui Y. J Power Sources 2009;189:35-9.

[459] Li H, Huang X, Chen L, Zhou G, Zhang Z, Yu D, Mo YJ, Pei N. Solid State Ionics 2000;135:181-91.

[460] Cui LF, Ruffo R, Chan CK, Peng H, Cui Y. Nano Lett 2009;9:491-5.

[461] Peng K, Jie J, Zhang W, Lee ST, Appl Phys Lett 2008;93:033105.

[462] Cui LF, Yang Y, Hsu CM, Cui Y. Nano Lett 2009;9:3370-4.

[463] Park MH, Kim MG, Joo J, Kim K, Kim J, Ahn S, Cui Y, Cho J. Nano Lett 2009;9:3844-7.

[464] Chan CK, Zhang XF, Y. Cui Y. Nano Lett 2008;8:307-9.

[465] Endo M, Kim C, Nishimura K, Fujino T, Mijashita K. Carbon 2000;38:183-97.

[466] Duan X, Huang Y, Cui Y, Wang J, Lieber CM. Nature 2001;409:66-9.

[467] Haraguchi K, Katsuyama T, Hiruma K, Ogawa K. Appl Phys Lett 1992;60:745-7.

[468] Quian F, Li Y, Gradecak S, Wang D, Barrelet CJ, Lieber CM. Nano Lett 2004;4:1975-9.

[469] Qian F, Gradecak S, Li Y, Wen CY, Lieber CM. Nano Lett 2005;5:2287-91.

[470] Svensson CPT, Martensson T, Tragardh J, Larsson C, Rask M, Hessmann D, Samuelsson L, Ohlsson J. Nanotechnology 2008;19:305201.

[471] Huang Y, Duan XF, Lieber CM. Small 2005;1:142-7.

[472] McAlpine MC, Friedman RS, Jin S, Lin K, Wang WU, Lieber CM. Nano Lett 2003;3:1531-5.

[473] Gudiksen MS, Lauhon LJ, Wang J, Smith DC, Lieber CM. Nature 2002;415:617-20.

[474] Kim HM, Kang TW, Chung KS. Adv Mater 2003;15:567-60.

[475] Sun XW, Huang JZ, Wang JX, Xu Z. Nano Lett 2008;8:1219-23.

[476] Nandarajah A, Word RC, Meiss J, Konenkamp R. Nano Lett 2008;8:534-7.

[477] Konenkamp R, Word RC, Schlegel C. Appl Phys Lett 2004;85:6004-6.

[478] Kim HM, Cho YH, Lee H, Kim SI, Ryu SR, Kim DY, Kan TW, Chung KW. Nano Lett 2004;4:1059-62.

[479] Huang HW, Kao CC, Hsueh TH, Yu CC, Lin CF, Chu JT, Kuo HC, Wang SC. Mater Sci Eng B 2004;113:125-9.

[480] Hsieh YP, Chen HY, Lin MZ, Shiu SC, Hofmann M, Chern MY, Jia X, Yang YJ, Chang HJ, Huang HM, Tseng SC, Chen LC, Chen KH, Lin CF, Liang CT, Chen YF. Nano Lett 2009;9:1839-45.

[481] Zimmler MA, Stichtenoth D, Ronning C, Yi W, Narayanamurti V, Voss T, Capasso F. Nano Lett 2008;8:1695-99.

[482] Bao J, Zimmler MA, Capasso F, Wang X, Ren ZF. Nano Lett 2006;6:1719-22

[483] Zimmler MA, Bao, J, Shalish I, Yi W, Yoon J, Narayanamurti V, Capasso F. Nanotechnology 2007;18:235205.

[484] Zimmler MA, Bao, J, Shalish I, Yi W, Yoon J, Narayanamurti V, Capasso F. Nanotechnology 2007;18:395201.

[485] Duan X, Huang Y, Agarwal R, Lieber CM. Nature 2003;421:241-5.

[486] Greytak AB, Barrelet CJ, Li Y, Lieber CM. Appl Phys Lett 2005;87:151103.

[487] Johnson JC, Choi, HJ, Knutsen KP, Schaller RD, Yang PD, Saykelly RJ. Nature Mater 2002;1:106-10.

[488] Liu YK, Zapien JA, Shan YY, Geng CY, Lee CS, Lee ST. Adv Mater 2005;17:1372-7.

[489] Liu YK, Zapien JA, Shan YY, Tang H, Lee CS, Lee ST. Nanotechnology 2007;18:365606.

[490] Maslov AV, Ning CZ. Appl Phys Lett 2003;83:1237-8.

[491] Zimmler MA, Bao J, Capasso F, Muller S, Ronning C. Appl Phys Lett 2008;93:051101.

[492] Gradecak S, Qian F, Li Y, Park HG, Lieber CM. Appl Phys Lett 2005;87:173111.

[493] Oulton RF, Sorger VJ, Zentgraf T, Ma RM, Gladden C, Dai L, Bartal G, Zhang X. Nature 2009;461:629-32.

[494] Pan A, Liu D, Liu R,Wang F, Zhu X, Zou B. Small 2005;1:980-3.

[495] Law M, Sirbuly DJ, Johnson JC, Goldberger J, Saykally RJ, Yang PD. Science 2004;305:1269-73.

[496] Siburly DJ, Law M, Pauzauskie P, Yan H, Maslov AV, Knutsen K, Ning CZ, Saykally RJ, Yang PD. PNAS 2005;102:7800-2.

[497] Pauzauskie PJ, Radenovic A, Trepagnier E, Shroff H, Yang PD, Liphardt J. Nature Mater 2006;5:97-101.

[498] van der Meulen MI, Petkov N, Morris MA, Kazakova O, Han XH, Wang KL, Jacob AP, Holmes JD. Nano Lett 2009;9:50-6.

[499] Tian B, Xie P, Kempa TJ, Bell DC, Lieber CM. Nature Nanotechn 2009; DOI: 10.1038/NNANO.2009.304